공학박사 학위논문

Development of Electrode Materials and Architectures for Safe and Efficient Energy Storage in Li-Ion Batteries and Supercapacitors

효율적이고 안전한 에너지 저장을 위한 리튬이온전지 및 슈퍼커패시터 용 전극물질의 개발과 아키텍쳐링

2016년 2월

서울대학교 대학원

화학생물공학부

박 수 민

Abstract

Development of Electrode Materials and Architectures for Safe and Efficient Energy Storage in Li-Ion Batteries and Supercapacitors

Soomin Park

School of Chemical and Biological Engineering

The Graduate School

Seoul National University

Occasional reports on accidental explosions that appear in the news, increases the safety concerns of using Li ion batteries (LIBs). The scope of LIB is expanding toward large-scale energy storage systems such as electrified transportation and smart grids. Considering these facts, manufacturers and consumers now have concerns regarding the safe use of such devices. The high voltage anode materials have greatly relieved the unstable state of LIB during operation because they can exclude the uneven plating of lithium and reductive electrolyte decomposition. Although various titanium based oxides have been developed as high voltage anode, low capacity or poor potential flatness still severely hinder their industrial usage. In this dissertation, two types of titanium-based crystals are proposed, and they exhibited enhanced Li storage performance as high voltage anode materials as follows.

- A c-channel that is formed inside stacked (001) planes in rutile TiO_2 exhibits the lowest energy barrier for Li migration. In this regard, the rational design of a TiO_2 architecture for stacked (001) planes is needed in

order to maximize Li storage. Here, a three-dimensional and dendritic TiO_2 sphere comprised of c-channel specialized nanorods is proposed, which can be prepared via the specific adsorption of chlorine ion on the (110) plane. Along with a confined Li pathway, such radially assembled TiO_2 nanorods show a low intercrystalline resistance. When fabricated into an electrode, the three-dimensional and dendritic TiO_2 sphere is capable of delivering an almost 100% Coulombic efficiency in conjunction with long cycle charge/discharge stability (300 cycles). This approach, which is based on theoretical studies and experimental validation, provides guidance for tailoring electrode materials for use in Li storage systems.

- $H_2Ti_{12}O_{25}$ (HTO), a recently discovered anode material for LIB, has outstanding electrochemical performance compared to other high voltage materials. However, its thermodynamic/kinetic properties as a Li host have not been thoroughly investigated yet. In this study, the Li storing behavior of HTO was intensively characterized by a combined theoretical experimental study. In addition, the strong dependence of electrochemical performance on Li diffusion kinetics stimulated us to develop a nanostructured HTO which provides incorporated Li with a short diffusion length inside a nano-crystal. As a result, the nanostructured HTO showed upgraded Li storage performance. This work suggests that the HTO is one of the most competitive material found to date for the construction of advanced LIB with excellent safety and stability.

Electrochemical capacitors (so-called supercapacitors), with high power density and superior cycling ability, are considered to be one of the most stable and safe energy storage systems. High power as well as reasonably high energy density are provided, supercapacitors are likely to be regarded as a representative energy storage system along with batteries. The common

challenge in supercapacitor design is the resistive behavior originated from sluggish ion transport, poor electrical conductivity, and high charge transfer resistance, which increases equivalent series resistance of overall cell. In addition, a variety of activation process for the increase of surface area not only are involved in harmful chemicals or toxic metals but also lower its cost-effectiveness. In this dissertation, two strategies for resolving above-mentioned challenging points are proposed; 3D bicontinuous metal-carbon hybrid and organic gel-wrapped MnO_2 thin fim electrode.

- The three dimensionally aligned bicontinuous carbon and metal hybrids are synthesized. The resulting material shows a significantly high rate capability up to 1,000 V s^{-1}. The proposed strategy exploits an agarose gel as a template for the simultaneous construction of three dimensional (3D) carbon structures filled with a metal-lined architecture in supercapacitors. The carbon framework with three dimensional and interconnected metal lines inside minimizes both empty inner pores and electron transfer barriers, which results in a substantial reduction of the overall electrode resistance. In addition, it can be used for the filteration of voltage ripples due to the ultrafas7t response with high efficiency.
- A robust hybrid film containing MnO_2 was prepared for achieving large areal capacitances. An agarose gel, as an ion-permeable and elastic layer coated on a current collector, plays a key role in stabilizing the deposited pseudocapacitive MnO_2. Cyclic voltammetry and electrochemical impedance spectroscopy data indicate that the hybrid electrode is capable of exhibiting a high areal capacitance up to 52.55 mF cm^{-2}, with its superior structural integrity and adhesiveness to the current collector being maintained, even at a high MnO_2 loading.

The emergence of body-centric power generators such as piezoelectric/solar

cell and the functional/morphological evolution of smart phones have created a need for advanced devices for energy storage. In order to meet the power demand of such devices, the construction of a series of unconventional energy storage systems have been developed in the past few years, which enable one to achieve flexible, foldable, and stretchable characteristics. In order to secure their stability and safety of energy storage platform under mechanically stressed conditions, the primary requirements of electrode materials include robust electrical connectivity and mechanical endurance. In the last part of this dissertation, a 'lint taping' method is described for the fabrication of thin layer of conducting network using graphite felt.

- An all-solid-state, completely foldable and washable energy storage platform was fabricated. By adopting it as a supercapacitor electrode, the physical characteristics and electrochemical properties of such a GFCN are identified. A constructed graphitic fiber network derived from conventional graphite felt was readily assembled into a full-cell by its self-adhering architecture. The as-prepared system exhibits high mechanical properties under various folding motifs and washable characteristics without capacitance fading by virtue of the robust electrical connectivity of the fibrous graphite network and intimate contact between the polymeric gel electrolyte and the electrodes. The collected results suggest that this supercapacitor system is a promising candidate for practically available and wearable energy storage systems with high cost-effectiveness and scalability.

Keywords: energy storage system, safety, stability, Li-ion battery, supercapacitor, high voltage anode materials, TiO_2, $H_2Ti_{12}O_{25}$, hybrid electrode, metal-carbon bicontinuous structure, MnO_2, all-solid-state, wearable, washable

Student Number: 2010-22811

Contents

List of Tables

List of Figures

Chapter 1. Introduction

1.1 Toward safe and efficient Li-ion batteries: Development of high voltage anode materials

1.1.1 Development of Li-related batteries from a safety standpoint

The essential reason that a battery technology is based on metallic Li as anode is directly related to the fact that Li is the most electropositive (-3.04 V *vs.* standard hydrogen electrode) and the lightest (6.94 g mol^{-1} and 0.53 g cm^{-3}) metal. The physical and chemical properties of Li metal enables one to develop energy storage systems with high energy density [1]. However, there is a crucial drawback of a Li-metal/electrolyte configuration, which is uneven (dendritic) Li growth during the repeated charge/discharge cycles. This phenomenon brings about an explosion caused by short-circuit and overheat of battery. (Figure 1-1(a)) [2, 3].

In order to exclude the safety issues which is associated with the problematic Li growth, a second insertion materials (Figure 1-1(b)) was developed [4, 5]. This technology is referred to as "Li-ion" or "rocking-chair" battery system. The Li-ion batteries (LIBs) significantly relieve the dendritic problem and are intrisically safer than Li-metal cells because Li is in ionic state rather than metallic state. To compensate for the elevated potential of Li insertion to the negative electrode, the compounds with higher Li insertion potential have been

developed for use in positive electrode. It is a reason that the rigourous researches have been conducted to develop layered or three-dimensional-type transition metal oxides (e.g. $LiCoO_2$, $LiNiO_2$, and $LiMn_2O_4$) as positive electrodes [6].

Up to now, the LIBs have secured success and been upgraded through a selective adoptation of appropriated materials or a discovery of new active materials [7-15]. However, occasional reports on accidental explosions that appear in the news, increases thte safety concerns of using Li-ion cells. The scope of LIBs is expanding toward large-scale energy storage systems such as electrified transportation and smart grids [16-18]. Considering these facts, manufacturers and consumers now have concerns regarding the use of such devices. In fact, the poor safety or failure process of LIBs are rooted mainly in side reactions occurring at the negative electrode (solid)-electrolyte interface (SEI), and addressing this interfacial issues is highly complicated. It should be noted that, despite substantial research efforts have been placed on the failure mechanism which might be originated from undesirable solid electrolyte interfaces (SEIs) located on anode materials, its composition and nature are still the subject of controversy [19-24].

1.1.2 Challenges in development of high voltage anode materials for use in LIBs

The currently available LIBs based on graphite anode materials can hardly satisfy the requirements for high capacity large-scale applications due to the

limitations associated with power density, stability, and safe characteristics. In order to effectively assure stability and safety of LIBs, the high voltage anode materials which can be operated over 0.8 V (*vs.* Li/Li^+) have attracted great attention recently because they can exclude the uneven plating of Li, reductive electrolyte decomposition due to almost free of SEI film (Figure 1-2).

Titanates, including $L_4Ti_5O_{12}$ (LTO) and TiO_2, are being intensively investigated for use as high voltage anodes [25, 26]. Although various titanium based oxides have been developed as high voltage anodes, low capacity or poor potential flatness still severely hiner their industrial usage. Spinel-structured LTO is now used in commercial LIBs, since it offers an extraordinarily flat potential plateau, long cyclic stability, and high rate capability. However, there is a critical drawback regarding the low level of theoretical capacity (175 mAh g^{-1}) [26]. Another example, TiO_2 polymorphs (e.g. rutile, anatase, TiO_2(B)) can accommodate more Li, especially when the particle size is reduced to nanometer scale [27, 28]. However, the sloping voltage profile of nano-TiO_2 implies that the insertion of Li involves a surface redox or pseudocapacitive charging mechanism rather than a structural transformation (Figure 1-3) [29]. This Li insertion behavior causes hardships in battery management, results in considerable limitations in practically available discharge capacity (Figure 1-4) [30].

The one of important disadvantage of high voltage anode materials is that the elevated Li insertion potential lowers the operating voltage of a single cell. Recent developments in biopolar architecture in LIB systems have resolved the reduced operating voltage issue to a considerable extent by designing

electrochemical systems in sandwich structures, which results in multiplied voltage by series connections in each stack [31, 32]. High voltage anode materials are also essential for the construction of bipolar battery systems because the anode and cathode need to be loaded on the same Al current collector in opposite sides (Figure 1-5). In a bipolar LIB system, the potential window of the anode should retreat from the potential for Li-Al alloy formation (0.4 V *vs*. Li/Li^+) [33, 34].

In summary, the low capacity (LTO) or poor potential flatness (TiO_2) are current limitations of high voltage anode materials. Consequently, to make up for the weak points, considerable efforts have been devoted to constructing desired atomic/nano crystal morphology motivated by the intrinsic behavior of inorganic crystals, which has the potential to become a powerful methodology for the development of advanced high voltage anode materials.

1.1.3 Strategy 1: *c*-channel specialized TiO_2 spheres as high voltage anode materials

Considerable efforts have been devoted to constructing desired crystal morphology motivated by the theoretical basis regarding the principal behaviors of inorganic crystals [35, 36]. Titanium dioxide (TiO_2), as an important semiconductor, has attracted intense research interests owing to its potential application in electrochemical energy storage material based on Li chemistry. Importantly, the polymorphs of TiO_2 (e.g. rutile, anatase, and brookite) provide the open access to rational design of optimal nanocrystal for

Li host material.

In order to achieve the theoretical basis, it is necessary to understand the dynamics of Li in the various TiO_2 polymorphs. Briefly, when a Li atom is incorporated at interstitial sites of TiO_2, the Li modifies the distribution of charge traps within the TiO_2 [37]. The electronic charges are be distributed over the Ti atoms adjacent to Li interstitials, which suggests the strong binding (binding energy $\fallingdotseq$ 0.54 eV) between inserted Li and electrons trapped at Ti centers [38]. Localized electrons in TiO_2 that are trapped as small polarons undergo thermally activated hopping between available sites and the collective (ambipolar) migration of Li and electrons dominates the overall current of charge carriers in this regime [39]. In this light, the atomic environment (relative position of the Li^+ and the Ti^{3+}) along the migration path has a significant effect on the energy barrier and site-to-site Li mobility [40-42].

Throughout the whole Li pathways in TiO_2 polymorphs, the channel along the c-axis (referred to as the "c-channel") that is present in the interior of the rutile TiO_2 phase is known to provide a 'highway' for Li transport due to the lowest energy barrier ($\fallingdotseq$ 0.04 eV) [43]. The c-channel of rutile TiO_2 is found inside stacked (001) planes and contains large open spaces for long-range Li migration.

Here, a new three-dimensional and dendritic TiO_2 spherical structure (3D-TS) with a sub-micrometer size is prepared as an idealized architecture. A novel synthetic method based on a bicontinuous emulsion system is proposed, and the synthesis of highly uniform 3D-TS is feasible. Spherical 3D-TS was constructed by the radial assembly of c-channel specialized TiO_2 rods which

have a high aspect ratio of ~24. Computational studies reveal the growth mechanism of TiO_2 rods that comprise the 3D-TS and the directional diffusivity of Li. Thus, the 3D-TS, the formation of which takes advantage of the combination of the anisotropic morphology of the TiO_2 rods and the mobility of Li, shows optimal Li storage performance in Li-battery operations. Several studies on nanostructured rutile TiO_2 have been reported, which were mainly directed at the surface storage of Li by increasing the surface area of TiO_2 [44-48]. In this study, it should be noted that, along with the surface storage, another important factor in enhancing Li storage performance is the insertion of Li into bulk region of rutile TiO_2 via the radial alignment of facile Li pathways (Figure 1-6).

1.1.4 Strategy 2: $H_2Ti_{12}O_{25}$ nanostructures as high voltage anode materials

$H_2Ti_{12}O_{25}$ (referred to as the "HTO") first exploited as Li storage material by J. Akimoto *et al.*, should be considered to be primarily as the promising anode material covering a high operating potential range due to its outstanding energy density and flat voltage plateau: *(1)* It has a reversible capacity of over 200 mAh g^{-1}, *(2)* The Li insertion and extraction occurs at approximately 1.55 V (*vs.* Li/Li^+) [49]. Although typical charge/discharge voltage profiles and cyclic stability of HTO have been reported, the rate capability and underlying Li storage mechanism of HTO are mostly unknown [50].

In this work, a detailed examination of the electrochemical properties of HTO

is investigated from a kinetic perspective and, based on the collected results, the nanostructure of HTO is proposed. Specifically, *(1)* the characteristics of Li diffusion inside the HTO crystal were identified by *ab initio* calculations using density functional theory (DFT). And, *(2)* a strong dependence of Li storage performance on Li diffusion within the crystal lattice prompted us to develop a nanostructured HTO which provides incorporated Li with a short diffusion length inside nano-crystal.

The Li diffusion dynamics inside the crystal structure are highly important features that determine the energy and power densities of electrode materials, because, in many Li storage materials Li migration inside the crystal during charging/discharging processes is the rate limiting step [51-53]. When a Li is incorporated at the interstitial sites, electronic charges are distributed over the Ti atoms that are adjacent to Li. The localized electrons which are trapped as small polarons undergo thermally activated hopping between available sites, and the collective migrations of Li and electrons dominate the overall diffusivity of Li in the crystal structure [39, 54]. To determine the characteristics of Li diffusion inside the atomic crystal of HTO, it is necessary to understand the atomic environment (the relative position of Li, O, and Ti) and discover feasible migration paths [55]. Here, the accelerated Li migration inside HTO crystal is achieved *via* modulating the nano-structure of the material.

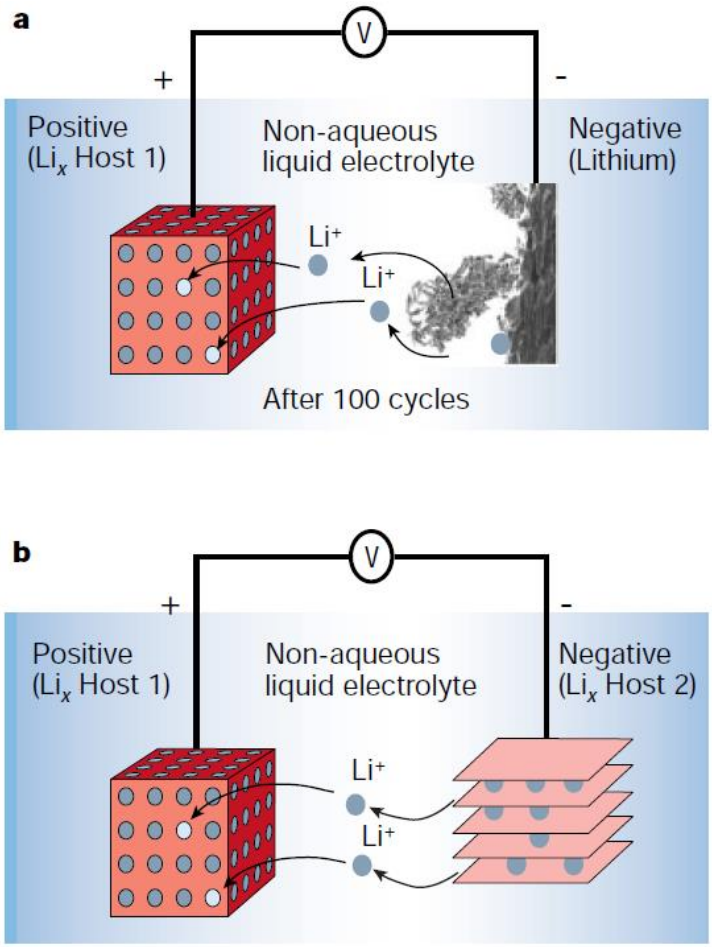

Figure 1-1. Schematic diagram and operating principles of (a) Li-metal battery and (b) LIB. Adapted from J. –M. Tarascon *et al* [1].

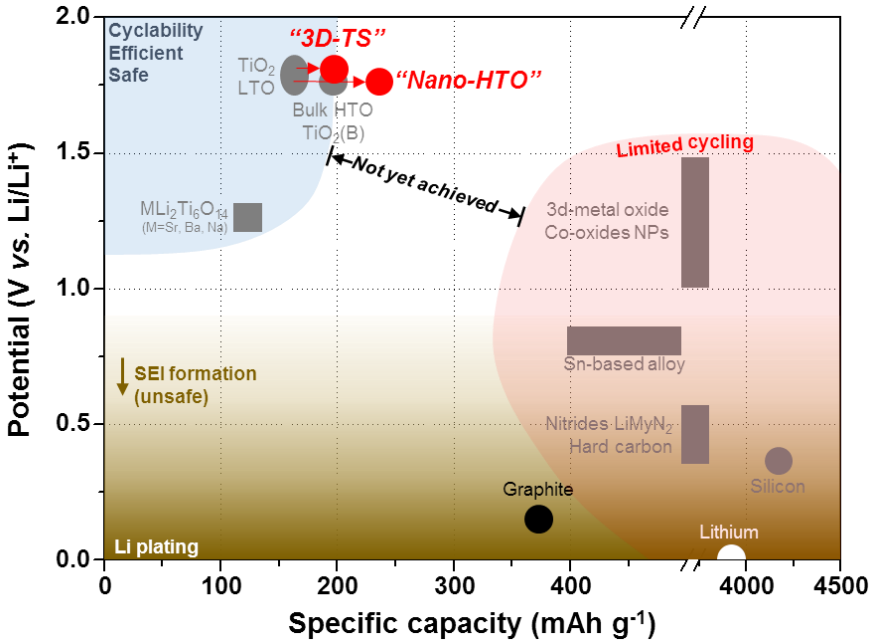

Figure 1-2. Electric potential (in reference to metallic Li, V) *vs.* specific capacity of anode materials for LIB.

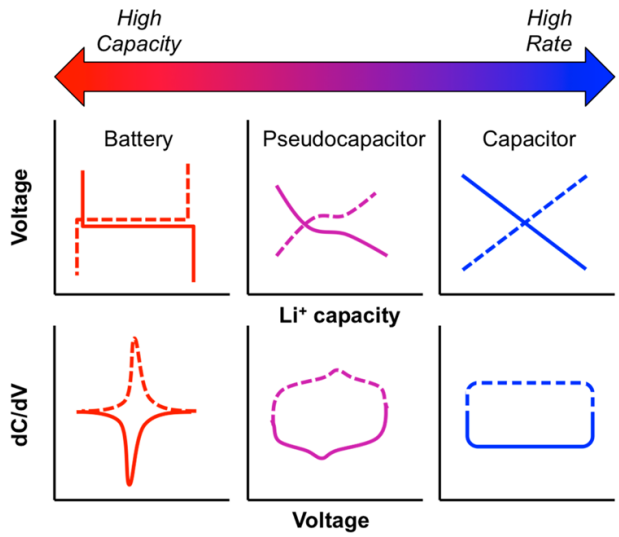

Figure 1-3. Schematic diagram of idealized voltage and differential capacity profiles for three basic charge storage mechanism. Adapted from A. G. Dylla *et al* [29].

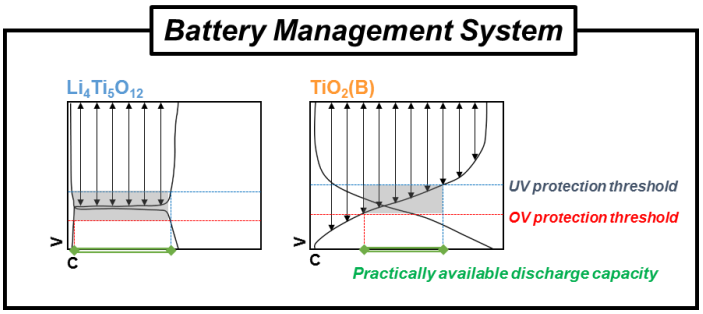

Figure 1-4. Schematic illustrations comparing the voltage profiles of titanium-based high voltage anode materials (LTO, TiO_2(B)). Practically available discharge capacity, under/over-voltage protection thresholds are denoted.

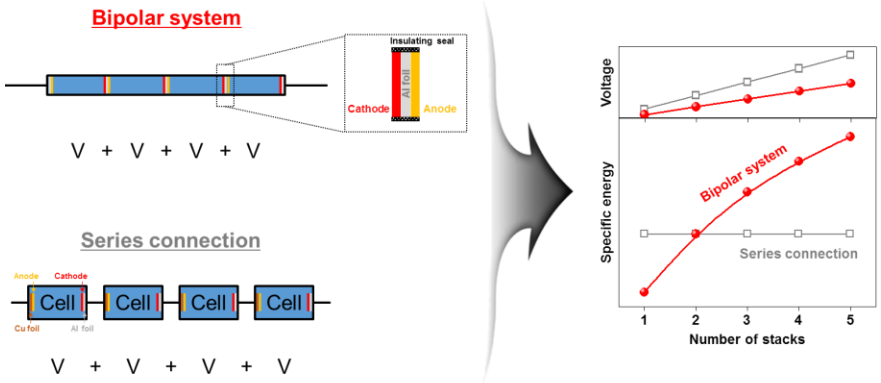

Figure 1-5. Schematic illustrations of bipolar and series connection systems.

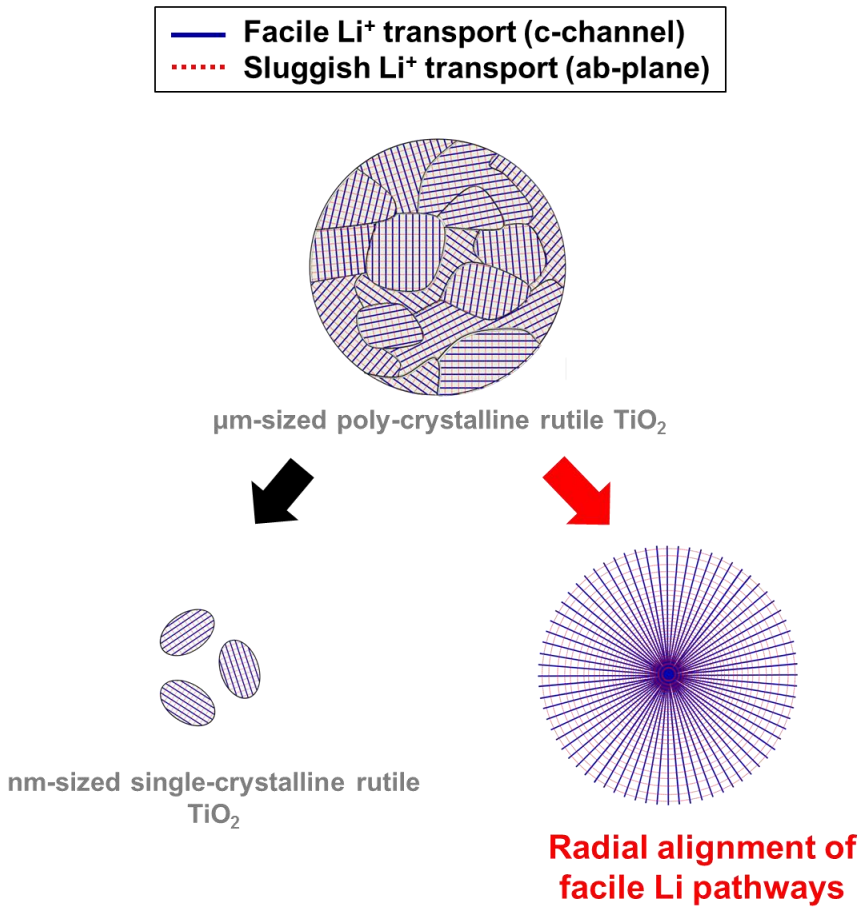

Figure 1-6. Schematic illustration showing the various architectures of rutile TiO_2.

1.2 Toward safe and efficient supercapacitors: Development of hybrid electrode materials

1.2.1 Development of supercapacitors for safe and reliable energy storage systems

Electrochemical capacitors (so-called supercapacitors), with high power density and superior cycling ability, are considered to be one of the most promising systems in the energy storage field. As shown it Figure 1-7, a Ragone plot effectively emphasize power density *vs*. energy density for the primary energy storage systems [56]. High power as well as reasonably high energy density are provided, supercapacitors can become a promising candidate for emerging energy applications. The currently available supercapacitor systems are extentively used in various electronic devices such as consumer electronics, memory back-up systems, and industrial power and energy management [57]. A notable example is that supercapacitors were recently adopted in emergency doors on the Airbus A380, highlights their safe and reliable performance. In near future, supercapacitors are likely to be regarded as a representative energy storage system along with batteries. One of the most predictable applications is its installation in hybrid electric or fuel cell vehicles. Combined with high-energy batteries or fuel cells, the supercapacitor is able to perform a key role in high power demanding conditions such as starting up and acceleration.

1.2.2 Challenges facing supercapacitor

The principle mechanism of energy storage of the supercapacitors is classified in two; capacitive or pseudocapacitive. The capacitive (non-Faradaic) energy storage is the result of charge separation at the interface between electrode and electrolyte. And the pseudocapacitive (Faradaic) process is based on redox reactions that occur in the electrode materials. The most widely used active electrode materials are carbon (e.g. activated carbon, graphene, and carbon nanotube) and transition metal oxide (e.g. MnO_x and RuO_2) [58-68]. The common challenge in supercapacitor design is the resistive behavior originated from sluggish ion transport, poor electrical conductivity, and high charge transfer resistance, which increases equivalent series resistance (ESR) of overall cell [69]. In addition, a variety of activation process (e.g. KOH, NH_3, and CO_2) for the increase of surface area not only are involved in harmful chemicals or toxic metals but also lower its cost-effectiveness [70-73]. Therfore, the development of one-step process based on 'green chemistry', without an additional activation process, would be desirable for future generation of supercapacitor.

1.2.3 Strategy 1: Bicontinuous metal/carbon hybrid as high power supercapacitor electrodes

The use of electrochemical energy storage devices in heavy-duty equipment is expanding (Figure 1-8) [74]. For such applications, it is important to develop

an advanced generation of supercapacitors that have the capability to supply high levels of power [56, 75]. Importantly, the time constant t for ion diffusion ($t=L^2/D$) and the internal resistance for electron transport ($R=\rho L/A$) are the major factors that are responsible for the limited power of such devices [76-83]. Thus, in attempts to reduce ion and electron transfer length (L) and minimize resistive behavior, a diversity of nano-structured electrode materials have been developed, such as controlled arrays of nanowires and carbon nanotubes, microchips based on onion-like carbon nanoparticles and vertically oriented graphene nanosheets [80-84]. These reported methods, however, are only be applicable to film-type or nano-structured electrodes, which are unfit for practical and industrial usage on account of insufficient stored energy in the overall electrode. In this context, high-volume production and increasing the loading capacity of electrode materials without performance fading represents a substantial challenge in this field.

Fundamentally, the development of bulk electrodes for supercapacitor systems with ultrahigh fast rate capabilities are required to minimize primary resistance during charge/discharge cycles, ion transfer interference by complex inner pores, and electronic resistance between the electrode and current collector [76-79, 85, 86]. Recently, a 3D structured metal that has the ability of ensuring electrode material polarization through its electronic conductivity was proposed as another possible solution. Among fabrication methods, selective etching of a bimetallic alloy (e.g. Ag-Au) is a representative method for achieving 3D metallic structures with uniformity [85]. In addition, as a bottom-up approach, H. Zhang et al. proposed the preparation method of

electrodeposited 3D metallic structures using polystyrene beads as a template and successfully proved their performance in a fast-operating battery system [86]. However, some technical bottle-necks still remain in the application of 3D metallic architectures to electrodes for energy storage. First, a significant loss of noble metals and detrimental procedure during acid etching are inevitable in 3D fabrication including the dealloying process. Two-step fabrication (electrode material loading after 3D structuring) also causes weak connections between the electrode material and 3D metal, which is an important attribute of charge transfer resistance. To address these issues, in the present work, a one-step fabrication method for preparing an electrode with a 3D metallic structure and carbon-based electrode material was developed, which mimics the structure of the brain coral in the ocean [87]. The metallic structure and carbon without inner pores are integrated into a bicontinuous architecture with a large contact area and strong interfacial bonding. It allows ion transfer to active sites of the electrode surface and charge transfer between two components in the electrode to be facilitated. The high volume production of a biocontinuous electrode with an excellent power density of greater than 40 kW kg^{-1} is described (based on the mass of electrode material). This value is one of the highly outstanding performance reported for the carbon-based supercapacitor electrodes [76-89].

1.2.4 Strategy 2: Hybrid MnO_2 film for enhancing the structural integrity of thin film supercapacitor electrodes

Many attempts have been made to improve the energy/power density of energy storage systems (ESS) by introducing thin film architectures to electrode materials. Certain types of thin film electrode materials reported show low ion diffusion length and reduced electron transfer resistance that are related to the major properties of the next generation ESS [90-94]. Until now, however, there are problems associated with thin film electrodes, including a short life cycle and limitations in thickness. More importantly, the development of film-type electrodes that are capable of storing more energy per unit area has become an urgent issue in order to meet future demands of the electronics industry.

One of the fatal problems for the practical use is the fragile characteristics of thin film-type materials. As an example, anodic/cathodic electrodeposition is one of the most controllable approaches for the fabrication of thin film electrodes [95, 96]. In this method, it is possible to precisely control the film thickness and morphology of active materials [97-100]. Nevertheless, disintegration of the deposited layer results in contact failure between the active material film and the current collector. This is closely related to the fading in the performance of energy storage devices [101, 102]. This characteristic is common across all techniques associated with thin film fabrication and it is highly dependent on the adhesion and thickness of the active layer as well as the formation of cracks in the deposited films.

In order to find a solution to these issues, I research herein the synthesis of a robust metal oxide thin film by agarose gel wrapping. An agarose gel was coated on a metallic current collector prior to the electrodeposition of an active metal oxide. Agarose gels are comprised of a polymer matrix with sub-

micrometer pores (pore sizes of 400~500 nm) and high elasticity (Young's modulus of 116 kPa) [103, 104]. Such hydrogels show, not only great film-forming ability on a substrate during the sol-gel process but also have a high accessibility for an ionic metal precursor and an electrolyte in aqueous solution [105-107].

The proof-of-concept research is based on the preparation of manganese dioxide (MnO_2) films for use in supercapacitor applications. As a pseudocapacitive electrode material, MnO_2 has attracted considerable interest due to its properties that include a high theoretical specific capacitance (1370 F g^{-1}), low cost and the fact that it is environmentally benign [96, 108]. However, the major problem associated with MnO_2 is the high charge-transfer resistance between the MnO_2 film and the metallic current collector, which can be attributed to the low adhesion of such films [96]. In addition, in the case when the amount of MnO_2 deposited is increased, film contact to the current collector becomes deteriorated due to film shrinkage during the oxidation of Mn hydroxide [101, 102]. Therefore, an upper limit exists for capacitance per unit area of the current collector. For this reason, an electrodeposited MnO_2 film was selected as a representative model material to prove the effect of agarose gel hybridization.

In this study, the electrochemical performance and morphology of an agarose gel-wrapped MnO_2 architecture were evaluated. Also, 3D finite element (FEM) simulations and the first-principles calculations were performed to verify the superior elastic properties and ion accessibility of the agarose gel layer, respectively. The results indicate that this hybrid electrode exhibits a high areal

capacitance (52.55 mF cm^{-2}) that is 5 times higher than that of the control sample, which can be attributed to the elastic gel-wrapping effect.

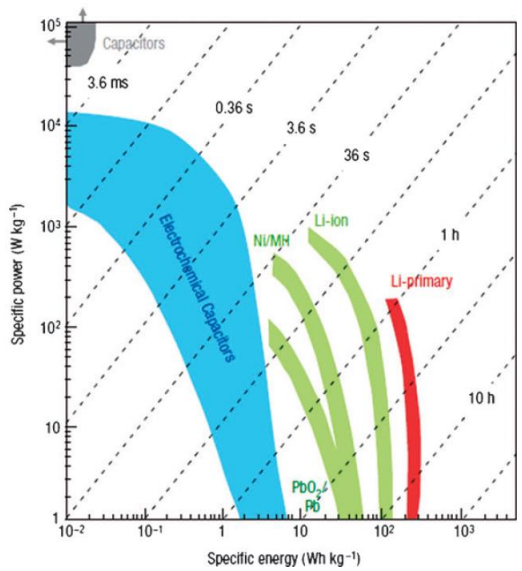

Figure 1-7. Ragone plot (specific power *vs.* specific energy) for various electrochemical energy storage devices. Adapted from P. Simon *et al* [56].

Figure 1-8. Hybrid diesel/electric rubber-tired gantry crane with DLCAP electrochemical capacitor energy storage system (fuel saving of 40 % are typical). Adapted from J. R. Miller *et al* [74].

1.3 A system level approach to construct robust energy storage platform enduring mechanical stress

The emergence of body-centric power generators such as piezoelectric/solar cell and the functional/morphological evolution of smart phones have created a need for advanced devices for energy storage. In order to meet the power demand of such devices, the construction of a series of unconventional energy storage systems (ESS) have been reported in the past few years, which enable one to achieve flexible, foldable, and stretchable characteristics [109-114]. A prototype ESS for the future was recently proposed, and such explorations bring up a new trend for wearable energy [115].

The primary requirements of electrode materials for use in wearable ESS include electrical connectivity and mechanical endurance. The electrical connectivity of randomly distributed electrode materials can be explained by the percolation threshold, a mathematical term derived from percolation theory [116]. I. Balberg et al., reported that the use of a conducting stick with a high aspect ratio results in a percolation threshold much lower than that for round-shaped materials [117]. Thus, carbon nanotubes (CNTs), which have outstanding mechanical properties (Young's modulus of 270~950 GPa, tensile strength of 11~63 GPa) have been selected and extensively studied as a pioneer electrode materials for use in advanced thin and wearable supercapacitor devices [118]. In this context, various fabrication techniques for CNT films including the Landmuir-Blodgett technique [119], vacuum filtering [120], drying drop [121], and chemical vapor deposition [122] were developed, and

web-like networks of CNT building units show unique and superior mechanical robustness, thermal stability, and electrical conductivity [123, 124].

Although these advantages are claimed for CNTs, their relatively high production cost and the difficult preparation of stable CNT dispersions are still challenging problems for their practical application as electrodes [125, 126]. A graphene-based electrode was recently proposed as an alternative to CNTs by virtue of its high aspect ratio [127, 128]. However, a 2-dimensional electrical path and the extensive agglomeration of the exfoliated graphene sheet continue to pose a hurdle [129]. Therefore, the development of a new type of conducting network with a negligible level of percolation threshold that can maintain electrical conductivity under an extraordinarily deformed state has become an urgent issue in order to meet future demands of wearable electronics.

As is well known, A. K. Geim and K. S. Novoselov extracted graphene from a sample of graphite using ordinary adhesive tape [130]. This history suggests that exfoliation by utilizing the adhesive properties of commercial tape could be effectively applied to constructing a thin layer comprised of bulk materials. In the present research, inspired by the discovery of graphene, I propose a 'lint taping' method to fabricate thin layer of conducting network using graphite felt (referred to herein as GFCN). This direct solid-to-solid transfer approach is highly effective for constructing a well-distributed conductive network, as discussed below. Graphite felt consists of tubular-shaped carbon fiber with an average diameter of below 10 μm. The carbon fiber has high aspect ratio (length/diameter>1715) and conductivity (~260 S cm^{-1}) that approaches that of CNTs by virtue of graphitic characteristics [131]. In this method, the tape film

functions as a flexible substrate. More importantly, the adhesive strength of the tape not only allows the conducting network to maintain its structural integrity but assists the processes of device assembling.

In this dissertation, by adopting it as a supercapacitor electrode, the physical characteristics and electrochemical properties of such a GFCN are identified. The final wearable system is symmetrically constructed by using the GFCN on tape and a polymer electrolyte composed of polyvinyl alcohol (PVA)/phosphoric acid (H_3PO_4). This energy storage platform was stable in extremely severe mechanical tests while showing a capacitive performance comparable to those of the conventional carbon-based counterparts. Furthermore, the integrated-cloth based system showed stable capacitive behavior even after laundering in a commercial washing machine.

1.4 Objectives

This thesis mainly consists of the development of (1) titanium-based high voltage anode materials, (2) hybrid supercapacitor electrode materials, and (3) robust energy storage platform with resistance to mechanical stress.

Following this introduction,

(1) In Chapter 2 and 3, the 3D TiO_2 nanospheres with radially aligned *c*-channel nanorods and the hydrogenated titanate with a novel atomic/nano-architecture are discussed. The facilitated Li diffusion inside the *c*-channel specialized TiO_2 structure allows it to exhibit enhanced Li storage performance. And, a bundle of $H_2Ti_{12}O_{25}$ nanorods which confers significantly shortened diffusion length is successfully synthesized for the construction of outperforming $H_2Ti_{12}O_{25}$.

(2) In Chapter 4 and 5, the 3D metal-carbon bicontinuous architecture and the hybrid MnO_2 film are presented. The facilitated ion transfer to electrode surface and charge transfer dramatically increase the power density of metal-carbon hybrid structure. And, the substrate adhesiveness of the agarose gel, which is hybridized with MnO_2, successfully improve the structural integrity of thin film electrode even at high MnO_2 loadings.

(3) In Chapter 6, the fabrication of an all-solid-state, foldable and washable energy storage plaform using simple ‘lint taping’ method were proposed.

The combination of theoretical proof, physical methodologies, and applications in the enegy problem together with the fundamental importance of developing a new architecture emphasize stongly the value of proposed electrode materials with high safety and stability.

Chapter 2. Radial Alignment of *c*-Channel Nanorods in 3D Porous TiO_2 for Eliciting Enhanced Li Storage Performance

2.1 Experimental

2.1.1 Preparation of TiO_2 materials

The synthesis of the 3D-TS was achieved in a bicontinuous emulsion phase formed from Winsor type III system. Deionized water (D.I. water), cyclohexane, and magnesium stearate (Mg-stearate) was used for the preparation of Winsor type III ternary system composed of water, oil, and surfactant, respectively. First, 0.77 g of Mg-stearate (Riedel-de Haën) was dissolved in 30 ml of 2.6 M HCl (35~37%, Samchun) (Solution A). Titanium n-butoxide (4.06 ml, 97% purity, Aldrich) and 4.5 ml of n-amyl alcohol (99%, Samchun) were added to 30 ml of cyclohexane (≥99%, Sigma-Aldrich) and the resulting solution was vigorously stirred for 20 min at room temperature (Solution B). Solutions A and B were mixed and additionally stirred for 30 min at room temperature. The mixture, composed of three different phases (oil-emulsion-water), was transferred into a 150 ml Teflon-sealed autoclave and maintained at 150 °C for 4 h. After cooling to room temperature, the reaction mixture was centrifuged and washed with ethanol three times (Figure 2-1). The product was dried at 70

°C to obtain the final 3D-TS. In the synthetic process, about 90% of the titanium in the titanium n-butoxide is converted into TiO_2 in the 3D-TS (Table 2-1). Among the TiO_2 counterparts, micrometer-sized and poly-crystalline rutile TiO_2 particles (pc-TiO_2) were present, as has been previously reported [132]. Briefly, methanol, acetonitrile, water, dodecylamine, and titanium isopropoxide were mixed and used in hydrolysis and condensation reaction. The products were calcined in air at 700 °C for 4 h to obtain the final pc-TiO_2. The nanometer-sized, single-crystalline rutile TiO_2 particles were obtained from commercially available products (nano-TiO_2, Tayca, MT-100AQ).

2.1.2 Characterizations

The surface morphology of the samples was characterized by scanning electron microscopy (SEM, Carl Zeiss, SUPRA 55VP). An X-ray diffractometer (XRD, Rigaku, D/max-2200) was utilized to investigate crystalline structure of the TiO_2 samples. Bright-field transmission electron microscope (TEM) images and selected-area electron diffraction (SAED) pattern were collected by analytical TEM (JEOL, JEM-2100F). Nitrogen adsorption and desorption isotherm were measured using ASAP 2010 Micromeritics apparatus.

2.1.3 Electrochemical measurements

Electrochemical experiments were performed using a conventional coin cell (CR2032) assembled in an Ar-filled glove box. A lithium foil and microporous polypropylenes were used as the counter electrode and separator, respectively. The working electrode was prepared by mixing 80% w/w of the TiO_2 active materials, 10% w/w conductive carbon (Super P) and 10% w/w poly(vinylidene difluoride) binder for Li ion cells. The mixture was blended with a few drops of N-methyl-2-pyrrolidone (NMP, Sigma-Aldrich) to produce slurry. The resulting slurries were casted on Cu foils by doctor blading and vacuum-dried at 120 °C for 12 h. After roller compression, film-type electrodes were obtained. A 1.15 M $LiPF_6$ solution of dissolved in 3:5:2 (v/v/v) ethylene carbonate/ethyl-methyl carbonate/diethyl carbonate were adopted as an electrolyte. Galvanostatic charge/discharge analyses were performed with an automatic battery cycler (WBCS3000, Wonatech) at ambient temperature (30 °C). Electrochemical impedance spectroscopy (EIS) was conducted using a computer-controlled potentiostat (ZIVE SP2, WonaTech) at E=1.85 V after 30 charge/discharge cycles. The frequency range was 10 mHz ~ 100 kHz under AC stimulus with a 10 mV amplitude. The parameters of the equivalent circuit were calculated by using ZMAN software.

2.1.4 Computational details

Periodic density functional theory (DFT) calculations were carried out using

the Vienna ab initio simulation package (VASP) [133]. The generalized gradient approximation (GGA) parameterized by Perdew-Burke-Ernzerhof (PBE) exchange-correlation functional was employed [134]. Ionic cores were described by the projector augmented wave (PAW) method [135]. The wave functions were constructed from the expansion of planewaves with an energy cutoff 400 eV. A 3 x 3 x 3 Monkhorst-Pack k-point mesh was used to sample the Brillioun zone. All calculations were converged until the forces on all atoms were less than 0.03 eV $Å^{-1}$. The electronic optimization steps were converged self-consistently to $<10^{-6}$ eV. DFT+U within Dudarev's approach was used with U_{eff} = 4.2 to account for the on-site Coulomb interaction in the localized *d* orbital [136]. This U value has been obtained by fitting to experimental data the splitting between occupied and unoccupied Ti *d* states for oxygen vacancy states at the (110) surface of rutile TiO_2 [137], and has been used to model oxygen vacancies at other rutile surfaces [138], Nb and Ta substitution [139], and oxygen vacancy and Ti interstitial formation in rutile and anatase TiO_2 [140]. For the calculation of bulk optimization, the cutoff energy was increased to 520 eV. The surface was constructed by cleaving the optimized bulk structure along the (001) and (110) surfaces. To prevent in-physical electronic interactions, a 10 Å of vacuum region space between the slabs was added. Both (001) and (110) surfaces largely consisted of 3 layers and the top 2 layers were allowed to relax while the residual bottom layer was fixed. The transition state was located using the climbing image-nudged elastic band (CI-NEB) method [141, 142]. Seven spaced images were obtained by linear interpolation and used as initial trajectories for migration path. In the CI-NEB calculations, the images

were refined until the maximum atomic forces are converged within 0.1 eV $Å^{-1}$. The difference in charge densities during Li migration was calculated using following equation: $\Delta\rho = \rho LiTiO - (\rho TiO + \rho Li)$ where $\rho LiTiO$ is the total charge density of the LiTiO system, ρTiO and ρLi are the charge densities of the TiO systems without Li and isolated Li atom, respectively [143, 144].

2.2 Results and discussion

2.2.1 Li diffusion dynamics inside rutile TiO_2

There are two feasible pathways for the migration of Li inside rutile TiO_2 as illustrated in Figure 2-2(a) and Figure 2-3. Li can migrate (i) along the ab-plane in the [110] direction and (ii) through the c-channel in the [001] direction. Previous efforts have been made to evaluate Li diffusion in the rutile phase by means of quantum mechanical and molecular dynamic methods [145, 146]. These studies shared a common interest in the anisotropic diffusion of Li in a rutile phase. To examine the degree of anisotropy of a Li diffusion process more accurately, the evolution of energetics was tracked, and corresponding energy barriers to Li migration was extracted using density functional theory (DFT) calculations with the climbing image-nudged elastic band (CI-NEB) method. Figure 2-2(b) shows the relative energies as a function of the Li movement along the straight line projected between two Li octahedral sites for both paths (ab-plane and c-channel). The calculated energy barrier for the c-channel is 0.05 eV which is 37 times lower than that for the ab-plane (1.83 eV). This suggests

that the migration of Li along the c-channel is highly favored inside rutile TiO_2.

At the saddle point corresponding to the highest energy level along the ab-plane migration, Li is located in the tetrahedral site, surrounded by three octahedral Ti sites (two plane-sharing octahedral Ti site and an edge-sharing octahedral Ti site). In this situation, the localization of 3*d* electrons occurs along with extensive Ti network. In addition, the binding between trapped electrons and Li contains remarkably insufficient interaction due to electrostatic screening of the nearest oxygen atoms, which can be confirmed by the resulting variations in the charge densities (Figure 2-2(c)). It should be noted that there is a strong preference for electron trap in the lithium interstitial vicinity as mentioned above [38]. On the other hand, the intensive localization of electrons over adjacent Ti sites forms a complete Li-Ti cluster which is consistently maintained for all locations of Li on the c-channel path (Figure 2-2(d)). These results show an extraordinarily low energy barrier level in the c-channel, which is in agreement with previous reports [145, 146]. Importantly, this severe anisotropy of Li diffusion provides us the rationale to design a 3D-TS that accommodates radially aligned c-channels.

2.2.2 Synthesis of 3D-TS

In order to synthesize a 3D-TS which is comprised of radially assembled TiO_2 rods, a synthetic method was developed utilizing bicontinuous emulsion phase of Winsor type III system where both hydrolysis and condensation reactions of a titanium precursor (titanium n-butoxide) occur. Winsor type III

is a three-phase system, in which the bicontinuous microemulsion phase coexists with excess water phase at the bottom and excess oil phase at the top (Figure 2-4(a)). The process of sequential hydrolysis, condensation, protrusion, and maturation is described in Figure 2-4(b-e).

At the initial stage of the reaction (Figure 2-4(b)), the titanium n-butoxide is located in the oil phase (cyclohexane) due to the hydrophobic nature of the tert-butoxide ligands ($(O\text{-}C_4H_9)_4$) [147]. The surfactant (Mg-stearate) exists at the oil/water interface, and this eventually leads to the formation of a bicontinuous emulsion phase (3ϕ) when the desired amounts of water, oil, and surfactant are mixed. The titanium n-butoxide in cyclohexane is steadily hydrolyzed and the products pass into the water phase and the condensation reaction of titanium hydroxide ($Ti(OH)_4 \rightarrow TiO_2$) follows. During the condensation reaction to TiO_2, the high acidity of the water phase (2.6 M of HCl) leads to edge-shared linking and corner-shared bonding of the $[TiO_6]$ octahedron, which results in the formation of the rutile phase of TiO_2 [148]. The $[TiO_6]$ octahedrons are linked by sharing two opposite edges to form chains along the c-axis, which is closely related to the c-channel, namely 'Li highway'. After this series of sequential reactions, primary rutile nanocrystallites are produced, as evidenced by the SEM image of Figure 2-4(b).

After the formation of primary TiO_2 nanoparticles, the secondary crystal growth begins (Figure 2-4(c)). During the secondary crystal growth of TiO_2, the generation of curvatures (denoted in Figure 2-4(c)) at the oil/water interface is important for determining the spherical shape of the 3D-TS. The driving force for the generation of curvature is a tendency to maintain a charge balance at the

oil/water interface. The hydrolyzed titanium hydroxides (in the acidic water phase) that have a positive charge and head-groups of the anionic surfactant are stably bound and neutralized by Coulomb interactions. As the titanium hydroxides are converted into non-ionizing TiO_2 during the condensation reaction, the TiO_2 rods that are compressed together to sustain charge balance. In this situation, the interfacial area between the oil and water, where the head-group of the surfactant is located, are continuously increased, and the curvatures begin to protrude. In the end, the protruded curvatures form a closed structure with a spherical morphology [149]. Figure 2-4(c) and (d) display schematic illustrations and corresponding SEM images explain the extrusive evolution.

The assembly of TiO_2 nanorods separated from the oil/water interface undergoes a maturation process (Figure 2-4(e)). In the process, the titanium hydroxides in water phase are continually accessible to the TiO_2 assembly for the construction of fresh TiO_2 rods and to prolong pre-existing TiO_2 rods. This maturation process allows the overall surface energy to be minimized.

As a result, a sub-micrometer sized 3D-TS composed of radially and densely packed TiO_2 rods was obtained after the solvothermal reaction. In this method, the size and compactness of TiO_2 nanorods constituting the 3D-TS is determined by the amount of HCl compared to titanium n-butoxide (Figure 2-5).

2.2.3 Characterization of 3D-TS

The X-ray diffraction (XRD) pattern (Figure 2-6(a)) shows that the

synthesized 3D-TS consists of a rutile crystals (JCPDS No. 21-1276). As indicated by the low and high magnified scanning electron microscopy (SEM) images in Figure 2-6(b), the 3D-TSs were synthesized with high uniformity and their spherical morphology is well constructed by the assembly of TiO_2 rods. Transmission electron microscopy (TEM) images in Figure 2-6(c) show the radially assembled state of the TiO_2 rods with a rectangular parallelepiped shape. A lattice resolved high-resolution TEM image of the tip region of the 3D-TS shows that (001) lattice planes are visible and perpendicular to the rod axis with single crystallinity (Figure 2-6(d)). The lattice spacing of 0.296 and 0.325 nm are attributed to the (001) and (110) planes of rutile TiO_2, respectively. The selected-area electron diffraction (SAED) pattern was recorded along the [001] zone axis, thus indicating the growth direction of the nanorods (Figure 2-6e). These results verify that single-crystalline TiO_2 nanorods constituting 3D-TS are produced and grow along the [001] direction.

The porous structure of the 3D-TS was investigated using N_2 adsorption-desorption and the results are displayed in Figure 2-7. The 3D-TS exhibited a type IV isotherm with a H2 type hysteresis loop in the relative pressure range of 0.6 ~ 1.0, indicating the existence of various sized mesopores (Figure 2-7(a)) [150]. The pore size distribution (Figure 2-7(b), calculated from the desorption branch using the Barrett-Joyner-Halenda method) confirms the multimodal pore size distribution, which consists of a relatively sharp peak (4 nm), a feeble shoulder peak (6 nm), and a broad peak (8 nm). This distribution arises from the interior space of hierarchical structure containing radially assembled TiO_2 nanorods. The overall surface area (calculated using the Brunauer-Emmett-

Teller theory) is ~82.9 m^2 g^{-1}. Quantified properties are summarized in Table 2-3.

2.2.4 Anisotropic growth of TiO_2 nanorods

As discussed above, our main objective is to produce [001]-directionally overgrown TiO_2 nanorods with sufficient aspect ratio. In the early stage of 3D-TS formation, the secondary crystal growth of primary TiO_2 nanoparticles is critical, because it is a decisive step in forming the final architecture of the TiO_2 rods on an atomic scale (Figure 2-4(b) and (c)). Some efforts have been previously made to develop the anisotropic [001] growth of rutile TiO_2 for use in Li storage or dye-sensitized solar cells [151-153]. Although some noticeable features were exploited by varying the synthesis conditions (temperature, acidity, etc.), the underlying mechanism responsible for the anisotropic growth of TiO_2 remains unclear. To elucidate the reason for [001]-directional growth, the role of Cl^- ions that are present in the water phase was examined [154]. Figure 2-6(f) and (g) show the results from our DFT calculations regarding the adsorption of Cl to the (001) and (110) surfaces of rutile TiO_2 (see Figure 2-8 and Table 2-4). The quantified absolute value of the binding energy of Cl to (001) surface range from 0.77 to 2.31 eV which is far lower compared to the case of the (110) surface (2.83~4.27 eV). Therefore, it can be concluded that selectively adsorbed Cl on the (110) facets acts as a shielding layer and prevents the approach of titanium hydroxide. Thus, the TiO_2 growth is occurred only on the (001) surfaces which is not favored to the Cl adsorption (Figure 2-6(h)).

Samples synthesized using phosphoric acid, nitric acid, and acetic acid did not show any anisotropic morphology, which also provides support for the above-mentioned mechanism (Figure 2-9).

2.2.5 Electrochemical analyses

The crystal and nanostructure of the 3D-TS pose significant advantages which permit exceptional Li storage performance for use as anode materials of LIB (Figure 2-10(a)). Galvanostatic charge/discharge is performed between 1.0~3.0 V (*vs.* Li/Li^+) at various rates from 0.2C to 10C. The 1.0C rate here refers to the application of 168 mA g^{-1} [155, 156]. Both micron-sized poly-crystalline rutile TiO_2 (pc-TiO_2) and nano-sized single-crystalline (nano-TiO_2) were adopted as rutile TiO_2 counterparts for their distinctive Li dynamics. Figure 2-11, Figure 2-12, and Table 2-3 show the results of various physicochemical analyses (SEM, TEM, XRD, and N_2 adsorption-desorption) of these control materials.

In general, Li in an electrode material is stored at the electrode/electrolyte interface or inside the bulk crystal, leading to different types of structural behavior. In other words, the insertion of Li can accompany a single-phase solid-solution process or a structural transformation [157]. For the case of pc-TiO_2, which lacking in assembled c-channel nanorods, the poor diffusion in the ab-plane obstructs the Li from moving toward the thermodynamically favorable octahedral sites. In fact, pc-TiO_2 exhibits a very poor capacity (25.5 mAh g^{-1} at 0.2C and 5.3 mAh g^{-1} at 10C) during the repetitive charge/discharge processes

(Figure 2-10(b) and 2-13(a)). As a result, the single-phase solid-solution behavior on small surface area (3.39 m^2 g^{-1}) becomes the predominant Li storage mechanism.

The negligible capacity of pc-TiO_2 explains why earlier investigations dealing with the insertion of Li^+ into TiO_2 undervalued rutile TiO_2 in favor of anatase TiO_2 [158, 159]. In order to resolve this sluggish Li transportation of pc-TiO_2, some researches on nanometer-sized or nanoporous structures of rutile TiO_2 (represented by nano-TiO_2) have been reported about their remarkably improved capacities, which indeed highlight the potential of rutile TiO_2 for use as a Li^+ host material. The overall Li diffusion length is significantly shortened and their single crystallinity is able to resolve the sluggish diffusion. However, when the size is reduced to a nanometer scale, Li surface storage appears to be thermodynamically more favored than bulk insertion [160]. It should be noted that a substantial portion of the capacity of nano-TiO_2 arises from single-phase reaction and therefore can be influenced by surface area, surface site energies, and redox effects [161]. As a result, the nano-TiO_2 showed a moderate capacity of 130 mAh g^{-1} at 0.2C and sloping voltage profiles without a distinctive voltage plateau (Figure 2-10(b)).

The 3D-TS provides Li with a high solid (TiO_2)-solution (electrolyte) interfacial area available for a single-phase reaction. More importantly, the extended c-channel as a conductive pathway can effectively deliver Li to a stable site inside TiO_2 crystal. The Li that accumulates inside c-channels induces a phase transformation of the TiO_2 crystals from TiO_2 rutile with a *P42/mnm* space group to Li_xTiO_2 with a *P2/m* (Figure 2-14). The lithiation of

TiO_2 up to Li/Ti=0.53 resulted in a phase transition toward an intermediated phase, very similar to the original rutile phase but slightly deformed, thus reducing the symmetry to the monoclinic *P2/m* space group [162]. This reversible phase transformation between TiO_2 (*P42/mnm*) and $Li_{0.53}TiO_2$ (*P2/m*) is mainly responsible for creating the noticeable plateau-like regions with centers at 1.85 V. Importantly, the transformation to *P2/m* $Li_{0.53}TiO_2$ is achieved by Li insertion migrating through the c-channel pathway and subsequent deformation of the original *P42/mnm* TiO_2. For this reason, the 3D-TS showed a capacity of 190 mAh g^{-1} (at 0.2C, 10^{th} cycle) and the corresponding composition of $Li_{0.57}TiO_2$ which is similar Li/Ti ratio of $Li_{0.53}TiO_2$.

As shown in the voltage profile and differential capacity of 3D-TS (Figure 2-10(b) and (c)), a voltage plateau region appears between 1.8~2.0 V. These results confirm that the potential-sensitive phase transformation of the 3D-TS is enhanced over that in pc-TiO_2 and nano-TiO_2, while the accompanying capacity increases to 190 mAh g^{-1} at 0.2C. Such a phenomenon has not been reported previously for various types of rutile TiO_2 [44-48].

The initial charge/discharge voltage profiles are presented in Figure 2-15. In the 1^{st} lithiation process, two distinct potential plateaus appear at 2.2 V and 1.4 V. The potential plateau at 1.4 V is commonly found in rutile TiO_2, and has also been reported in the literatures [44, 163]. However, the profile containing plateau at 2.2 V is not consistent with that of other TiO_2 reported previously, and the plateau disappears after 1^{st} cycle. It can be speculated that this unknown plateau originated from the organic impurities and that are completely

decomposed under the oxidative conditions. In fact, CHNS analysis results (carbon content of 2.05 wt. %) revealed the presence of trace amounts of residual surfactants and butyl groups. Even if the 60 mAh g^{-1} from the 2.2 V plateau were not related to the insertion of Li into TiO_2, the 3D-TS was able to accommodate Li up to $Li_{0.8}TiO_2$ (270 mAh g^{-1}) during the 1st lithiation process. Subsequently, 0.57 mol of Li per mol TiO_2 ($Li_{0.57}TiO_2$, 190 mAh g^{-1}) could be cycled reversibly. An irreversible loss in capacity ($Li_{0.23}TiO_2$) during the first charge/discharge was also observed for other TiO_2 polymorphs and nanosized rutile, which is attributed to the irreversible structural change ($Li_{0.85}TiO_2$ with *P2/m* space group) due to the deeper penetration of Li (1.0~1.4 V *vs.* Li/Li^+) [164, 165].

Figure 2-13(a) displays the evolution of capacities which was monitored at various current densities ranging from 0.2C to 10C. The electrode composed of 3D-TS was stably charged and discharged with a nearly 100% Coulombic efficiency regardless of the C-rates and noticeable plateau-like regions with centers at 1.85 V were consistently observed (Figure 2-16). These findings demonstrate the existence of fast and efficient Li^+ insertion/extraction, aided by the radially constructed c-channel. In addition, the 3D-TS assures a low electronic contact resistance between individual TiO_2 particles because the spherical 3D-TS clusters may prefer a closely packed configuration when they are fabricated into an electrode. On the contrary, the nano-TiO_2 underwent severe capacity fading (over 20% of the initial capacity) during the 10 cycles and showed a lower level of rate capability. The inferior cycle/rate performance of the nano-TiO_2 electrode can be mainly attributed to (i) structural collapse

during repetitive cycles (see Figure 2-17) (ii) the increased level of inter-crystallite/particle electron transfer resistance, which increases the overall resistance of the electrode and makes rapid (de)lithiation difficult.

Electrochemical impedance spectroscopy (EIS) analyses were performed to quantitatively determine the difference in electronic/ionic behavior of the 3D-TS and the other two TiO_2-containing materials. Figure 2-13(b) and (c) show Nyquist plots obtained after 30 cycles and an equivalent circuit model for the fitting of the EIS results, respectively [166]. Based on the fitting results, each kinetic parameter was extracted from the experimental data for 3D-TS, nano-TiO_2, and pc-TiO_2 (Table 2-5). Among the kinetic parameters, R_e and R_{ct} correspond to equivalent series resistance and electrolyte/TiO_2 charge transfer resistance, respectively. The values of R_e of three types of TiO_2 are in similar range, while the R_{ct} (41.2 Ω) for 3D-TS is much smaller than those for nano-TiO_2 and pc-TiO_2 (261 Ω and 238 Ω, respectively).

This result confirms the superior conductance of the 3D-TS electrode. R_{ic} arises from resistance caused by TiO_2 inter-crystallite/particle electron transfer. The densely packed 3D-TS electrode provides a favorable configuration for the delivery of electrons across primary crystallites or secondary particles. Therefore, the value of R_{ic} corresponding to 3D-TS (39.3 Ω) is significantly smaller than the corresponding values for nano-TiO_2 (354 Ω) and pc-TiO_2 (305 Ω). The CPEs are the respective constant-phase elements to account for a depressed semicircle in the experimental spectra. Most importantly, Z_w is the Warburg element related to the diffusion of Li inside the bulk crystal and it can be considered to be an index for verifying the high Li mobility of 3D-TS. The

value of the Warburg coefficient (A_W) is the value of the gradient of the Warburg plot. Since A_W is inversely proportional to the square root of the diffusion coefficient, the lower value of A_W (0.037 mΩ $s^{-0.5}$) originates from the outstanding Li transportation ability of the 3D-TS. It is a necessary result that the dynamic range of the phase transition potential (between 0.2C and 1.0C) is smaller in the 3D-TS electrode (~0.02 V) than the corresponding values for the nano-TiO_2 electrode (~0.06 V) and the pc-TiO_2 electrode (undetectable) due to the lower resistance exerted in the 3D-TS (Figure 2-18). In addition, the 3D-TS showed a long cyclic stability without any significant capacity fading (Figure 2-19).

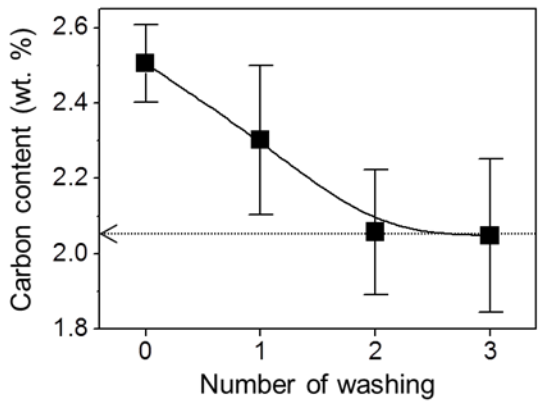

Figure 2-1. The residual carbon contents as a function of washing times for 3D-TS. The identified carbon content of organic impurities were about 2.05 wt. %. An CHNS corder (TruSpec Micro CHNS) was utilized for elemental analyses.

Table 2-1. Yield of 3D-TS.

	Chemical	Quantity (g)	Ti content (g)
Used	Titanium (IV) n-butoxide[a)]	3.94	0.554
Produced	TiO_2 (3D-TS)[b)]	0.839	0.503
		Ti conversion	**90.8%**

a) Reagent grade (97%), Mw=340.32, Density=1.00 g ml^{-1}

b) Mw=79.87, Exclusion of organic impurities

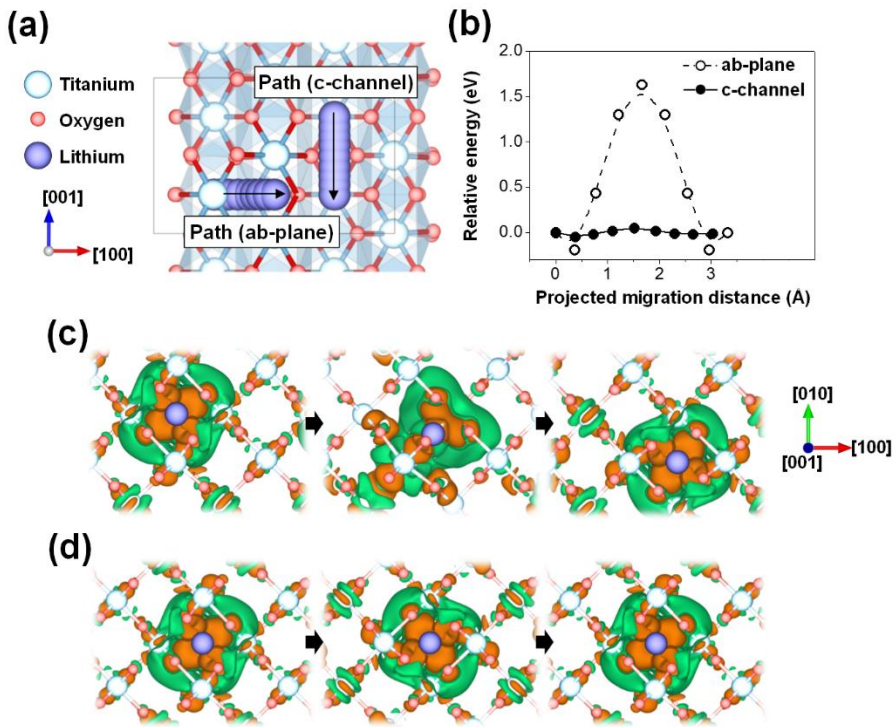

Figure 2-2. (a) Atomic crystal structure of the tetragonal $Li_{0.06}TiO_2$ with a *P42/mnm* space group. The arrows indicate the directions of the diffusion (c-channel and ab-plane). (b) DFT-calculated relative energetics along the different migration paths. The evolutions of differential charge density inside the TiO_2 crystal during (c) Li migration along ab-plane path; (d) Li migration through c-channel path. The left and right images were captured at octahedral positions, and the middle image corresponds to the saddle point with the highest energy level along each Li migration pathway. Brown color indicates a gain of electrons while green shows a loss of electrons. Isosurface levels of all images are 0.5 me $Bohr^{-3}$.

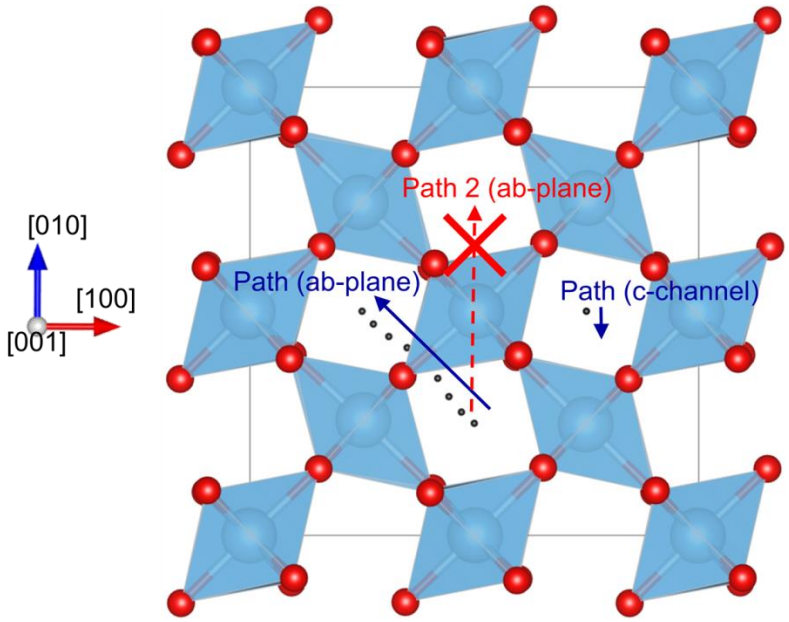

Figure 2-3. Possible Li migration pathways in rutile TiO_2. The path (c-channel) represents Li migration along a c-axis, and path (ab-plane) corresponds to the movement of Li to the nearest neighbor diagonal channel in the [110] direction. Path 2 (ab-plane) corresponds to Li migration in the [010] direction directly through edge-sharing octahedrons, which is not a feasible pathway due to the tremendous energy barrier.

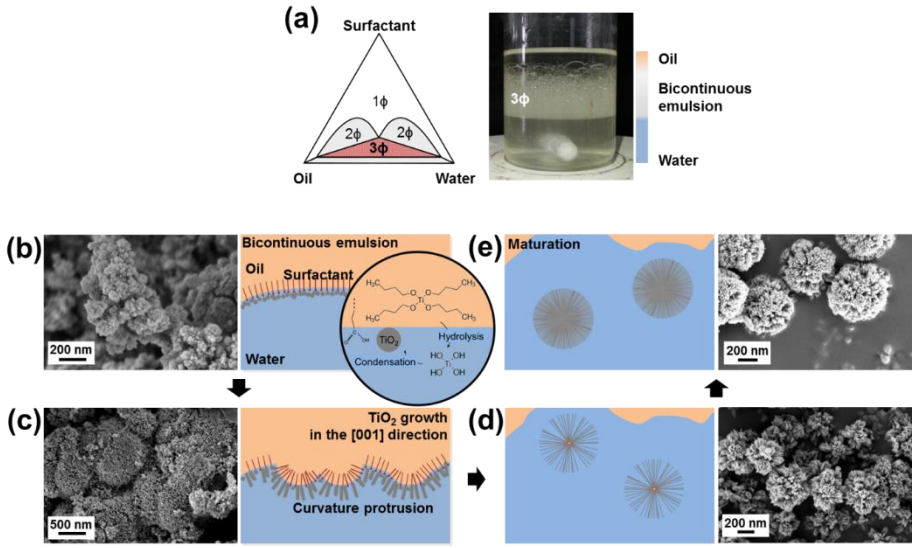

Figure 2-4. (a) Phase behavior of the Winsor III system (left). The term "nϕ" indicates the number of phases, and 3ϕ indicates bicontinuous emulsion phase. Optical image and schematic of Winsor III system (right). (b-e) Schematic illustrations and corresponding SEM images of reaction intermediates of 3D-TS as a function of time (0.5, 1, 2, and 4 h).

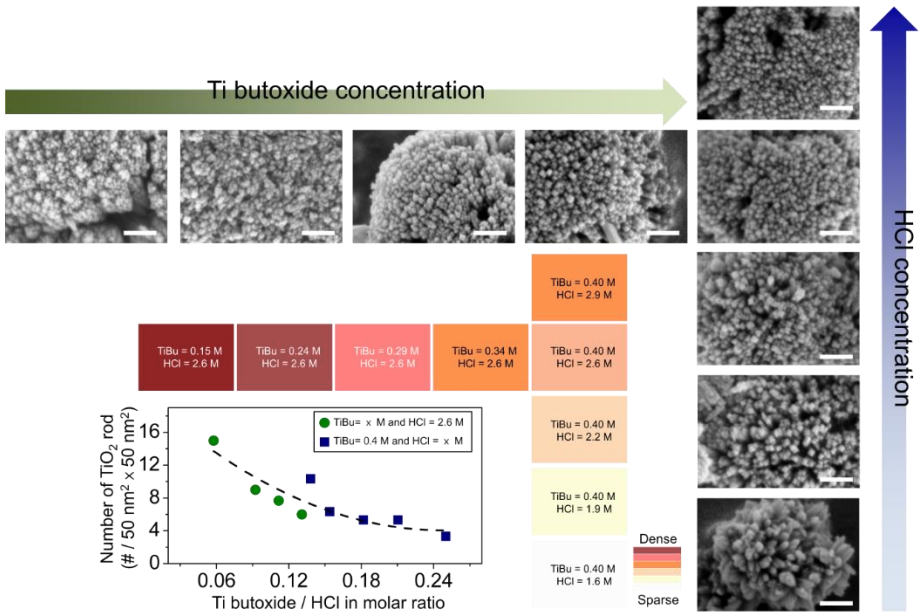

Figure 2-5. Controlling the density of TiO_2 nanorods. SEM images in equal scale of 3D-TS synthesized under the various Ti butoxide/HCl molar ratios (scale bar = 100 nm).

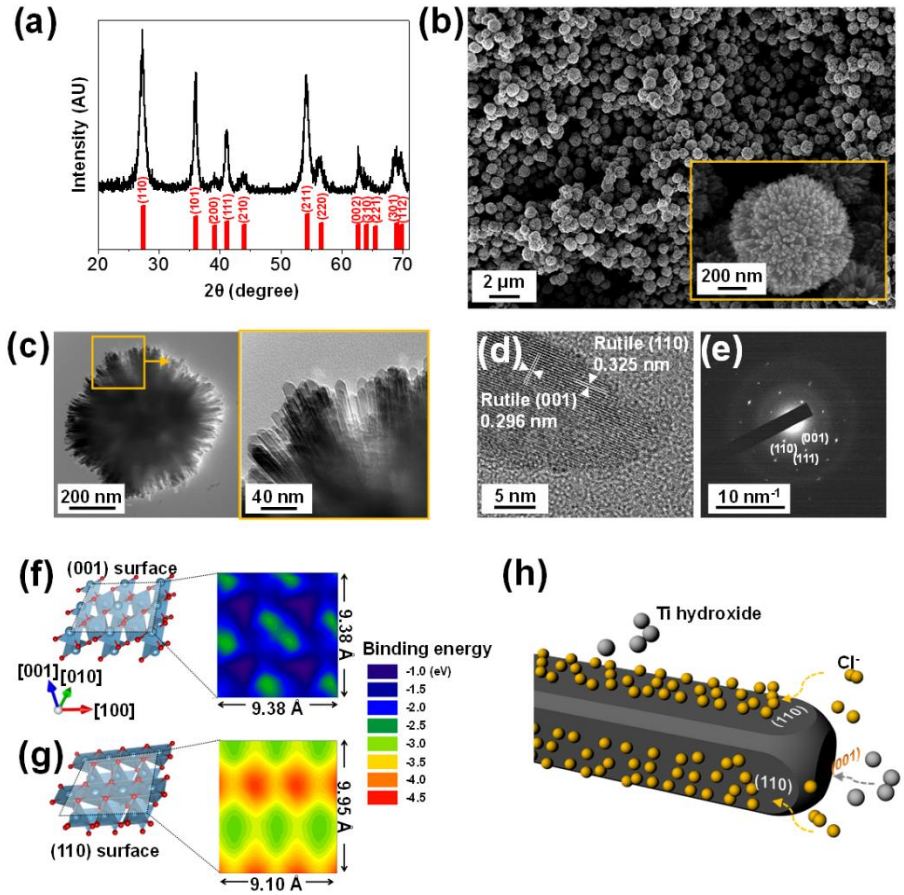

Figure 2-6. (a) XRD pattern and (b) low magnification SEM image and enlarged image (inset) of 3D-TS. (c) TEM images of 3D-TS. (d) TEM image of highly magnified the tip region of the 3D-TS and corresponding (e) SAED pattern. DFT models and contour plots indicating the adsorption energies of single chlorine to (f) (001) and (g) (110) surfaces. (h) Schematic illustration describing the [001] growth of TiO_2 rod in consequence of the surface-selective adsorption of chlorine.

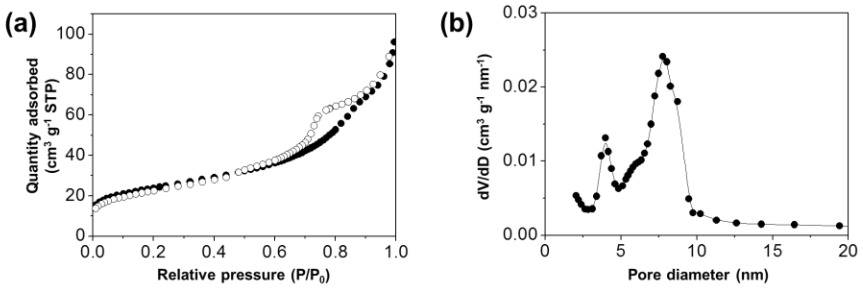

Figure 2-7. (a) Nitrogen adsorption-desorption isotherms and (b) pore size distribution curves of 3D-TS.

Table 2-2. Quantified structural properties of TiO_2.

Parameter	BET surface area	Average pore diameter	Total pore volume
Unit	$m^2\ g^{-1}$	nm	$cm^3\ g^{-1}$
3D-TS	82.9	6.19	0.132
nano-TiO_2	89.6	18.9	0.348
pc-TiO_2	3.39	36.1	0.006

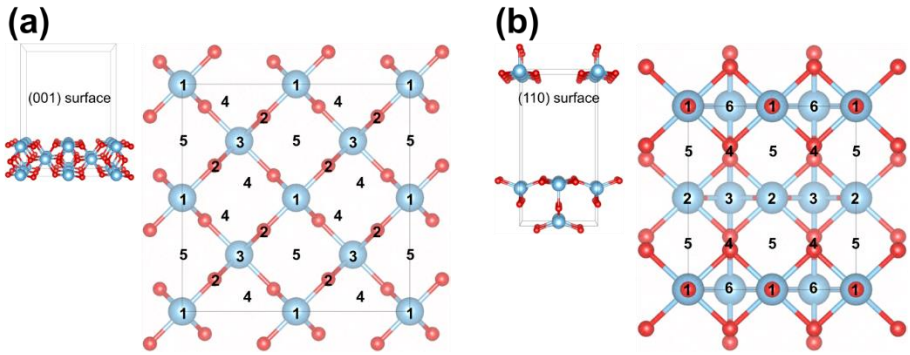

Figure 2-8. The atomic structures of TiO_2 surfaces. A hexahedron represents the boundary of a primitive unit cell (left images of a and b, respectively) and the adsorption positions of chlorine are denoted (right images of a and b, respectively).

Table 2-3. Calculated results of the adsorption energy of Cl to the TiO_2 surfaces. The adsorption positions (#1 ~ #6) are shown in Figure 2-8.

Parameter	Adsorption energy of Cl to TiO_2 surface (eV)	
	(001) Surface	(110) Surface
E_{ads}[a)] (1)	-2.31	-4.27
E_{ads} (2)	-1.47	-3.14
E_{ads} (3)	-0.77	-2.83
E_{ads} (4)	-2.30	-2.99
E_{ads} (5)	-1.43	-3.37
E_{ads} (6)	-	-3.58
Total energy of single Cl atom[b)]	-0.26	-0.26
Total energy of TiO_2 surface	-260.18	-150.29

[a)]Adsorption energy of Cl at × position ($E_{ads}(\times) = E_{Cl\text{-}surface} - E_{Cl} - E_{surface}$); [b)] Single Cl atom is placed in 10 × 10 × 10 $Å^3$ unit cell.

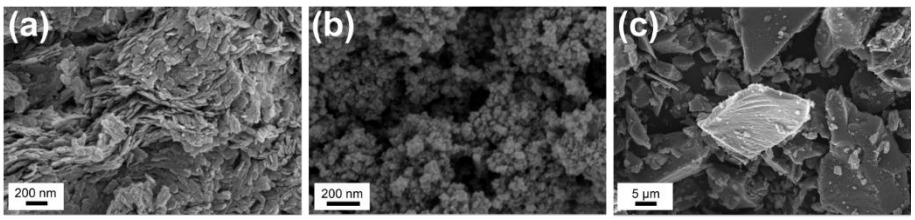

Figure 2-9. SEM images of TiO_2 particles synthesized using dilute, aqueous solutions of H_3PO_4 (a), HNO_3 (b), and CH_3COOH (c). Other synthesis conditions including oil, co-solvent, and surfactant remain unchanged.

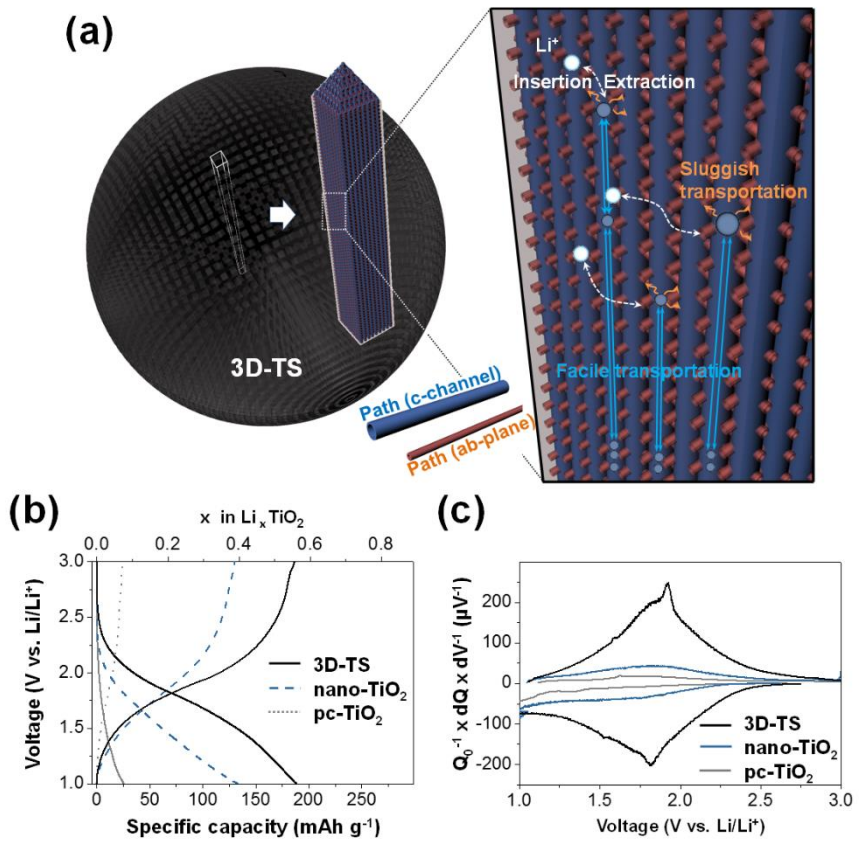

Figure 2-10. (a) Schematic illustration describing architectures of 3D-TS. (b) Galvanostatic 10th charge/discharge voltage profiles and (c) differential capacities of 3D-TS, nano-TiO2, and pc-TiO2 obtained at 0.2C.

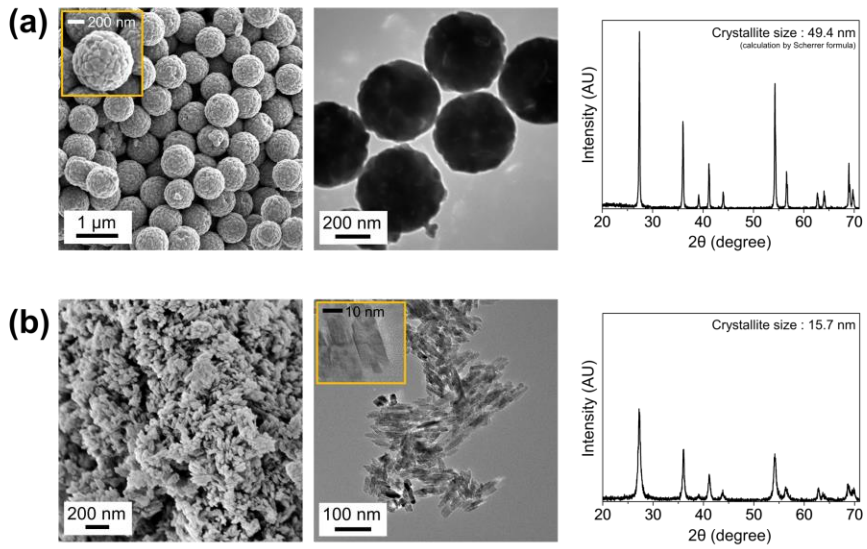

Figure 2-11. SEM, TEM images and XRD pattern of rutile (a) pc-TiO_2 and (b) nano-TiO_2 particles, respectively.

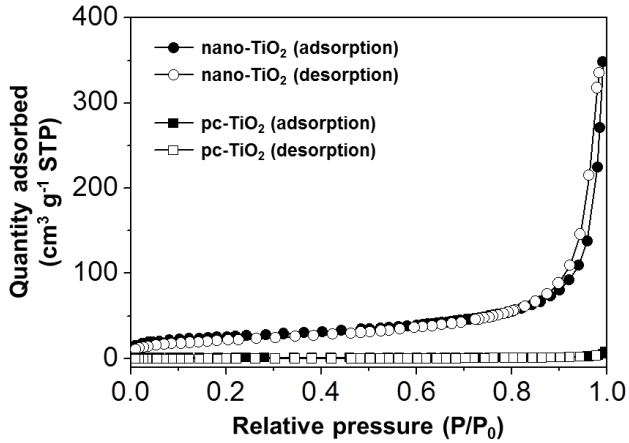

Figure 2-12. Nitrogen adsorption-desorption isotherms of nano-TiO_2 and pc-TiO_2.

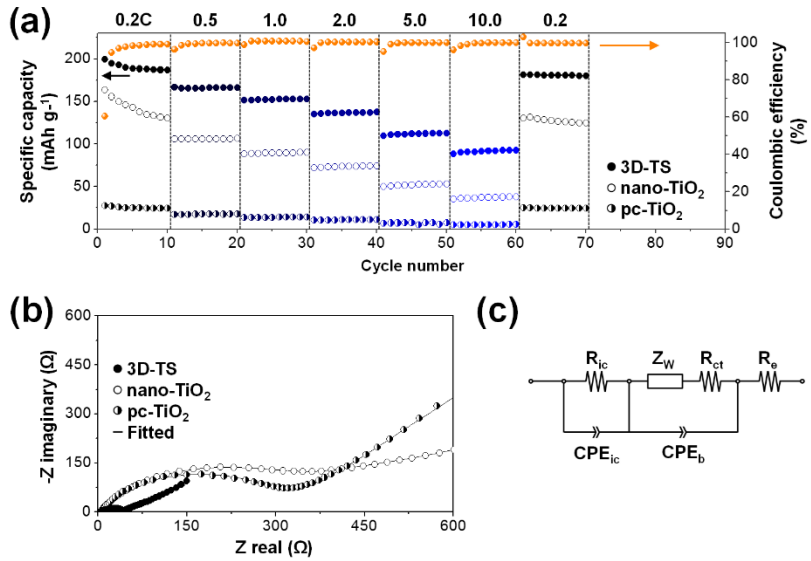

Figure 2-13. (a) Specific capacities of 3D-TS, nano-TiO_2, and pc-TiO_2 cycled at various C-rates. Coulombic efficiencies of 3D-TS are denoted. (b) Nyquist plots obtained from electrodes composed of 3D-TS, nano-TiO_2, and pc-TiO_2. (c) Equivalent circuit model for fitting.

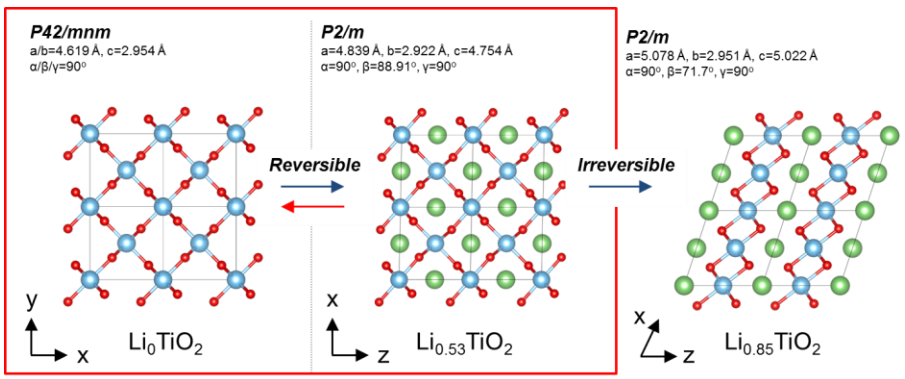

Figure 2-14. Structural evolution of rutile TiO_2 during (de)lithiation process.

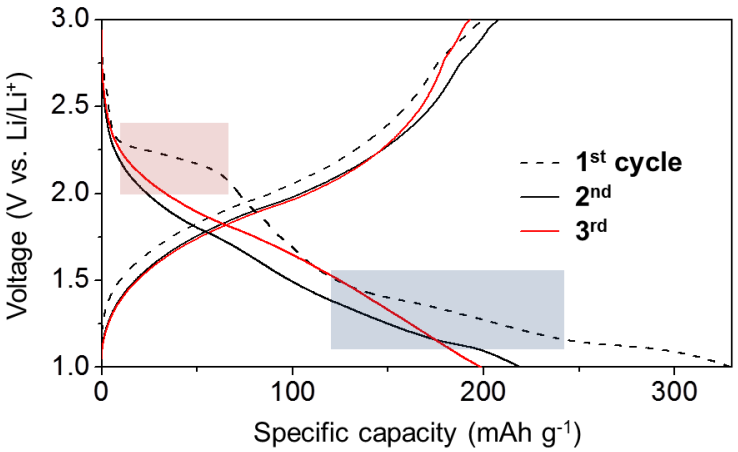

Figure 2-15. First three charge/discharge voltage profiles of 3D-TS at a rate of 0.2C.

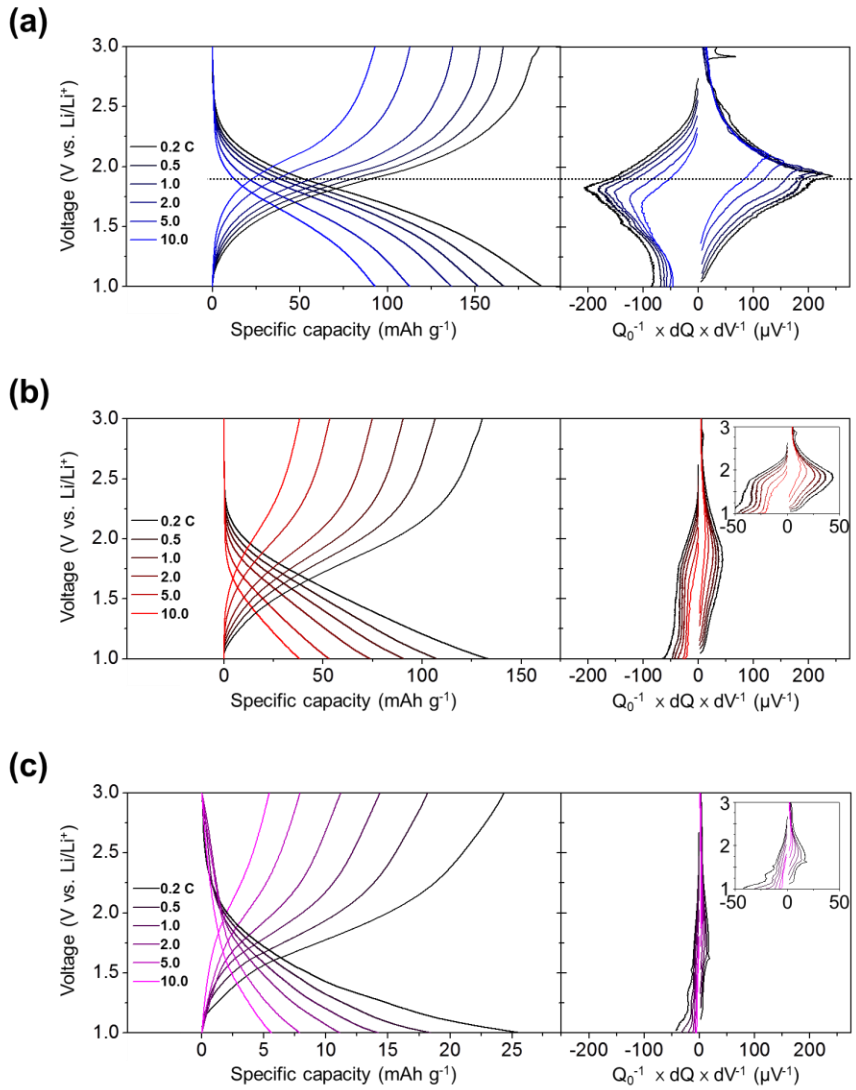

Figure 2-16. Galvanostatic charge/discharge voltage profiles and corresponding differential capacities for (a) 3D-TS, (b) nano-TiO_2, and (c) pc-TiO_2 at various C-rates (0.2C ~ 10C).

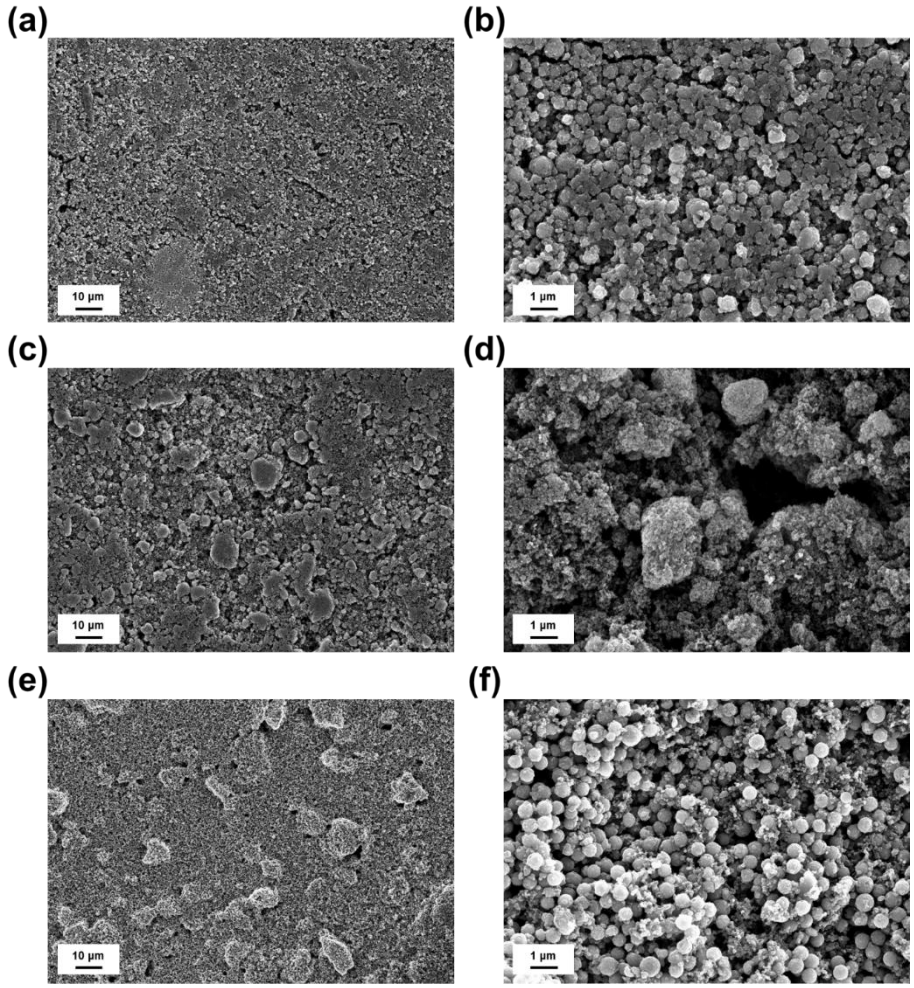

Figure 2-17. SEM images of electrodes after 200 cycles; (a, b) 3D-TS, (c, d) nano-TiO_2, and (e, f) pc-TiO_2.

Table 2-4. Fitting parameters used to simulate the EIS data.

Parameter		Active material		
	Unit	3D-TS	nano-TiO_2	pc-TiO_2
R_e	Ω	4.76	3.74	3.67
R_{ct}	Ω	41.2	261	238
R_{ic}	Ω	39.3	354	305
A_W[a)]	mΩ $s^{-0.5}$	0.037	0.387	1.01

[a)] $A_W = \frac{RT}{An^2F^2\theta C\sqrt{2D}}$

where R is the gas constant, T is the temperature, A is the diffusion area, n is the valency, F is the Faraday constant, C is the concentration of Li^+, D is the diffusion coefficient of Li in electrode and θ denotes the fraction of the reduced and oxidized species present.

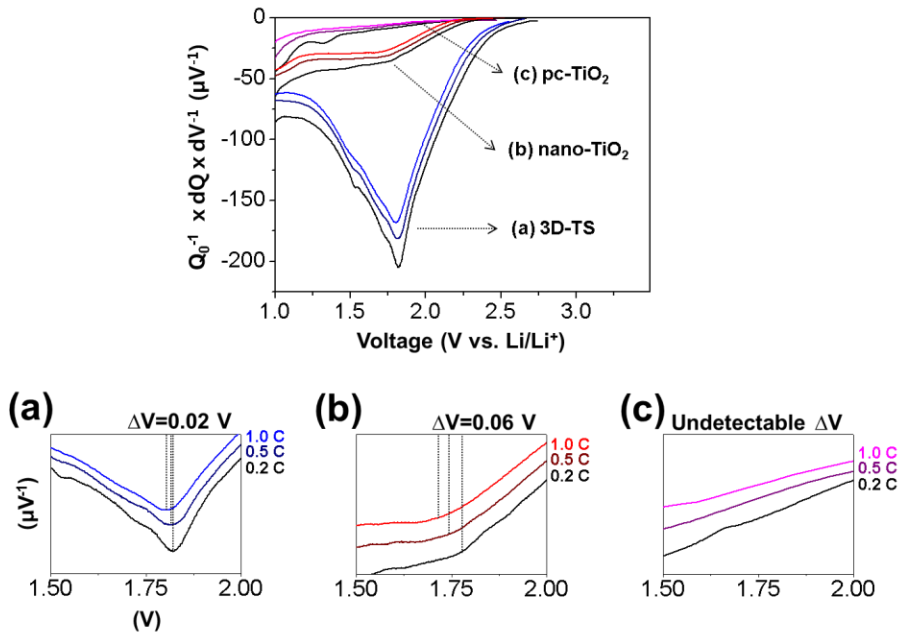

Figure 2-18. Differential capacities (obtained from galvanostatic charge voltage profiles at 0.2, 0.5, and 1.0 C) of (a) 3D-TS, (b) nano-TiO_2, and (c) pc-TiO_2.

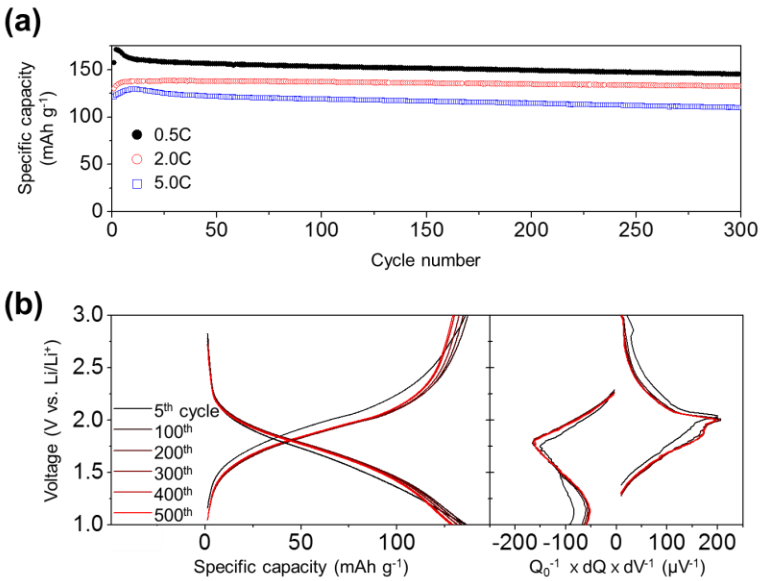

Figure 2-19. (a) Discharge capacities of the 3D-TS at 0.5, 2.0, and 5.0C during galvanostatic cycles. (b) The evolution of voltage profiles and corresponding differential capacities of the 3D-TS during long cycles test at 2.0C.

Chapter 3. Nanostructured $H_2Ti_{12}O_{25}$ as a Superior High Voltage Anode Materials for Li-Ion Batteries

3.1 Experimental

3.1.1 Synthesis of $H_2Ti_{12}O_{25}$ materials

$H_2Ti_{12}O_{25}$ samples were sequentially synthesized by the recrystallization of TiO_2 to $Na_2Ti_3O_7$, Na^+/H^+ ion exchange, and dehydration/condensation reaction upon heat treatment, according to a previous report [49]. First, $Na_2Ti_3O_7$ samples were prepared via a solid-state heat treatment using three types of TiO_2 nanoparticles with anatase (COTIOX KA-100, Cosmo Chemical), rutile (Titanium (IV) oxide, rutile, Aldrich), and anatase/rutile mixed phases (Aeroxide TiO_2 P 25, Evonik). Sodium carbonate (≥99.0%, Sigma-Aldrich) and TiO_2 particles were mixed in 1:3 molar ratio (0.53 g of Na_2CO_3 + 1.2 g of TiO_2). The finely ground mixture was heat-treated in air at 800 °C for 20 h. After cooling to room temperature, the sample was ground and heat-treated again under the same conditions. For the Na^+/H^+ ion exchange, the 0.75 g of resultant $Na_2Ti_3O_7$ was then placed in 200 ml of 1.0 M HCl with deionized water and stirring at 60 °C for 5 days. The reaction mixture was centrifuged and washed with water and ethanol two times. The product was dried at 70 °C to

obtain the $H_2Ti_3O_7$. The final $H_2Ti_{12}O_{25}$ was obtained after heat treating the $H_2Ti_3O_7$ at 260 °C for 5 h in air. The commercially available $Li_4Ti_5O_{12}$ (Samwha Capacitor Co., Ltd) were used as a control samples which were synthesized using a conventional solid-state reaction of TiO_2 and Li_2CO_3.

3.1.2 Characterizations

The morphologies of the samples were examined by transmission electron microscopy (TEM, JEOL, JEM-3010) and scanning electron microscopy (SEM, Carl Zeiss, SUPRA 55VP). An X-ray diffractometer (XRD, Rigaku, D/max-2200) was utilized to investigate crystalline structure of the samples.

3.1.3 Electrochemical measurements

Electrochemical experiments were performed using a conventional coin cell (CR2032) assembled in an Ar-filled glove box. A lithium foil and microporous polypropylenes were used as the counter electrode and separator, respectively. The working electrodes were fabricated using 80% w/w of the $H_2Ti_{12}O_{25}$, 10% w/w conductive carbon (Super P) and 10 % w/w poly(vinylidene difluoride) binder. The mixture was blended with a few drops of N-methyl-2-pyrrolidone (NMP, Sigma-Aldrich) to produce a grey-colored slurry. The slurries were cast on metal (Al or Cu) foils by doctor blading and the resulting film was vacuum-dried at 120 °C for 12 h. After roller compression, film-type electrodes are cut into a round disc with geometric area of 1 cm^2. The loading amounts of the

active materials were 1.4~1.5 mg cm^{-2}. A 1.15 M $LiPF_6$ solution of dissolved in 2:4:4 (v/v/v) ethylene carbonate/ethyl-methyl carbonate/dimethyl carbonate were adopted as an electrolyte. Galvanostatic charge/discharge analyses were performed with an automatic battery cycler (WBCS3000, WonaTech) at ambient temperature (30 ^{o}C). Electrochemical impedance spectroscopy and cyclic voltammetry were conducted using a computer-controlled potentiostat (ZIVE SP2, WonaTech). EIS data were obtained at E=1.58 V after 30 charge/discharge cycles. The frequency range was 100 mHz ~ 100 kHz under AC stimulus with a 5 mV amplitude. The parameters of the equivalent circuit were calculated by using the ZMAN software.

3.1.4 Computational details

Periodic density functional theory (DFT) calculations were carried out using the Vienna *ab initio* simulation package (VASP) [133]. The generalized gradient approximation (GGA) parameterized by Perdew-Burke-Ernzerhof (PBE) exchange-correlation functional was employed [134]. Ionic cores were described by the projector augmented wave (PAW) method [135]. The wave functions were constructed from the expansion of planewaves with an energy cut-off 520 eV. A 3 x 3 x 3 Monkhorst-Pack k-point mesh was used to sample the Brillioun zone. All calculations were converged until the forces on all atoms were less than 0.05 eV $Å^{-1}$. The electronic optimization steps were converged self-consistently to $<10^{-6}$ eV. DFT+U within Dudarev's approach was used with U_{eff}=4.2 to account for the on-site Coulomb interaction in the localized d

orbital [136]. This U value was obtained by fitting to experimental data the splitting between occupied and unoccupied Ti d states for oxygen vacancy states at the (110) surface of the TiO_2 [137], and has been used to model oxygen vacancies at other TiO_2 surfaces [138], Nb and Ta substitution [139], and oxygen vacancy and Ti interstitial formation in TiO_2 [140]. The transition state was located using the climbing image-nudged elastic band (CI-NEB) method [141, 142]. Nine spaced images were obtained by linear interpolation and used as initial trajectories for migration path. In the CI-NEB calculations, the images were refined until the maximum atomic forces are converged within 0.1 eV $Å^{-1}$.

3.2 Results and discussion

3.2.1 Structural evolution during synthesis of the HTO

In order to synthesize HTO, $Na_2Ti_3O_7$ as a parent crystal was first prepared by a solid state reaction between TiO_2 and Na_2CO_3 at 800 °C [49]. TiO_2 materials containing anatase or rutile phases can be adopted as starting materials. In this work, three types of TiO_2 with different crystalline structures were utilized: pure anatase, pure rutile, and an anatase/rutile-mixed phase. The crystal structure of the starting TiO_2 is highly important and determines the shape and size of the HTO products as discussed below. The produced $Na_2Ti_3O_7$ crystals can be efficiently converted to $H_2Ti_3O_7$ by an ion exchange step between Na^+ and H^+ [167, 168]. $H_2Ti_3O_7$ with a layered structure is rearranged to form final

HTO crystals during thermally induced dehydration and condensation reactions [169]. The evolution of crystal structure is displayed in Figure 3-1 and detailed synthetic methods are presented in the experimental section.

3.2.2 Characterizations of HTO made from phase-pure TiO_2

Figure 3-2 shows characterization and electrochemical data for two kinds of HTO materials synthesized from pure anatase or rutile TiO_2. X-ray diffraction (XRD) patterns of both HTO crystals are in agreement with the previously reported pattern (Figure 3-2(a)), which indicates that the HTO particles with a high crystallinity were successfully synthesized [49, 50]. Transmission electron microscopy (TEM) images and the scanning electron microscopy (SEM) image in Figure 3-2(b-d) reveal that both HTO particles are identical rod-shaped and micrometer-sized particles having transversal lengths of about 0.4 μm and longitudinal lengths of 1~10 μm.

Galvanostatic charge/discharge measurements of the HTO were performed between 1.0 and 3.0 V (*vs.* Li/Li^+) at various rates from 10 mA g^{-1} to 1000 mA g^{-1}. The electrode composed of HTO prepared from pure rutile TiO_2 was stably charged and discharged with 95~99% Coulombic efficiency, and an apparent voltage plateau were consistently observed (Figure 3-2(e)). The electrode delivers a reversible capacity of 192, 177, 161, 140, 113, 95, 78 mAh g^{-1} at a current density of 10, 25, 50, 100, 250, 500, 1000 mA g^{-1}, respectively. In corresponding differential capacities (Figure 3-2(f)), there are two voltage plateau regions center at 1.50 V and 1.58 V (*vs.* Li/Li^+). The two separated

voltage plateaus imply that there are two types of Li insertion sites and subsequent phase transformation [170]. The HTO showed a capacity retention of 74% during 150 charge/discharge measurements. The predictable reason for the capacity fading during the repetitive cycles is that irreversibly inserted Li obstructs further lithiation at confined areas of HTO crystals. The HTO material derived from anatase TiO_2 likewise exhibited an equivalent Li storage performance (Figure 3-3)

The decrease in reversible capacity at higher current density and the degraded performance that occurs during the repeated charge/discharge cycles can be explained by the limited Li diffusivity inside the bulky HTO crystal. To accurately explain the electrochemical properties of HTO in relation to the Li diffusion characteristics, before that, it is necessary to quantitatively identify the diffusion properties of Li and verify the existence of a close dependence between Li storage performance and diffusivity inside HTO crystal.

3.2.3 Diffusion properties of Li inside HTO

In order to theoretically determine the diffusivity of Li within the HTO crystal, it is necessary to construct a representative atomic crystal model. A monoclinic $Na_2Ti_{12}O_{25}$ crystal model with a *P12/ma* space group (ICSD ID: 28339) was utilized for the construction of the $H_2Ti_{12}O_{25}$ crystal model, because structural data for HTO have not been reported in previous studies. After replacing Na of $Na_2Ti_{12}O_{25}$ model with H, DFT calculations were proceeded to optimize the HTO crystal structure. The optimized structure and coordinates

are presented in Figure 3-4. Inside HTO crystal, the hydrogen atoms adsorbed on adjacent oxygens, forms O-H bond with the length of 98.4 pm.

There are four feasible pathways for the migration of Li inside the crystal: Two paths along the a-axis and two paths along the c-axis (Figure 3-5). The evolution of energetics for each path was determined, and the energy barriers to Li migration were extracted using DFT calculations using the climbing image-nudged elastic band (CI-NEB) method. Figure 3-6 shows the relative energies as a function of the movement of Li along the straight line projected between the two sites for each path. The calculated energy barrier for the path B and D are 0.157 and 0.271 eV, respectively. The values of the energy barrier for the Li migration through path A and C are 2.7~6.7 times higher than those for paths B and D. Therefore, there are severe anisotropy of Li diffusion processes inside HTO, which indicates that the majority of Li diffusion occurs *via* penetrating tetragonal channels (path B and D) in parallel with the c-axis.

The diffusion constant can be estimated using the Einstein-Smoluchowski relation as follows [55, 171].

$$\mathrm{D} = \mathrm{g}\Gamma d^2$$

where g($\cong$1) is a geometric factor, $\Gamma(= v^* exp - E_{act}/(k_B T))$ is a hopping frequency between sites ($v^* \cong 10^{13}$ Hz) and d is the migration distance. The values of D for path B and D are approximated to be 10^{-7}~10^{-4} ($cm^2\ s^{-1}$) at a temperature of 305 K. Comparing with D for the commercially available graphite (10^{-7}~10^{-6} $cm^2\ s^{-1}$) [172], path B and D provide an efficient route for

the diffusion of intercalated Li. Table 3-1 shows detailed information on the determined diffusion characteristics.

3.2.4 Effect of operating temperature on Li storage performance

The effect of operating temperature was investigated to verify the dependence of Li storage performance on the diffusivity of Li. Figure 3-7(a) displays the evolution of discharge capacities which was monitored at various operating temperatures ranging from 287 K to 315 K. A large difference in capacity of 63 mAh g^{-1} occurs when the operating temperature is elevated from 287 K to 315 K. At the same time, the diffusion constants change in the range of 1.5×10^{-5}~2.6×10^{-5} (cm^2 s^{-1}), which was determined based on the results of DFT calculations regarding Li migration through path B. In the case of another feasible diffusion path D, the diffusion constants are in the range of 2.7×10^{-7}~7.2×10^{-7} (cm^2 s^{-1}) (Figure 3-8). In principle, the diffusion of Li is accelerated by increasing the ambient temperature as described by Arrhenius equation. Therefore, if the insertion/extraction of Li in HTO are diffusion-controlled reactions, then the Li storage behavior of HTO should change significantly in response to variations in the temperature. Consequently, the proportional relationship between the diffusion constant and capacity verifies that the electrochemical performance of HTO materials depend upon the kinetics of Li migration inside the crystal structure. It is well-known that the electrochemical performance of LTO is mainly limited by its intrinsically low electronic conductivity [173]. A comparison between the capacities of LTO and HTO in

response to temperature change can also provide evidence for the diffusion-controlled Li insertion/extraction process of HTO (Figure 3-9).

Due to the effect of temperature, not only decreased capacity but larger polarization are observed at lower ambient temperatures (Figure 3-10). This is because the diffusion of Li become sluggish. Importantly, the poor diffusion in the HTO obstructs Li from moving toward the thermodynamically favorable intercalation sites, which results in an increase in internal resistance and the blockage of further lithiations. A comparison of cyclic voltammetry (CV) curves in Figure 3-7(b) clearly shows that the polarization range of potential (denoted in Figure 3-7(b)) is remarkably larger when the HTO electrode is charge/discharged at low temperature.

As mentioned above, Li diffuses into HTO in a highly anisotropic manner *via* kinds of one-dimensional channels (path B and D) developed in parallel with the c-axis. Also, between path B and D, Li diffusivity is higher in path B. As presented Figure 3-7(b), the voltage plateau at 1.5 V is substantially attenuated at low temperature of 287 K, while the plateau with a center at 1.58 V is relatively well preserved. The reason for this result lies in the kinetic discrepancy of Li diffusion along path B and D. The relatively sluggish Li mobility makes it difficult to access Li insertion sites through path D. Therefore, it can be concluded that the voltage plateaus at 1.5 V and 1.58 V indicate Li insertion through path D and B, respectively.

3.2.5 Kinetic gap of structural transformation from TiO_2 to $Na_2Ti_3O_7$

The understanding of Li dynamics and their effect on the Li storage performance drove us to develop a nanostructured HTO. The time constant t for Li diffusion ($t = L^2/D$) is an important factor that is responsible for the limited power or rate capability of an electrode material. Thus, in attempts to reduce the Li transfer length (L) and minimize resistive behavior, a nanostructured HTO with the shape of a nano-bundle was synthesized in this study.

In order to synthesize a HTO nano-bundle comprised of HTO nanorods, the initial synthetic step from TiO_2 to $Na_2Ti_3O_7$ during the solid-state HTO synthesis should be noted. This recrystallization of TiO_2 to produce $Na_2Ti_3O_7$ is especially worth noting because it involves drastic structural changes in the atomic and nanoscale (Figure 3-11). Among the reaction parameters, the crystalline phases of the reactants are highly important because the TiO_2 particles with different crystal structures and phase stabilities are likely to cause different reaction rates and pathways. If the TiO_2 particles containing both anatase and rutile phases are utilized for the synthesis of $Na_2Ti_3O_7$, the differences in the rate, namely a "kinetic gap" of structural transformation can be induced by virtue of varied thermal stabilities. It is well known that rutile shows higher phase stabilities than anatase at all temperatures [174, 175].

To identify the kinetic gap during the structural transformation from TiO_2 to $Na_2Ti_3O_6$, time-resolved XRD measurements were conducted for both anatase and rutile TiO_2. Identical to the synthetic condition of $Na_2Ti_3O_7$, a mixture of TiO_2 (anatase or rutile) and Na_2CO_3 powders was heat-treated (24h×2 at 800 ^oC) in air for XRD measurements. Figure 3-12(a) and (c) display the evolution

of the XRD pattern and corresponding peak area as a function of time when pure anatase TiO_2 particles were used as a starting material. Figure 5(b) and (d) are the same as above except that the pure rutile TiO_2 particles were used. Before the temperature rising, the XRD patterns for anatase (JCPDS No. 01-0562) or rutile (JCPDS No. 02-0494)-phased TiO_2 both match exactly with references. The overall structural transformation consists of a multi-step reaction of $TiO_2 \rightarrow Na_2Ti_6O_{13}$ (JCPDS No. 14-0277)$\rightarrow Na_2Ti_3O_7$ (JCPDS No. 14-0085) which can be described as follow:

$$6TiO_2 + Na_2CO_3 \rightarrow Na_2Ti_6O_{13} + CO_2$$

$$Na_2Ti_6O_{13} + Na_2CO_3 \rightarrow 2Na_2Ti_3O_7 + CO_2$$

where the $Na_2Ti_6O_{13}$ is a transient species within this multi-step reaction.

A comparison of the phase evolution of the material indicates that there is a kinetic gap in the structural transformations between anatase and rutile TiO_2 (Figure 3-12(c) and (d)). Upon heat treatment, the anatase TiO_2, which has a relatively lower thermal stability, is first converted to rutile TiO_2 within 2 h, and the peaks for the $Na_2Ti_6O_{13}$ intermediate then begin to appear. After 7 h of reaction, the contents of $Na_2Ti_6O_{13}$ gradually decrease to form $Na_2Ti_3O_7$. In this situation, the rutile TiO_2 derived from anatase completely disappears after a 10 h reaction time. On the other hand, the rutile form of TiO_2 instantly participates in the reaction to form $Na_2Ti_6O_{13}$. Most of the TiO_2 species disappears within 5 h, and the $Na_2Ti_6O_{13}$ also starts to disappear after 3 h. Based on the fact that the TiO_2 species is completely consumed, there is the time lag of 7 h between

anatase and rutile TiO_2, which generates the kinetic gap associated with the structural transformation (Figure 5(e)).

3.2.6 Synthesis and Li storage performance of nanostructured HTO

As it turns out, the presence of a kinetic gap during the structural transformation was applied to create the nanostructured HTO. First, TiO_2 particles with anatase/rutile mixed phases are utilized for the synthesis of HTO. It is well known that Aeroxide P 25 TiO_2 particles made by Evonik (referred to as P 25) is composed of mixtures of anatase and rutile crystallites, the reported ratio typically being about 70:30 [176]. The coexistence of anatase and rutile phases and the difference in the speed of structural transformation segregate the locations where the reaction occurs. As shown in Figure 3-13(a), the rutile phase constituting P 25 reacts rapidly with Na_2CO_3 to generate sodium titanate compounds ($Na_2Ti_6O_{13}$ and subsequent $Na_2Ti_3O_7$) in the shape of nanorods. Concurrently, the anatase phases promote the preferential transformation into rutile phases. The rutile phases originating from anatase parts then react with Na_2CO_3 later, which was already under way for the intrinsic rutile one. As a result, nano-bundle shaped nanostructured HTO can be obtained. No noticeable nano- structural changes were observed in the following dehydration ($4H_2Ti_3O_7 \rightarrow H_2Ti_{12}O_{25} + 3H_2O$) upon heating at 260 °C (Figure 3-14). Because the HTO is produced using mixed crystallites of TiO_2, hereafter referred to as mc-HTO.

Figure 3-13(b) and (c) show the TEM images of mc-HTO with a bundle-structure containing HTO nanorods. Each single nanorod has a diameter of 3~4

nm, and the entire mc-HTO bundle has a diameter of 50~100 nm and a length of 250~350 nm, as confirmed by the SEM image in Figure 3-13(d). Energy dispersive spectrometry (EDS) element mapping results (Figure 3-13(e)) proves that the mc-HTO is mainly composed elemental Ti and O and that impurities such as elemental Na, C are essentially absent.

As discussed above, our main object was to produce mc-HTO with a reduced resistive behavior stemming from the sluggish Li diffusion inside HTO crystal. Figure 3-15(a) shows the discharge capacities of the mc-HTO cycled at various current densities (10~1000 mA g^{-1}). The electrode composed of mc-HTO stably delivers a reversible capacity of 230, 216, 206, 195, 175, 158, 138 mAh g^{-1} with a nearly 100% Coulombic efficiency at a current density of 10, 25, 50, 100, 250, 500, 1000 mA g^{-1}, respectively (Figure 3-16). The rate capability of the mc-HTO is significantly better than the values for bulky HTOs made from pure crystalline TiO_2. The HTOs made from pure crystalline TiO_2 exhibited almost the same characteristics, therefore, they are referred to hereafter as pc-HTO. These findings demonstrate the existence of fast and efficient Li insertion/extraction, aided by a short diffusion length/time. In addition, the mc-TiO_2 showed a long cyclic stability without any significant capacity fading (Figure 3-17).

The highly conductive state signifies that the electrochemical characteristics of mc-HTO represent the thermodynamic properties of the materials. Therefore, the detailed mechanistic information on the Li insertion/extraction process can be confirmed *via* electrochemical analyses. The data in Figure 3-15(b) shows the charge/discharge voltage profile at the first cycle. During the first lithiation

(charging) process, mc-HTO accepts about 10.7 Li equiv.$^{-1}$ which correspond to a specific capacity of 295 mAh g^{-1}. And about 8.6 Li equiv.$^{-1}$ (236 mAh g^{-1}) are released in subsequent delithiations (discharge). It should be noted that about 2 Li equiv.$^{-1}$ are irreversibly inserted inside the HTO crystal. This phenomenon can be explained by the fact that the 2 Li^+ ions substitute pre-existing H^+ ions of HTO. Before the insertion of Li, the H^+ ions maintain the charge balance of the HTO crystal in which Ti atoms show Ti^{4+} states. The incorporation of Li during the first lithiation induces switching from H^+ to Li^+, which explains the exceptionally high specific capacity of HTO (or $Li_2Ti_{12}O_{25}$). After the first lithiation, the capacity corresponding to 2 Li equiv.$^{-1}$ is not recovered, consequently, 8.7 Li equiv.$^{-1}$ is reversibly inserted/extracted ($Li_2Ti_{12}O_{25} \leftrightarrow Li_{10.7}Ti_{12}O_{25}$).

Electrochemical impedance spectroscopy (EIS) analyses were performed to quantitatively determine the difference in electron/mass transfer resistance of the mc-HTO and pc-HTO. Figure 3-15(c) and (d) show Nyquist plots obtained after 30 charge/discharge cycles and an equivalent circuit model for the fitting of the EIS results, respectively [166, 177]. Based on the fitting results, each kinetic parameter was determined from the experimental data (Table 3-2). Among the kinetic parameters R_e corresponds to an equivalent series resistance and *CPEs* are constant-phase elements. Z_w is the Warburg element related to the diffusion of Li inside the crystal. Since the Warburg coefficient (A_W), which is directly converted to the diffusion coefficient, is an intrinsic property of HTO crystals, the value of A_W for both mc-HTO and pc-HTO are in a similar range. The values of R_{ct}, electrolyte/HTO charge transfer resistance, of mc-HTO (32.7

Ω) is smaller than that of pc-HTO (48.1 Ω), which confirms the superior mass conductance inside the mc-HTO electrode material. Interestingly, the value of R_{ic}, intercrystaliite transfer resistance, corresponding to mc-HTO (1.58 Ω) is significantly smaller than that of pc-HTO (9.23 Ω). This result indicates that the unique nanostructure of mc-HTO not only improves the kinetics of Li diffusion, but also assures a low electronic contact resistance between individual HTO particles, because a closely packed bundle of HTO nanorods facilitates the delivery of electrons across primary crystallites. Consequently, based on the EIS data, the bundled structure of mc-HTO relieves the resistive behavior, which explains the superior rate capability of the material.

Another noteworthy fact is that the mc-HTO delivered much higher discharge capacities at all current densities when compared to a commercial LTO sample which delivered 132 mAh g^{-1} of specific capacity at 10 mA g^{-1} and 74 mAh g^{-1} at 1000 mA g^{-1} (Figure 3-15(a)). This suggests that the mc-HTO represents a superior high voltage anode material which has the potential to substitute LTO material. Furthermore, such mc-HTO materials have many practical advantages for industrial production in terms of cost-effectiveness, ease of manufacturing, and scalability.

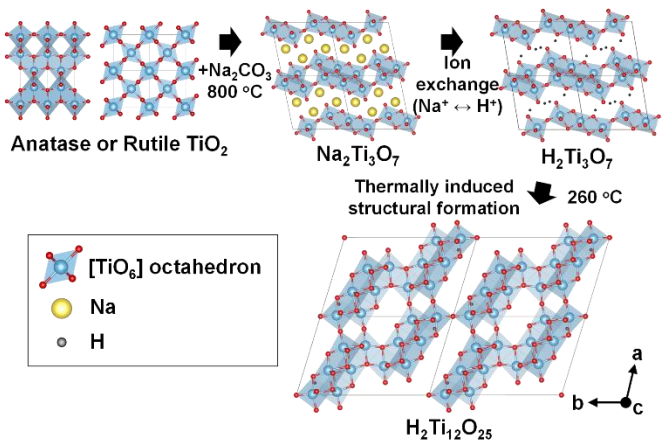

Figure 3-1. Synthesis of HTO crystals via a sequential process of recrystallization of TiO_2, ion exchange, and thermally induced dehydration/structural formation. Hexahedrons represents the boundary of a primitive unit cell.

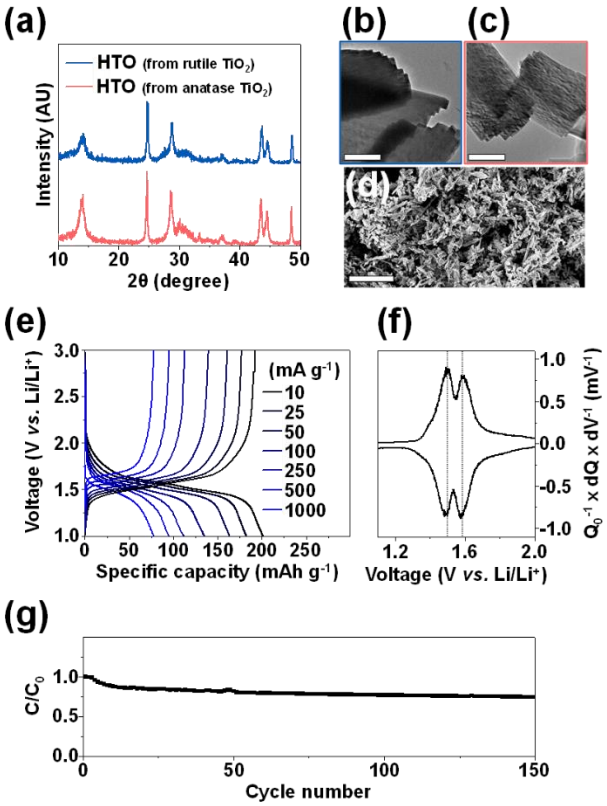

Figure 3-2. XRD patterns (a) and TEM images of prepared HTO crystal synthesized using pure rutile (b) and anatase (c) TiO_2 as starting materials. Scale bars correspond to 0.2 μm. (d) SEM image of a synthesized HTO crystal. Scale bar corresponds to 10 μm. (e) Galvanostatic charge/discharge voltage profiles of HTO made from rutile TiO_2 at various current densities from 10 mA g^{-1} to 1000 mA g^{-1}. (f) Corresponding differential capacities obtained at 10 mA g^{-1}. (g) Relative discharge capacities of the HTO at 100 mA g^{-1} during the galvanostatic charge/discharge cycles. C_0 is the discharge capacity from the first cycle.

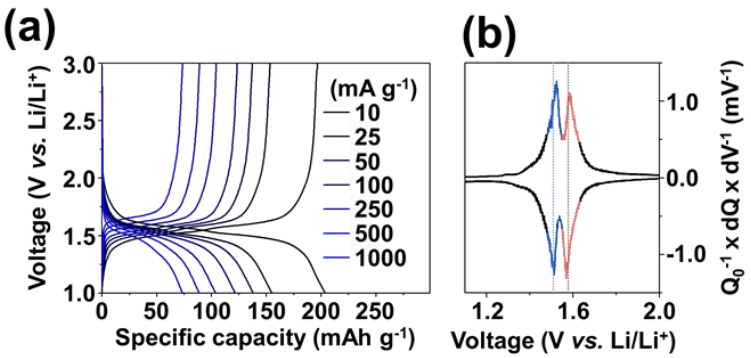

Figure 3-3. (a) Galvanostatic charge/discharge voltage profiles of HTO made from anatase TiO_2 at various current densities from 10 mA g^{-1} to 1000 mA g^{-1}. (f) Corresponding differential capacities at 10 mA g^{-1}.

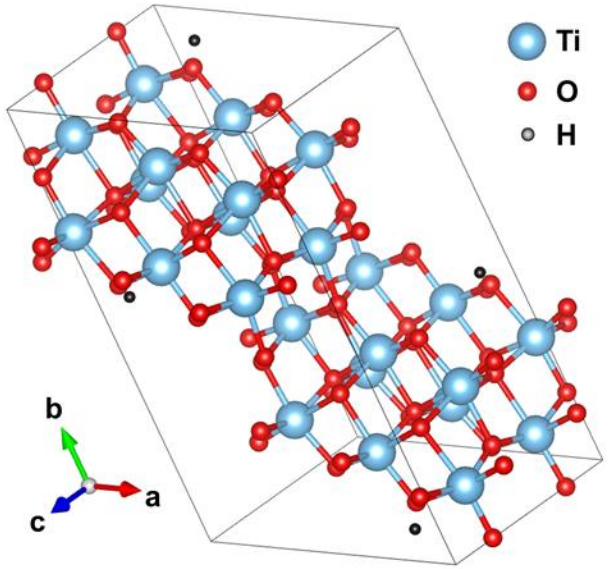

Figure 3-4. DFT-optimized crystal structure of $H_4Ti_{24}O_{50}$. Hexahedron represents the boundary of a primitive unit cell. The coordinates of this structure are presented below.

Coordinates of $H_4Ti_{24}O_{50}$

Unit cell (Å)

X	Y	Z
9.4775307667714586	-0.0907339953220821	-0.0050687142392930
-4.2311319016390598	14.2742692283106809	0.0013427561070414
-0.0055735329651447	-0.0025817149010813	7.7947458599171524

Atom	Cartesian coordinates		
	X	Y	Z
Ti	8.752673452	1.714004186	2.000160169
Ti	8.841069336	1.731665574	5.839629612
Ti	5.703452977	2.505454062	1.976972628
Ti	5.653498070	2.604665863	5.861759004
Ti	2.661355185	3.380330433	1.991120013
Ti	2.668621196	3.440557588	5.846370179
Ti	-3.740363928	12.498154468	1.955294140
Ti	-3.651969067	12.515813523	5.794763583
Ti	-0.552792659	11.625155345	1.933165329
Ti	-0.602748676	11.724362481	5.817952286
Ti	2.432084190	10.789262771	1.948556825
Ti	2.439350047	10.849486744	5.803807223
Ti	1.694422487	5.743501735	0.024538634
Ti	1.717368407	5.750441766	3.903423059
Ti	-2.810521754	10.203449579	7.768334101
Ti	-2.761153530	10.096517617	3.872819175
Ti	0.333999673	9.275942536	7.743668866
Ti	0.209213706	9.209569344	3.889083325
Ti	3.406282158	8.486317351	7.770389537
Ti	3.383337086	8.479377320	3.891504410
Ti	7.911226639	4.026369084	0.026591183
Ti	7.861858379	4.133301046	3.922106436
Ti	4.766705103	4.953876126	0.051258302

Ti	4.891491223	5.020249743	3.905843679
O	1.065944218	2.563339218	1.975780670
O	1.088258824	2.573800359	5.875949133
O	1.907503893	5.366039214	1.955630053
O	1.926416217	5.369771544	5.876095950
O	3.912773290	1.900855395	1.957109373
O	3.947410593	1.964857175	5.880897234
O	4.695406096	4.506336384	1.962374105
O	4.717035740	4.513028480	5.884227096
O	6.865588285	1.108993522	1.958591480
O	6.812322697	1.028093263	5.889224445
O	7.640722477	3.655012062	1.969925882
O	7.611263131	3.608266332	5.876672532
O	4.012447011	11.656018092	1.918974619
O	4.034759325	11.666480718	5.819143082
O	3.174287322	8.860048391	1.918830589
O	3.193202427	8.863779024	5.839296486
O	1.153295055	12.264962336	1.914028493
O	1.187930858	12.328963480	5.837816238
O	0.383669538	9.716793151	1.910699676
O	0.405297790	9.723480582	5.832552667
O	-1.711617107	13.201726462	1.905695474
O	-1.764883804	13.120824295	5.836328555
O	-2.510557074	10.621555300	1.918252614
O	-2.540018400	10.574804056	5.824999496

O	-3.549215455	12.005780462	7.777852573
O	-3.509141814	12.000482831	3.863479345
O	-1.514058236	8.498892538	7.723199991
O	-1.505771100	8.585676477	3.891174769
O	-0.095633397	5.146202727	0.005352714
O	-0.059273892	5.118564480	3.939219430
O	-0.762237266	11.047450097	7.776323076
O	-0.728675951	11.101931217	3.870522605
O	1.368148494	7.674915236	7.768184961
O	1.387966377	7.671697331	3.888465161
O	2.922765592	3.981580208	0.022602623
O	2.899697570	3.975760859	3.919272777
O	8.649920101	2.224038837	0.017072195
O	8.609846410	2.229336256	3.931446034
O	6.614762877	5.730926547	0.071731042
O	6.606476250	5.644143033	3.903754326
O	5.196337631	9.083616783	7.789574228
O	5.159978696	9.111255032	3.855703161
O	5.862942348	3.182369414	0.018602834
O	5.829381164	3.127887869	3.924403005
O	3.732556279	6.554903425	0.026744973
O	3.712739398	6.558121755	3.906463005
O	2.177939054	10.248238878	7.772324639
O	2.201007640	10.254058227	3.875655156
O	-4.350533925	14.229413787	1.988443857

O	9.451239303	0.000405010	5.806481056
H	6.840400855	6.434844015	0.711136052
H	-1.739694960	7.794974223	7.083790661
H	-1.422022179	14.141795579	1.911731227
H	6.522727061	0.088023748	5.883176148

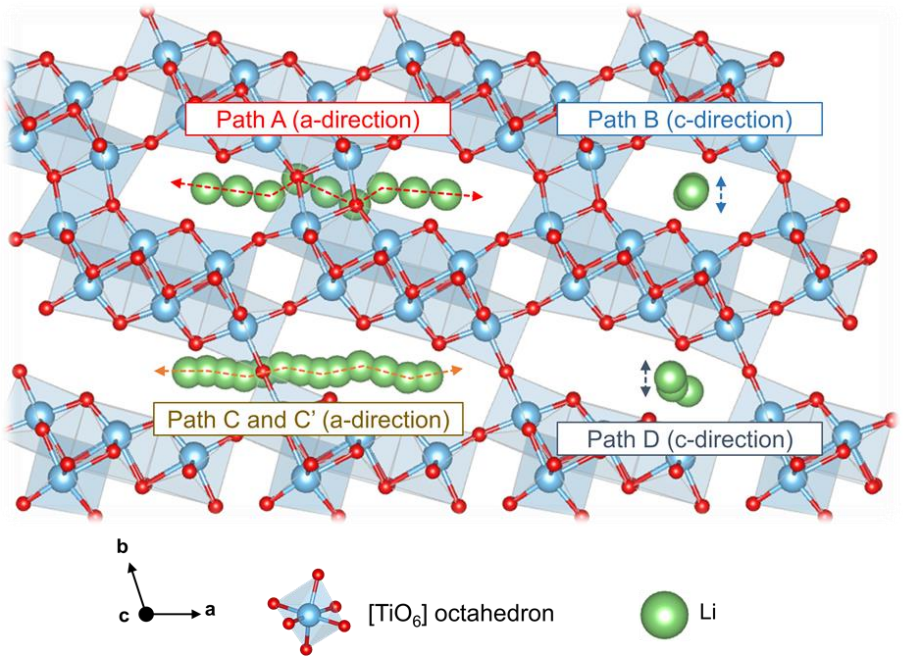

Figure 3-5. Atomic crystal structure of Li-incorporated $Ti_{12}O_{25}$ and possible pathways for Li migration inside the crystal. The path A and C represents Li migration in the a-direction, and the path B and C corresponds to the movement of Li in the c-direction.

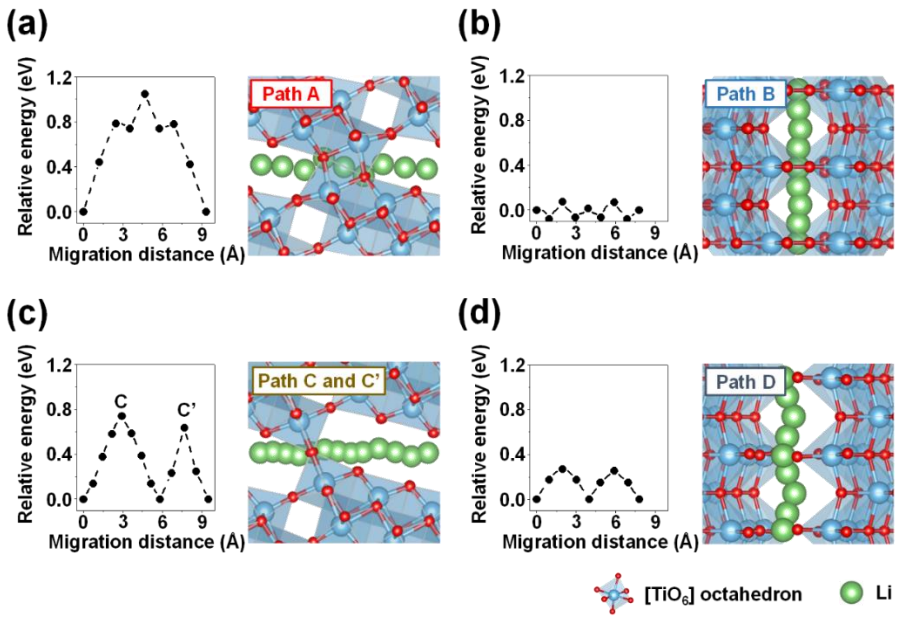

Figure 3-6. DFT-calculated relative energies along the different migration paths existing inside the HTO crystal and corresponding crystal structure of Li inserted HTO near each path. (a, c) Path A and C represents Li migration along a-direction. (b, d) Path B and D corresponds to the movement of Li through channels present in c-direction.

Table 3-1. Diffusion characteristics of Li inside the HTO crystal.

		Migration distance (d)	Energy barrier (E_{act})	Diffusivity at 305K[a)] (D)
		Å	eV	$cm^2\ s^{-1}$
Path A	a-direction	9.34	1.05	3.82×10^{-19}
Path B	c-direction	2.92	0.157	2.16×10^{-5}
Path C	a-direction	5.82	0.740	2.04×10^{-14}
Path C'	a-direction (inside pore)	3.68	0.637	4.05×10^{-13}
Path D	c-direction	3.98	0.271	5.22×10^{-7}

Note. In DFT calculations, a $Li_{0.5}Ti_{12}O_{25}$ crystal model was used to evaluate the energy barrier.

[a)]Diffusivity was calculated using the Einstein-Smoluchowski relation: $D = g\Gamma d^2$

where g($\cong 1$) is a geometric factor, Γ($= \nu^* \exp(-E_{act}/k_BT)$) is a hopping frequency between sites ($\nu^* \cong 10^{13}$) and d is migration distance.

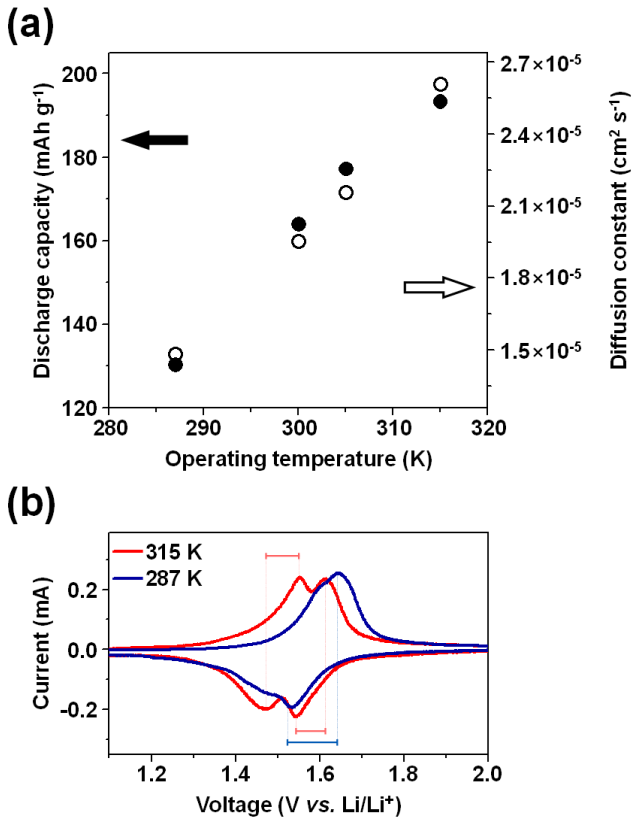

Figure 3-7. (a) Discharge capacities and diffusion constants of HTO as a function of operating temperature. The diffusion constants were determined using the results of the DFT calculations based on Li migration through path B which is identified as the most favorable Li pathway. (b) CV curves for the pc-HTO (measured at 0.05 mV s^{-1}) at operating temperatures of 287 K and 315 K.

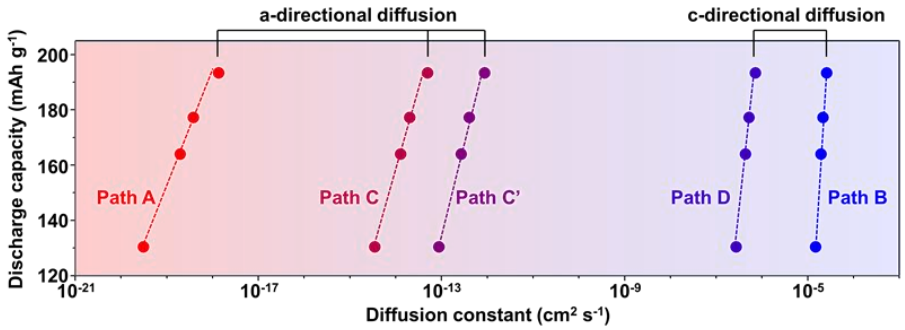

Figure 3-8. Discharge capacities of HTO and theoretically determined diffusion constants for four types of Li migration path existing inside HTO.

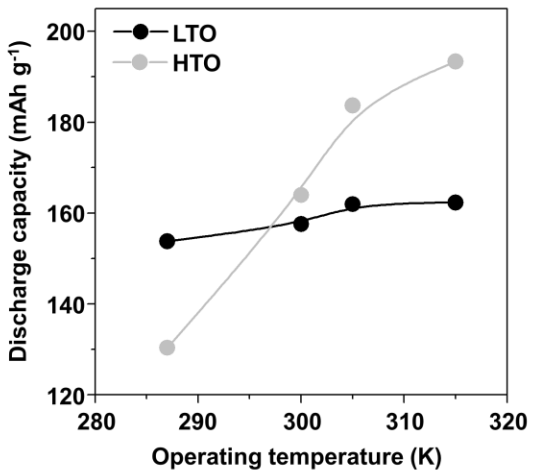

Figure 3-9. Discharge capacities at various operating temperature: Comparison between HTO (Li diffusion-controlled process) and LTO (electron conduction-controlled process).

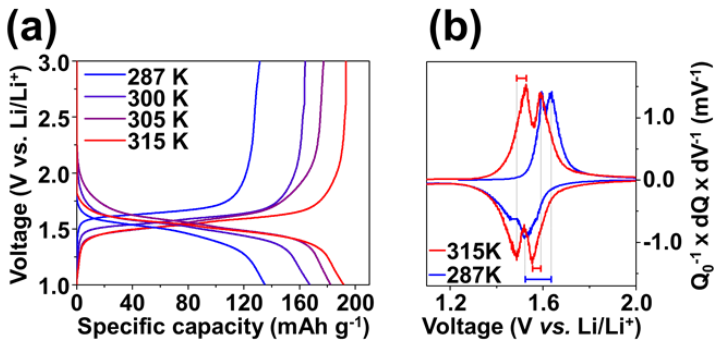

Figure 3-10. (a) Galvanostatic charge/discharge voltage profiles (measured at 10 mA g^{-1}) and (b) differential capacities of HTO at varied operating temperature.

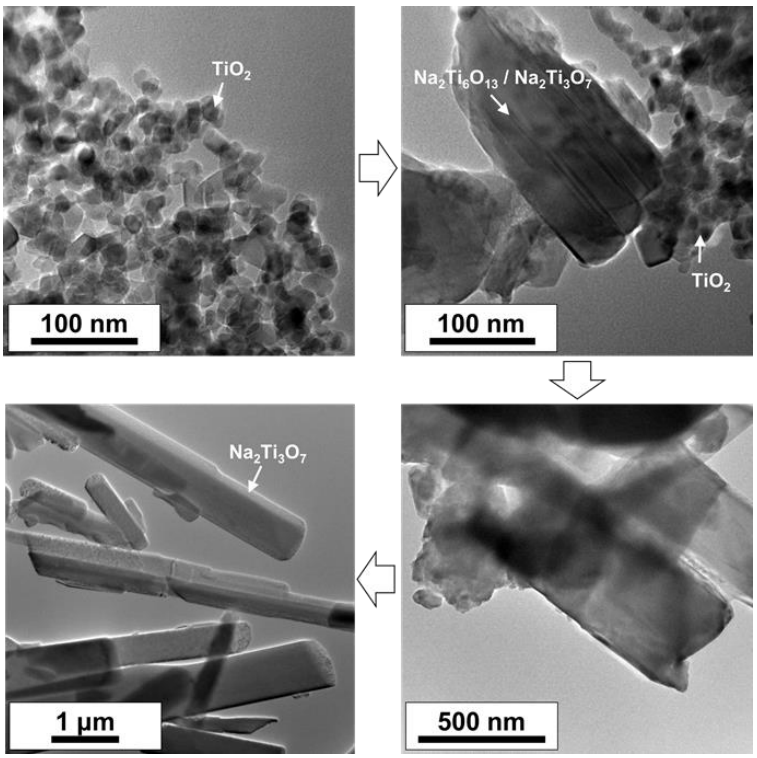

Figure 3-11. TEM images of samples obtained during the following conversion reaction: $TiO_2 + Na_2CO_3 \rightarrow Na_2Ti_3O_6$.

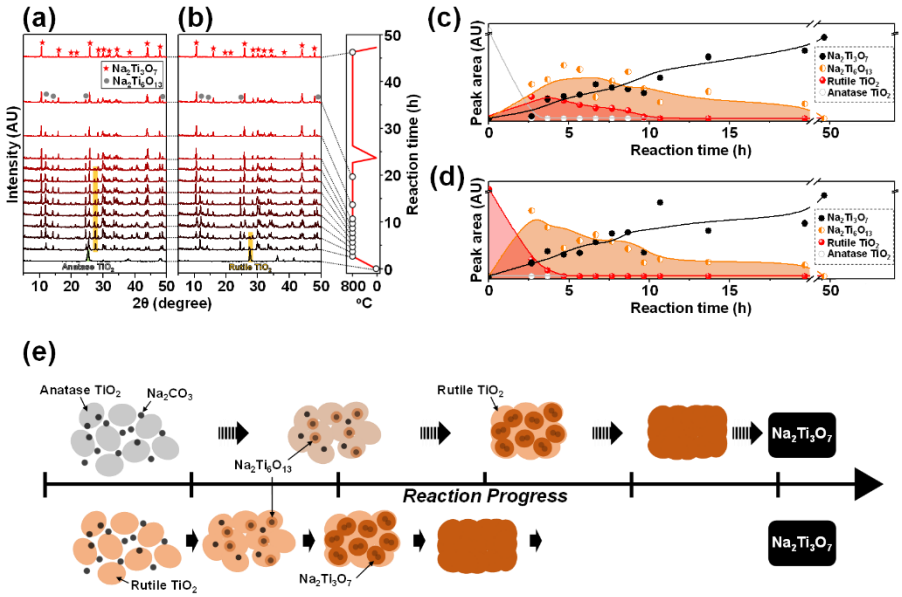

Figure 3-12. The evolution of XRD pattern during the phase transformation: (a) Anatase TiO_2 → $Na_2Ti_3O_7$ and (b) rutile TiO_2 → $Na_2Ti_3O_7$. (c, d) The XRD peak areas of reactants (anatase or rutile TiO_2), intermediate ($Na_2Ti_6O_{13}$), and product ($Na_2Ti_3O_7$) as a function of reaction time. The peak areas of anatase TiO_2, rutile TiO_2, $Na_2Ti_6O_{13}$, and $Na_2Ti_3O_7$ were obtained from major XRD peaks located at 25.28°, 27.51°, 11.84°, and 10.56°. (e) Schematic illustrations showing the kinetic gap during the TiO_2 → $Na_2Ti_3O_7$ phase transformations when anatase and rutile TiO_2 are adopted as starting materials, respectively.

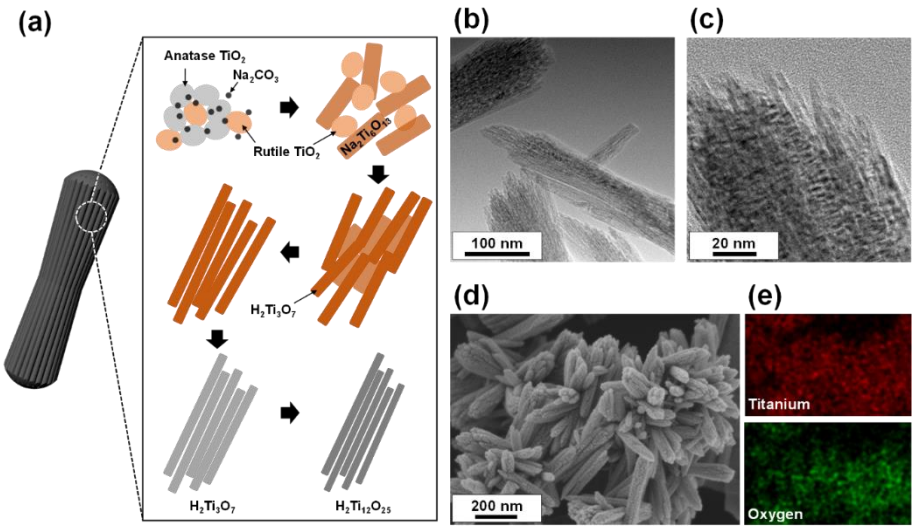

Figure 3-13. (a) Schematic illustrations showing the formation of mc-HTO driven by the kinetic gap of phase transformation between anatase and rutile TiO_2. (b, c) TEM images of mc-HTO crystals made from P 25 with anatase/rutile mixed phases. (d) SEM image of the mc-HTO and (e) EDS element mapping results.

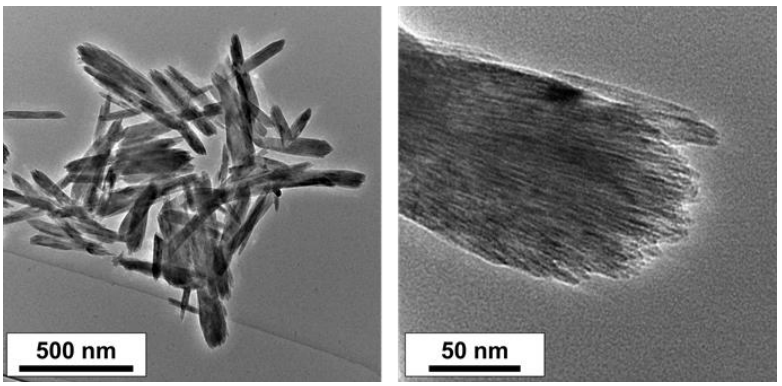

Figure 3-14. TEM images of nanostructured $H_2Ti_3O_7$ with the shape of a nano-bundle before thermally induced dehydration and condensation reactions at 260 ^oC.

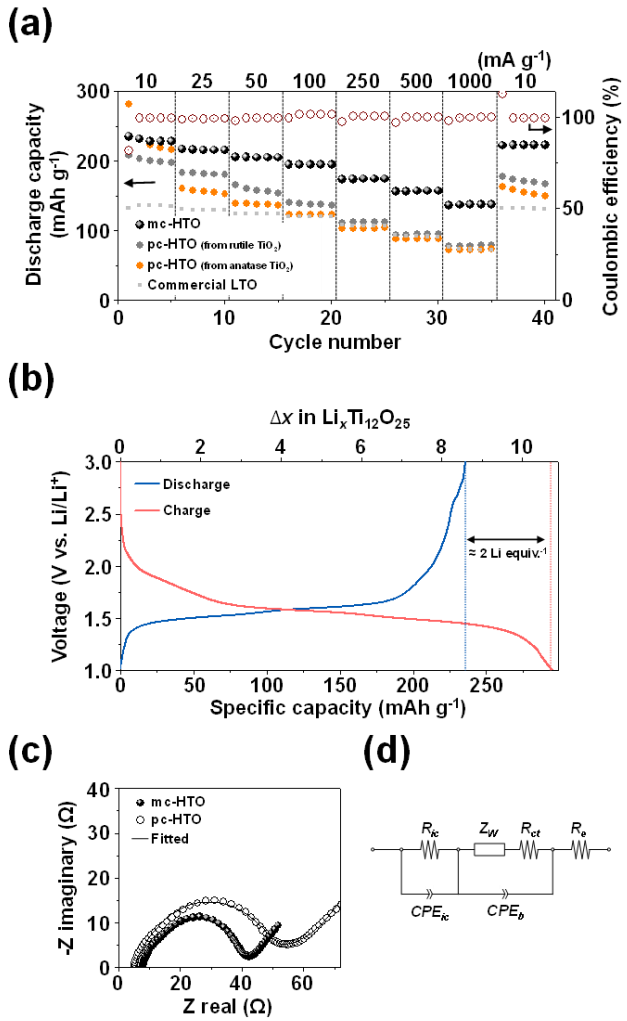

Figure 3-15. (a) Specific capacities of HTO electrodes and commercial LTO cycled at various current densities. Coulombic efficiencies of mc-HTO are denoted. (b) First charge/discharge voltage profile of mc-HTO at 10 mA g^{-1}. (c) Nyquist plots obtained from electrodes composed of mc-HTO and pc-HTO. (d) Equivalent circuit model for fitting.

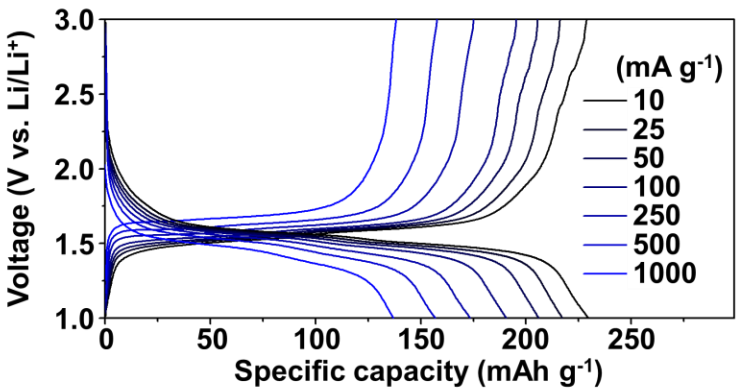

Figure 3-16. Galvanostatic charge/discharge voltage profiles of mc-HTO at various current densities from 10 mA g^{-1} to 1000 mA g^{-1}.

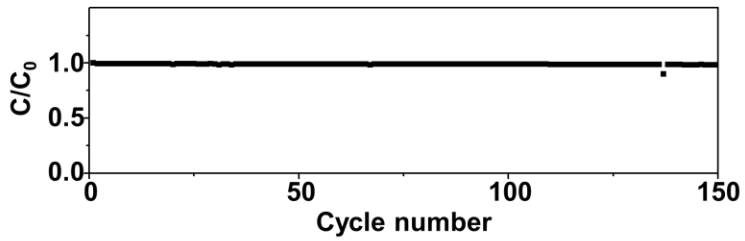

Figure 3-17. Relative discharge capacities of mc-HTO at 100 mA g^{-1} during the galvanostatic charge/discharge cycles. C_0 is the discharge capacity from the first cycle.

Table 3-2. Fitting parameters used to simulate the EIS data.

Parameter		Active material	
	Unit	mc-HTO	pc-HTO
R_e	Ω	7.51	4.98
R_{ct}	Ω	32.7	48.1
R_{ic}	Ω	1.58	9.23
A_W[a)]	mΩ $s^{-0.5}$	0.017	0.016

[a)] $A_W = \frac{RT}{An^2F^2\theta C\sqrt{2D}}$

where R is the gas constant, T is the temperature, A is the diffusion area, n is the valency, F is the Faraday constant, C is the concentration of Li^+, D is the diffusion coefficient of Li in electrode and θ denotes the fraction of the reduced and oxidized species present.

Chapter 4. 3D Bicontinuous Metal/Carbon Hybrid using an Agarose Gel for Ultra-Fast Charge/Dischargeable Supercapacitor Electrodes

4.1 Experimental

4.1.1 Fabrication of bicontinuous carbon and 3D Au composites

A 2 % (w/v) solution of agarose gel with dimensions of 1 cm × 2 cm × 0.5 cm was immersed in a 100 mM $HAuCl_4$ solution for 18 h at room temperature in sealed container. The gold precursors ($HAuCl_4$) inside the pores of the agarose gel were then completely reduced by treatment with an excess of sodium borohydride ($NaBH_4$), and washed with de-ionized water. The resulting gold/agarose gel composite was dried in a vacuum desiccator at room temperature before carbonization at 800℃ for 4h under Ar or NH_3 atmosphere.

4.1.2 Physicochemical characterizations

The surface morphology and composition of the Au/C composites were characterized using a scanning electron microscopy (SEM, Carl Zeiss, SUPRA 55VP). X-ray photoelectron spectroscopy (XPS, Karatos, AXIS-HSi), and X-ray diffractrometer (XRD, Rigaku, D/max-2200) were utilized to investigate the crystalline and elemental structure of composite. Bright-field TEM image

was collected by high-resolution TEM (HR-TEM, JEOL, JEM-3010).

4.1.3 Electrochemical characterizations

Electrochemical tests were performed using a standard three-electrode system (Iviumstat electrochemical analyzer, Ivium Technology) with a saturated Ag/AgCl as a reference electrode and platinum counter electrode. The working electrodes were prepared by coating the carbon materials (3DMC, activated carbon, graphite) and polytetrafluoroethylene (PTFE) as a binder on stainless steel (SUS) mesh. The analyses were conducted in 2M Li_2SO_4 aqueous electrolyte.

4.1.4 Calculations

The specific capacitance (F g^{-1}) was calculated from the cyclic voltammograms (CVs) according to the following equation:

$$C = \frac{In_{CV}}{v \times \Delta V \times m}$$

where, In_{cv} is the area of integral for the discharged CV curve (AV), v is the sweep rate (V s^{-1}), ΔV is the potential window (V) and m is the mass of electrode materials (g) [178].

The specific power (P, W kg^{-1}) at certain scan rate v (V s^{-1}) was calculated by integrating discharged area (IV) of CV curve as follows [179]:

$$P = \int_{V_1}^{V_2} I/m \ dv$$

where the V_1 is 0.0 V and the V_2 is 0.8 V.

And the specific energy W (Wh kg^{-1}) was obtained using the following equation [179]:

$$W = \frac{V_2 - V_1}{v \times 3600} \times \int_{V_1}^{V_2} \frac{I}{m} \ dv$$

The discharge/charge energy ratio (μ) was calculated as following equation:

$$\mu = \frac{W_d}{W_c} \times 100 \ \%$$

where W_d and W_c are the discharge and charge specific energy, respectively. The discharge and charge specific energy (W, Wh kg^{-1}) values at certain scan rate v (V s^{-1}) were calculated by integrating discharged and charged area of CV curve.

4.2 Results and discussion

4.2.1 Preparation of the 3D metal/carbon composite

The 3D metal/carbon composite (3DMC) was fabricated by an "intrusion and heat treatment" process (Figure 4-1(a)) using an agarose gel. Agarose gel,

extracted from red algae, is a carbon-based biopolymer with a 3D interconnected pore structure [180]. In previous research, D. Walsh et al., reported free-standing 3D metal structures which were synthesized using a polysaccharide as a soft sacrificial template [181]. Their proposed method was applicable to the construction of 3D structures with a wide spectrum of metal constituents, such as gold, silver, copper oxide, maghemite (Fe_2O_3). In addition, the consumption of the metal precursor does not exceed required amounts.

Herein, we expanded this soft template method, utilizing its inherent signature strengths, to fabricate a high-power supercapacitor electrode. The metal precursor, $HAuCl_4$ in the case of Au, was intruded into the hydrophilic pores of the agarose gel by capillary force [181]. The precursor ions inside the pore were then completely reduced by treatment with an excess amount of reducing agent ($NaBH_4$), subsequently this composite was dried and carbonized. During the carbonization process, a 3D metal-lining architecture was produced by the sintered metal nanoparticles within the complicated pore spaces (Figure 4-2) and the agarose gel was simultaneously carbonized to amorphous carbon. Our proof-of-concept studies are based on Au, the most well-known member of the metal species with excellent conductivity, although they are not limited to this material. We proved that this procedure can be applied to the construction of other metal/C hybrid such as bicontinuous Cu/C hybrid (Figure 4-3 and 4-4). The construction of a 3D metal structure inside the pore causes a pore blockage effect, resulting in the formation of a bicontinuous material without an inner pore structure. Intimate contact between the 3D Au and carbon is crucial for the achievement of an improved electrical conductivity at the interface of the bicontinous Au/C [182, 183]. The prepared composite had a brain coral-like structure as shown in Figure 4-1(b) and (c) [87]. In addition, to confirm the

continuous characteristics of the 3D structured metal inside the carbon, the composite was calcined in air and removed the carbon component (Figure 4-1(d)).

4.2.2 Electrochemical properties of the 3D metal/carbon composite

The electrochemical properties and resistive behavior of the prepared 3DMC supercapacitor electrodes were examined by cyclic voltammetry and impedance spectroscopy measurements. These analyses were performed in the potential window from 0 V to 0.8 V. An aqueous Li_2SO_4 solution was used as the electrolyte because of the high electrosorption properties of Li^+ [85].

Cyclic voltammograms (CVs) at various scan rates (from 0.01 V s^{-1} to 1,000 V s^{-1}) for the 3DMC electrode are summarized in Figure 4-5(a). Activated carbon as a commercial electrode and graphite as a highly conductive material were also examined for comparison [184, 185]. CV curves of the 3DMC show a symmetrical and rectangular shape, indicative of excellent capacitance properties, even at a very high scan rate of 1,000 V s^{-1}, indicating that the 3DMC can be charged/discharged 625 times in a second. On the other hand, activated carbon and graphite lose their symmetrical charge/discharge area at 0.01 V s^{-1}, 50 V s^{-1}, respectively (Figure 4-6). The quantified discharge/charge energy ratio (%) from CVs, as described in Figure 4-5(b), clearly confirms the excellent energy efficiency of the 3DMC electrode at high scan rate. These results are in good agreement with galvanostatic charge-discharge measurements (Fig. S5, ESI†). The overall internal resistance causes not only a narrower loop in CV diagrams, but also results in a short-lived supercapacitor by heat or defects [75-79]. Interestingly, the 3DMC electrode showed reproducible and stable

capacitive behavior during 1,000,000 charge-discharge cycles (Fig. 2(c)).

The specific capacitance of the 3DMC was 24 mF g^{-1} at 100 V s^{-1}, which surpasses the values for activated carbon and graphite at a lower scan rate (50 V s^{-1}) showing 0.48 mF g^{-1}, 20 mF g^{-1}. A high level scan rate means that a high power for prompt action is available, which should be accompanied by an ideal capacitive behavior. Figure 4-5(b) shows a comparison of the specific capacitance as a function of scan rate for the electrodes with a 3DMC, activated carbon and graphite. Although activated carbon and graphite have a higher specific capacitance and a capacitive behavior of up to 0.05 V s^{-1} (activated carbon), 5 V s^{-1} (graphite), the performance is dramatically decreased at a higher scan rate due to the charge resistive behavior of the material. Importantly, discharge current of 3DMC has a linear dependence on the scan rates up to 1,000 V s^{-1}. It means that the 3DMC retains its ideal capacitance even under conditions of ultrafast operation. This concept was also verified by comparing 3DMC with a mixture of Au particle and carbonized agarose gel (Figure 4-8).

A comparison of Nyquist plots of the 3DMC, activated carbon and graphite electrodes are shown in Figure 4-9(a). In the plots for activated carbon and graphite, a semi-circle appears in the high frequency region. However, no semi-circle was observed in the case of the 3DMC electrode, which indicates that electronic contact resistance is negligible [186-189]. I was also able to verify that the 3DMC electrode is not involved in Warburg impedance regarding mass transfer resistance (by the *De Levie* model), based on the fact that it has no line that intersects the real axis at a near –45° angle, unlike activated carbon and graphite [84, 186-189]. Its equivalent circuit and details are described in Figure 4-10.

Impedance phase angle data as a function of frequency for the 3DMC,

activated carbon and graphite are shown in Figure 4-9(b). Both the 3DMC and graphite showed capacitive behavior at a low frequency and resistive behavior at a high frequency. However, the phase transition of 3DMC with a decrease in frequency is much faster than that of graphite, because the fast charge/discharge ability permits high-frequency operation with near-ideal capacitive behavior. 3DMC has an impedance phase angle value of –76° at 120 Hz, which suggests that this electrode is also highly applicable for filtering ac voltage ripples [84]. This represents a solution for overcoming the low volumetric efficiency of commonly used electrolytic capacitors [83, 84]. Meanwhile, the activated carbon electrode does not show such capacitive behavior, even at the relatively low frequency region due to its complex inner pore structure and poor contact between the electrode materials and the current collectors [186, 187].

The non-porous structure of 3DMC is an important advantage for high power, but there is a drawback regarding on relatively low specific energy. To complement specific energy of 3DMC, I introduce a NH_3 treatment technique for carbon activation. Carbonization in a NH_3 atmosphere generate doped nitrogen in carbon (Figure 4-11(a)), which resulting in significant increase of capacitance due to the pseudo-capacitive effect as previously reported [190, 191]. Consequently, NH_3-carbonized 3DMC (NH_3-3DMC) exhibited 7 times higher specific capacitance than Ar-carbonized 3DMC (Ar-3DMC) (Figure 4-11(b)). NH_3-3DMC also showed high stability at the very high scan rate up to 1,000 V s^{-1}, which means that NH_3-3DMC retains high conductance as of Ar-3DMC (Figure 4-12). The specific energy and power level of electrodes summarized in Ragone plot (Figure 4-13).

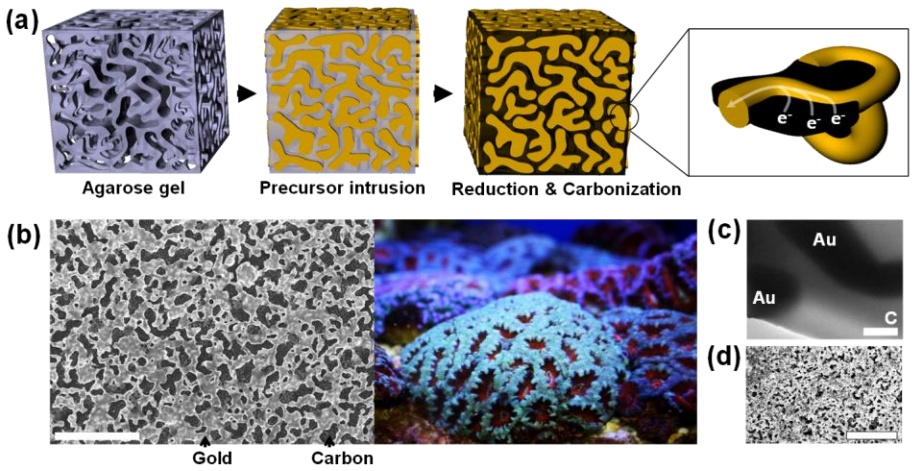

Figure 4-1. (a) Schematic illustration of the fabrication procedure of 3D metallic current collector and carbon composite. (b) SEM image of synthesized carbon/3D Au composite (left, scale bar is 5 μm) and picture of brain coral (right, Acanthastrea). (c) TEM images of synthesized carbon/3D Au composite (scale bar is 500 nm). (d) SEM images of 3D structured Au without carbon after air-calcination (scale bar is 5 μm).

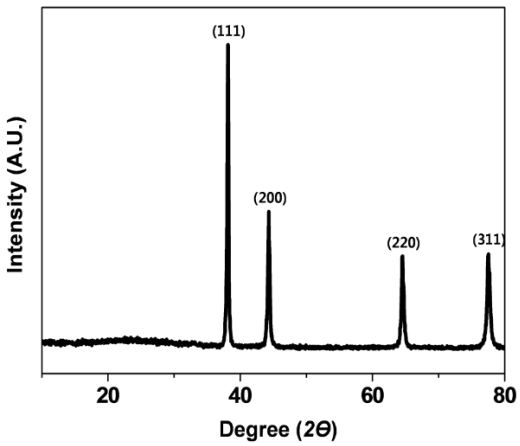

Figure 4-2. Crystalline structure of 3DMC. All Bragg reflectrions, observed in the XRD spectra, are indexed on the basis of the fcc structure of Au. Therefore, 3DMC consists of amorphous carbon and Au with no peaks corresponding to graphitic carbon.

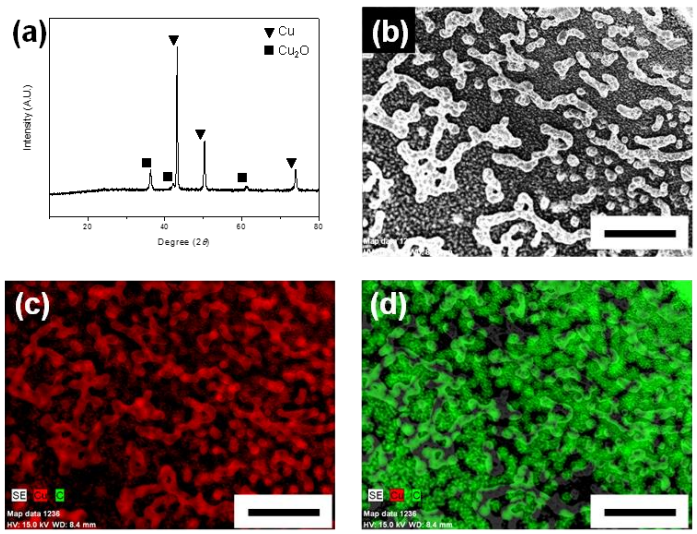

Figure 4-3. Cu-based 3DMC. (a) Crystalline structure of Cu-based 3DMC, the observed in XRD spectra, indicates the co-existence of amorphous carbon and partially oxidized Cu. (b) SEM image of Cu/C bicontinuous structure. EDS atomic analysis results of Cu-based 3DMC; (c) copper and (d) carbon. All scale bars are 30 μm.

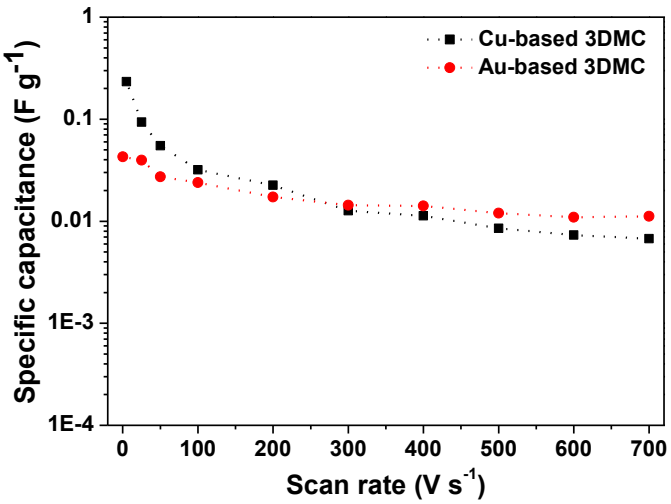

Figure 4-4. Specific capacitance *versus* scan rate for Cu-based 3DMC (black) and Au-based 3DMC (red) electrode. Due to the partially oxidized 3D Cu, rate capability of carbon/Cu hybrid remained slightly below that of carbon/Au hybrid.

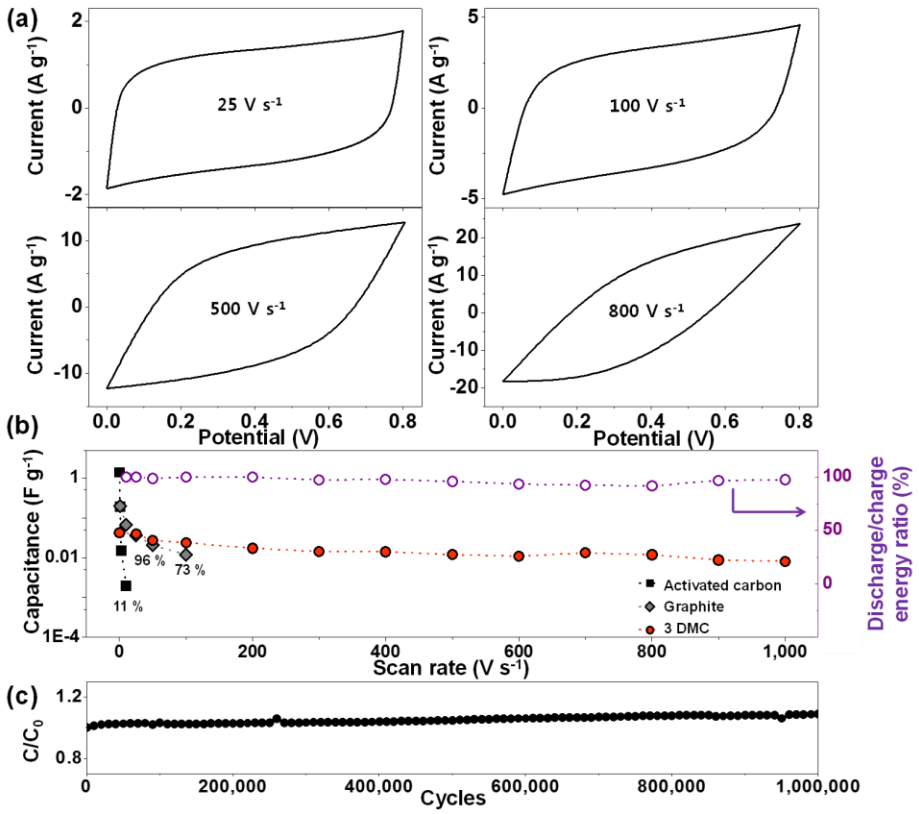

Figure 4-5. (a) Cyclic voltammograms for 3DMC electrode obtained at different scan rates. (b) Specific capacitance of 3DMC electrode as a function of scan rate. Discharge/charge energy ratios (%) indicate that 3DMC electrode fully charge/discharged at each scan rate. (c) Relative capacitance as a function of charge/discharge cycles at scan rate of 200 V s^{-1}. C_0 is the capacitance from the first cycle.

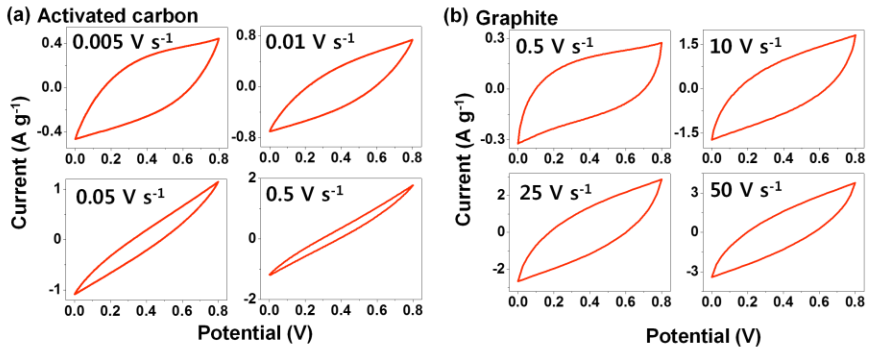

Figure 4-6. Cyclic voltammograms for commercial activated carbon (a) and graphite (b) electrodes obtained at different scan rates.

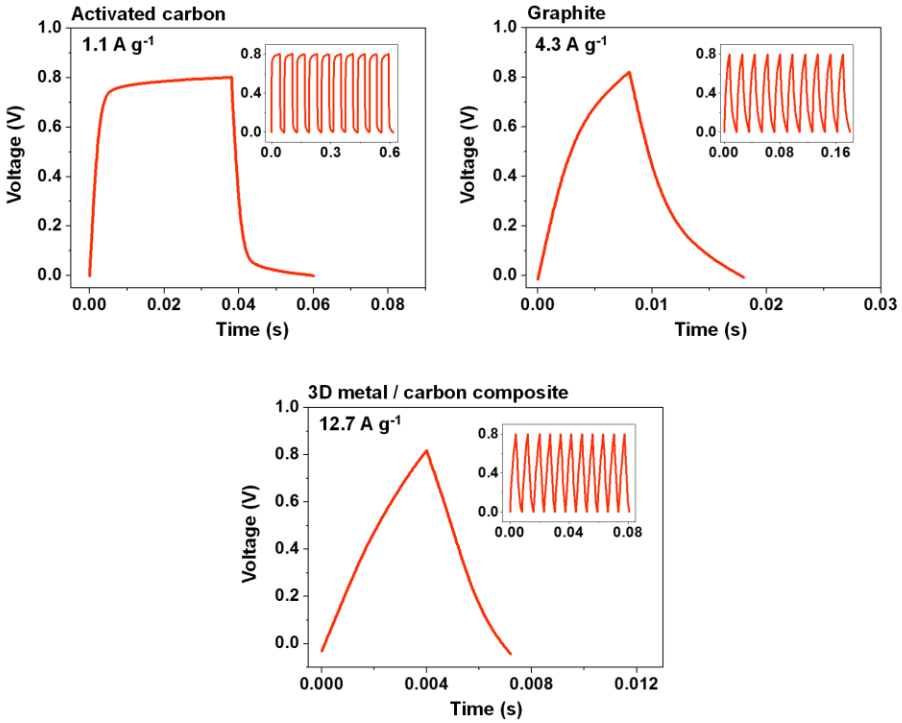

Figure 4-7. Charge-discharge curves (voltage *vs.* time) for activated carbon, graphite and 3DMC electrodes. The specific current of activated carbon, graphite and 3DMC electrode are 1.1 A g^{-1}, 4.3 A g^{-1}, and 12.7 A g^{-1}, respectively. Each values of specific current were determined by the peak currents in the CV analysis at a scan rate of 0.5 V s^{-1}, 100 V s^{-1} and 500 V s^{-1}, respectively.

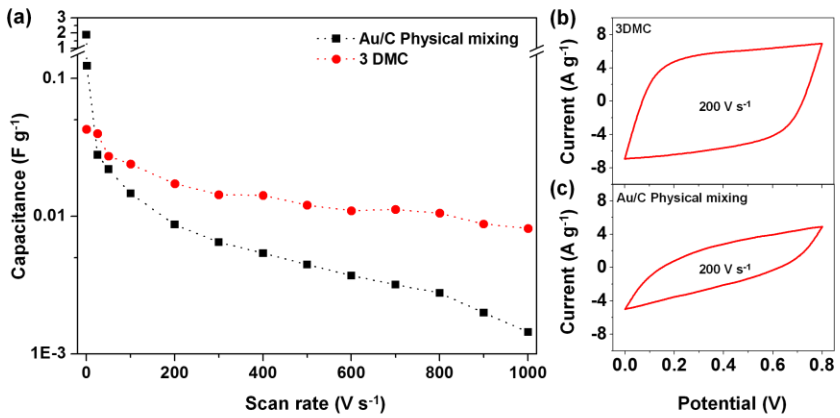

Figure 4-8. (a) Specific capacitance of 3DMC and Au particle/carbonized agarose composite electrode as a function of scan rate. Cyclic voltammograms for 3DMC (b) and Au particle/carbonized agarose composite (c) obtained at scan rate of 200 V s^{-1}. Amorphous carbon obtained by carbonizing an agarose gel and Au particles prepared by aqueous reduction of $HAuCl_4$ were mixed by ball-milling.

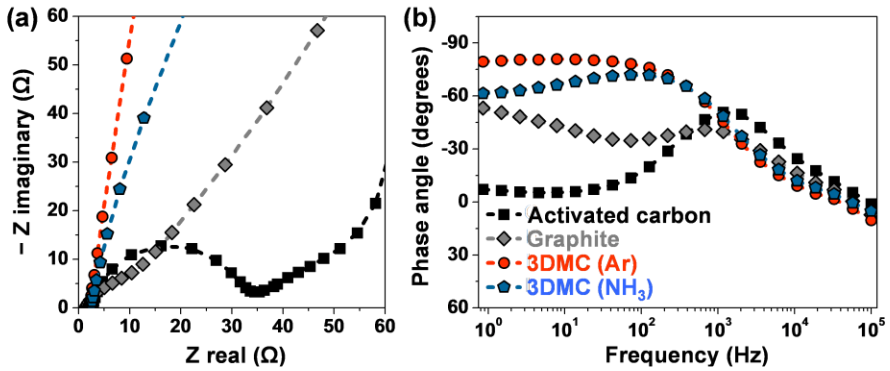

Figure 4-9. Nyquist impedance plots (a) and impedance phase angle as a function of frequency (b) of the 3DMC (Ar and NH_3 carbonized), activated carbon and graphite at an applied potential of 0.4 V, an ac amplitude of 10 mV, and frequencies of 100 mHz - 100 kHz.

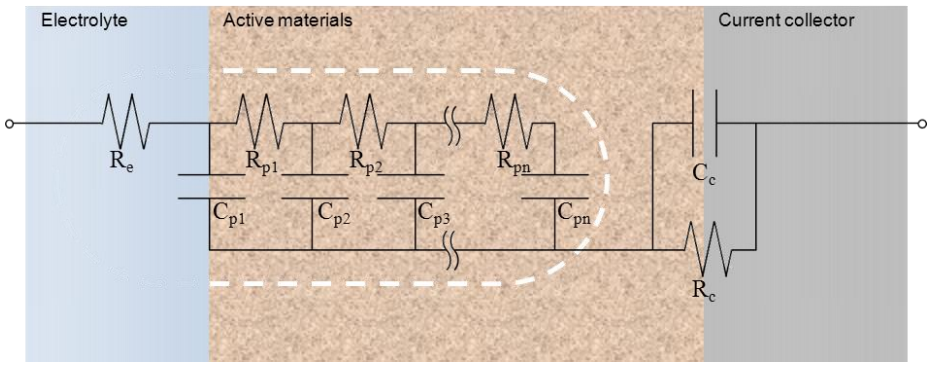

Figure 4-10. Equivalent circuit model used to interpret the measured impedance spectra of the electrodes. These elements include electrolyte resistance (R_e), capacitance (C_c) and resistance (R_p) from ion migration through the inner pore structure (*De Levie* model). In the case of activated carbon and graphite electrodes, this circuit acceptably simulates the results of the Nyquist plot (Figure 4-9(a)). On the other hand, the equivalent circuit of 3DMC is reduced to a simple RC circuit, because the pore structure resistance and charge transfer barriers between the electrode and current collector are negligible.

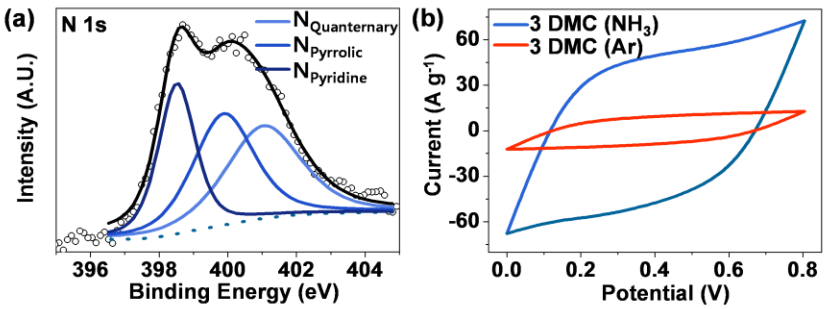

Figure 4-11. (a) XPS N1s region of NH_3 carbonized 3DMC. Deconvoluted spectra shows functional groups of nitrogen and three peaks can be assigned to quaternary (401.2 eV), pyrrolic or pyridone (400.5 eV) and pyridine species (398.5 eV). (b) Cyclic voltammograms for NH_3 carbonized 3DMC electrode (blue) obtained at scan rates 500 V s^{-1}. Measurements from a Ar carbonized 3DMC electrode (red) are shown for comparison.

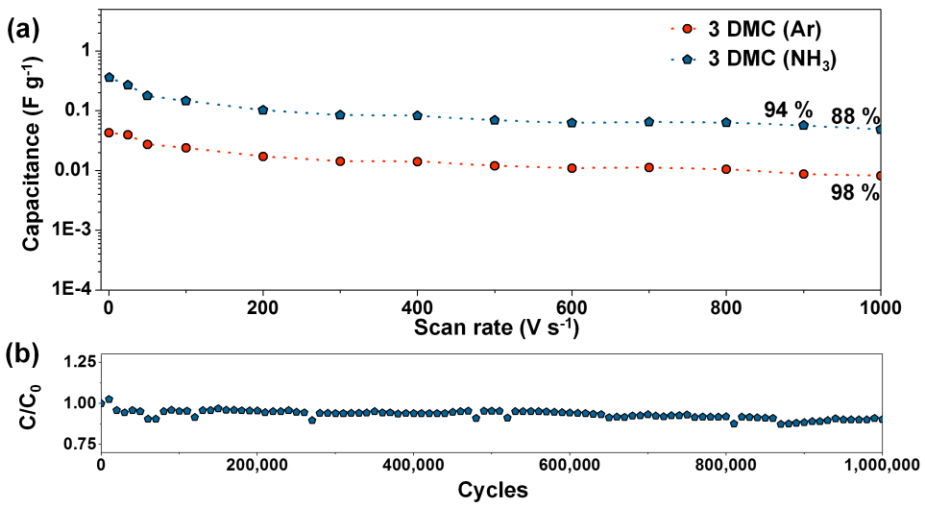

Figure 4-12. (a) Comparison of the specific capacitance of Ar, NH_3 carbonized 3DMC electrode as a function of scan rate. NH_3 carbonized electrode (blue) show 7 times higher specific capacitance than that of Ar carbonized electrode (red). (b) Stability test during the 1,000,000 charge/discharge.

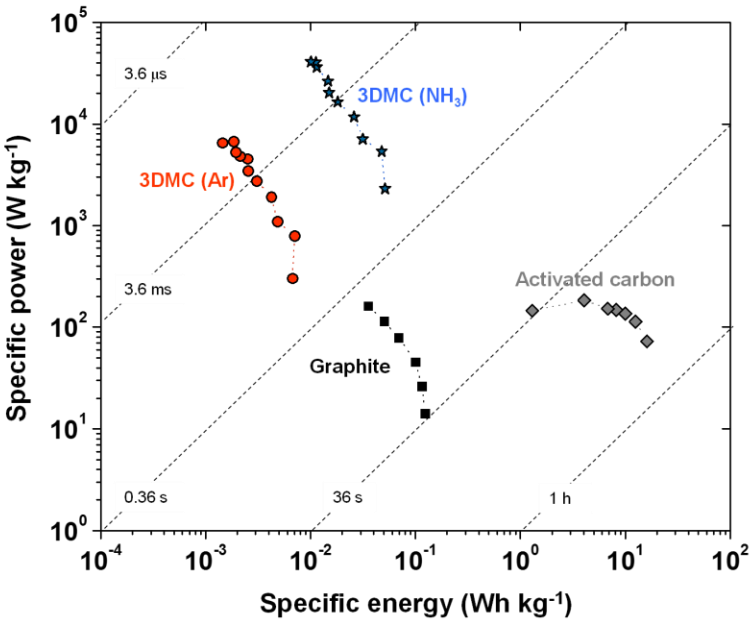

Figure 4-13. Ragone plot (specific power against specific energy) for prepared 3DMC (Ar, NH_3), graphite, activated carbon-based electrodes. Times shown in plot indicate the time constants of each material, which are calculated by dividing the specific energy by the power.

Chapter 5. Hybrid MnO_2 Film with Agarose Gel for Enhancing the Structural Integrity of Thin Film Supercapacitor Electrodes

5.1 Experimental

5.1.1 Fabrication of hybrid MnO_2 electrodes

For the preparation of the agarose gel-coated substrate, a 1% (w/v) solution of agarose powder in deionized (DI) water was heated using a microwave oven. After the complete dissolution of the agarose, the solution was cast on a stainless steel (SS) plate (1 cm^2 circle) by a dip-coating method, and the agarose solution was allowed to form a gel on the plate at room temperature for 4 hours in a sealed container. The Mn precursor solution for electrodeposition was prepared by dissolving 0.1 M of $Mn(NO_3)_2$ and 0.1 M of $NaNO_3$ in the DI water. The electrodeposition was performed potentiostatically at 1.2 V (vs Ag/AgCl) for various periods of time (10~1500 seconds). A saturated Ag/AgCl and a platinum plate were used as the reference and counter electrode, respectively. After electrodeposition, the deposited films were washed with DI water and dried at room temperature for 24 hours.

5.1.2 Characterizations

The surface morphology and composition of the prepared films were characterized by scanning electron microscopy (SEM, Carl Zeiss, SUPRA 55 VP) and focused-ion beam microscopy (FIB, Carl Zeiss, AURIGA). For the electrochemical measurements, cyclic voltammetry (CV) was performed in a standard three-electrode configuration (Iviumstat electrochemical analyzer, Ivium Technology) with an aqueous 1.0 M Na_2SO_4 solution as electrolyte. Electrochemical impedance spectroscopy (EIS) was conducted at an applied potential of 0.4 V, an ac amplitude of 10 mV, and frequencies of 100 mHz - 100 kHz. We used a saturated Ag/AgCl as the reference electrode and platinum counter electrode. The N_2 adsorption-desorption isotherms were recorded on a Micrometrics ASAP-2010 system to analyze pore structure and Brunauer-Emmett-Teller (BET) surface area of the film. The X-ray diffraction (XRD) patterns were obtained in 20~80° using X-ray diffractometer (Rigaku, D-MAX2500-PC).

5.1.3 Calculations

The capacitance (F) was calculated from cyclic voltammograms (CVs) using the following equation [178]:

$$C = \frac{In_{CV}}{v \times \Delta V}$$

where, In_{CV} is the area of integral for the discharged CV curve (AV), v is the sweep rate (V s^{-1}), ΔV is the potential window (V).

The specific capacitance (F g^{-1}) and areal capacitance (F cm^{-2}) were obtained by dividing capacitance by deposited mass (g) and area (cm^2), respectively.

5.1.4 3D finite elemental method modelling

A layer of agarose gel thin film was modeled as a linear elastic material. The modeled agarose film was 0.5 μm in thickness and 10 mm in diameter. The 10-node tetrahedron element was used to construct the agarose gel model. The calculated values were derived values for Young's modulus (1.2×10^5 Pa) and Poisson's ratio (0.32) found in the literatures [192].

The stress (σ) and strain (ε) of materials are described by Hooke's law:

$$\sigma_i = D_{ij} \times \varepsilon_i$$

where D_{ij} is elasticity matrix.

If the agarose gel is isotropic, the D_{ij} is described as follows:

$$D_{ij} = \frac{E(1-\nu)}{(1+\nu)(1-2\nu)} \begin{bmatrix} 1 & \gamma & \gamma & 0 & 0 & 0 \\ \gamma & 1 & \gamma & 0 & 0 & 0 \\ \gamma & \gamma & 1 & 0 & 0 & 0 \\ 0 & 0 & 0 & \beta & 0 & 0 \\ 0 & 0 & 0 & 0 & \beta & 0 \\ 0 & 0 & 0 & 0 & 0 & \beta \end{bmatrix}, \quad \sigma_i = \begin{bmatrix} \sigma_{xx} \\ \sigma_{yy} \\ \sigma_{zz} \\ \sigma_{xy} \\ \sigma_{yz} \\ \sigma_{zx} \end{bmatrix}, \quad \varepsilon_i = \begin{bmatrix} \varepsilon_{xx} \\ \varepsilon_{yy} \\ \varepsilon_{zz} \\ \varepsilon_{xy} \\ \varepsilon_{yz} \\ \varepsilon_{zx} \end{bmatrix}$$

$$\gamma = \frac{\nu}{1-\nu}, \qquad \beta = \frac{1-2\nu}{2(1-\nu)}$$

where E is Young's modulus and ν is Poisson's ratio.

Tensile-deformed structure was generated by applying the pressure of 1.332×10^{-10} Pa to agarose model in the direction of normal-to-xy plane. In Figure 5-5, blue backgrounds indicate non-deposited area in which there are no deformation, strain and stress.

5.1.5 Density functional theory calculations

Calculations were performed with the Vienna Ab initio Simulation Package (VASP) [133], employing the projector augmented wave (PAW) method [135]. Generalized gradient approximation (GGA) with the Perdew-Burke-Ernzerhof (PBE) functional was used [134]. The kinetic energy cutoff was set to a 400 eV. The first Brillouin zone integration was accomplished using the Monkhorst-Pack scheme. The $1\times1\times1$ and $2\times2\times2$ k-point sampling was done for agarose and MnO_2, respectively. As shown in Figure 5-10, the double helix structure of agarose gel occupies larger unit cell than the ramsdellite structure of MnO_2 [193]. A vacuum layer of 15 Å was taken in non-periodic directions for agarose. For the calculations of MnO_2 structures, DFT+U within Dudarev's approach was used with $U_{eff} = 4.0$ to account for the on-site Coulomb interaction in the localized *d* orbital [136].

The proton migrations through agarose and MnO_2 structure are visualized in Figure S1. For a fair comparison, a proton is translocated as it passes through the largest void in the unit cell structure in both cases. Figure 4 indicates the calculated energy barrier during the proton migration, which proves high

penetrability of proton through agarose gel.

Since rigorous Nudged Elastic Band (NEB) [141] calculations in our system would be computationally very expensive (72 C, 107 H and 54 O atoms in a agarose unit cell), I used the DFT-calculated total energies at each position of proton relative to the initial position as the relative energy profile along the migration pathway. The migration barrier calculated in this way is possibly over-estimated (Figure 4). However, it can be speculated that at least the relative comparison between proton migrations through agarose and MnO_2 would still be effective for the purpose of qualitative analysis.

5.2 Results and discussion

5.2.1 Synthesis and characterization of agarose gel-wrapped MnO_2 electrode

Figure 5-1(a) shows schematic illustrations of the agarose gel-wrapped (AGW) MnO_2 films that were prepared by electrodeposition. Agarose gels, coated on the SS plate, function as a pre-coated and elastic wrapping layer for the deposited MnO_2. During the anodic electrodeposition, Mn^{2+} ions readily migrate through the gel layer, because the hydrophilicity and porous properties of the framework provide sufficient accessibility of the Mn^{2+} to current collector (SS). The electrodeposited MnO_2 films showed porous structure with BET surface area of 255.33 m^2 g^{-1} and crystalline structure containing γ-MnO_2 phase as proved in Figure 5-2 and 5-3.

As shown in Figure 5-1(b) and 5-4, in the absence of an agarose gel layer, the deposited MnO_2 films lose their structural rigidity, consequently becoming fragmented and separated from the current collector. In contrast, in the presence of an agarose gel layer, no cracks or isolations were observed (Figure 5-1(c)) when the same weight of MnO_2 was deposited. As indicated by Figures 5-1(a) and 5-1(d), the MnO_2 film that was grown on the current collector is enclosed within the agarose gel layer, resulting in 3-layered structure (agarose gel / MnO_2 / SS). The hierarchical structures of MnO_2 form as it is pushing up the gel layer and the elastic recovery force of the gel is exerted in the opposite direction (Figure 5-1(e-g)).

A 3D FEM simulation was performed to prove that the agarose gel has abundant elastic properties and it maintained in a hybridized form, even at high MnO_2 loadings. As shown in Figure 5-5(a), I assumed that the gel is tensile-deformed along the Z-direction by about ~1.8 μm on the basis of previous SEM data. The maximum elastic strain and stress in such a deformation were calculated to be 2.6×10^{-7} μm/μm and 3.0×10^{-2} Pa, respectively (Figure 5-5(b) and (c)). The value for equivalent stress is very low, compared to the reported failure stress of the gel (48 KPa), indicating that the agarose gel completely encloses the deposited MnO_2 film due to its high elasticity [194].

Based on the above findings, it can be concluded that the agarose gel effectively prevents the MnO_2 film from disintegrating and plays a key role in the formation of a robust MnO_2 film by virtue of its supportive and elastic properties. As a result, the agarose gel-wrapping permits intimate contact to be achieved between the MnO_2 film and the current collector.

5.2.2 Electrochemical measurements

The electrochemical properties and resistive behavior of the prepared AGW MnO_2 supercapacitor electrodes were evaluated by means of cyclic voltammetry and impedance spectroscopy measurements. These analyses were performed in the potential window from 0 V to 0.8 V.

The CVs curves for the AGW MnO_2 films with various weights of deposited MnO_2 (~0.769 mg cm^{-2}) are summarized in Figure 5-6(a) and (b). The deposited MnO_2 was quantified by measuring the accumulation capacity (mAh) during electrodeposition and the results show a linear correlation (R^2=0.99) between the measured accumulation capacity (mAh) and the the weight of the deposited MnO_2 (Figure 5-7) [101]. All CV curves were obtained at a scan rate of 10 mV s^{-1} and show a symmetrical and rectangular shape, indicative of good capacitance properties. Understandably, when the electroactive MnO_2 loading is increased, the overall capacitance of the electrode is also improved. In Figure 5-6(a), the capacitance of a bare MnO_2 film was increased with increasing amounts of deposited MnO_2 up to a level of 0.073 mg cm^{-2}. When the amount of deposited MnO_2 reached 0.116 mg cm^{-2}, however, the capacitance of the electrode abruptly decreased. This result can be rationalized by assuming that there is a certain threshold regarding loading capacity (g cm^{-2}) for stable charge transfer and energy storage. MnO_2-deposited films over the threshold (0.073~0.116 mg cm^{-2}) become fragile and the initially deposited form of the film can no longer be retained (Figure 5-1(b)). To the contrary, AGW MnO_2

films show a consistent increase in capacitance even at relatively high MnO_2 loading levels (up to 0.769 mg cm^{-2}).

For a clear comparison between bare MnO_2 and AGW MnO_2, the values for specific capacitance (F g^{-1}) and areal capacitance (mF cm^{-2}) are plotted as a function of deposition weight in Figures 5-6(c) and (d). Under the low loading conditions employed (below 0.02 mg), both bare MnO_2 and AGW MnO_2 showed high capacitance values of 200~400 F g^{-1} the level of which is similar to that found in literature reports [90, 95, 195]. However, the specific capacitances of a bare MnO_2 film sharply decreased when the deposition weight exceeded the threshold (indicated by the arrow) such that a value of 20.90 F g^{-1} was found when MnO_2 was deposited at a level of 0.116 mg cm^{-2}. Importantly, the MnO_2 inside the agarose gel films maintained its superior specific capacitance in the vicinity of 100 F g^{-1} up to 0.75 mg cm^{-2} (121.16 F g^{-1} at 0.23 mg cm^{-2}, 107.21 F g^{-1} at 0.41 mg cm^{-2}, and 64.92 F g^{-1} at 0.75 mg cm^{-2}). In Figure 5-6(d), while the maximum areal capacitance of bare MnO_2 was 8.74 mF cm^{-2}, I was able to achieve a level of 52.55 mF cm^{-2} by taking advantage of the agarose gel-wrapping effect. The areal capacitance increased linearly up to 46.30 mF cm^{-2} with increasing amount of deposited MnO_2 increased (~0.41 mg cm^{-2}). This value for the areal capacitance surpasses previously reported results regarding the pseudocapacitive performance of electrodeposited MnO_2 [195-197]. The rate capability of the AGW MnO_2 was investigated at various rates from 10 mV s^{-1} to 1000 mV s^{-1} because a fast charge-discharge can adversely affect the structural stability of the film (Figure 5-8). Importantly, when the rate returns to the initial 10 mV s^{-1} after 30 cycles, the AGW MnO_2 recovers its

original capacitance (107.21 F g^{-1} at 0.41 mg cm^{-2}). In addition, no evidence of capacitance fading was found for AGW MnO_2 electrodes with a deposition weight of 0.77 mg cm^{-2} after 5000 cycles (within 10 % of the initial capacitance) (Figure 5-9).

DFT calculations were conducted to predict the accessibility of electrolyte to the agarose gel-wrapped MnO_2. According to the previous reports regarding the charge storage mechanism of MnO_2, the pseudocapacitance of MnO_2 depends on the migration of protons into and out of the MnO_2 lattice under applied electrical fields [198]. When MnO_2 is reduced to produce MnOOH, protons are incorporated into the MnO_2 lattice. Based on this fundamental knowledge, the calculated energies required for proton migration through an agarose gel and a MnO_2 structure were compared. Figures 5-10 and 5-11 show the calculated relative energy at each point of the path, and indicates that the potential energy barrier for proton migration through the MnO_2 lattice is much larger than that for the migration of a proton through the agarose film. Therefore, the agarose gel is not the main obstacle to proton migration. Consequently, the loss of performance caused by agarose gel-wrapping can be negligible. This excellent ion penetrability of agarose gels is also attributed to their large number of pores.

The Nyquist impedance plots for both electrodes (Figure 5-12) are very similar to both bare MnO_2 and AGW MnO_2 under conditions in which small amounts of MnO_2 were deposited. This result indicates that the resistive behavior of both electrodes are nearly identical, which are consistent with the DFT calculations. However, when the amount of deposited MnO_2 is increased to 0.116 mg cm^{-2}, the R_{ct} in bare MnO_2 is dramatically increased. These results

are in agreement with the drop in the capacitances of electrodes in the above-mentioned CVs (Figure 5-6(a)). In contrast, AGW MnO_2 maintained an equivalent Rct at a deposition weight of both 0.057 and 0.158 mg cm^{-2} (Figure 5-12(b)). This clearly demonstrates that the substrate adhesiveness of the agarose gel film plays a significant role in retaining the initially deposited forms of a MnO_2 layer without any loss electrical connectivity at the MnO_2/SS interface.

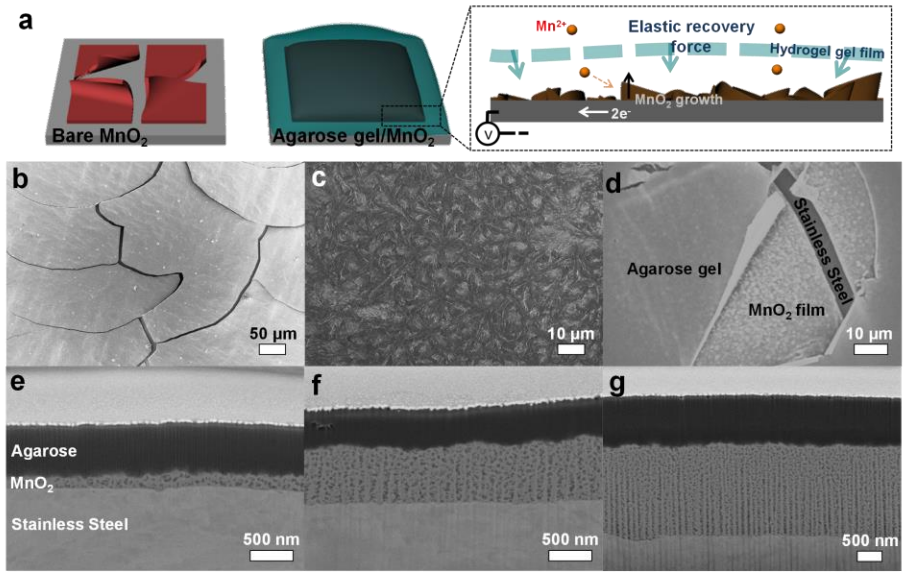

Figure 5-1. Schematic illustration of agarose gel-wrapped MnO_2 film (a). SEM images of the bare MnO_2 films (b), and SEM images of top views (c, d) an side views (e, f, g) of the agarose gel-wrapped MnO_2 films. Deposition amounts of MnO_2 are 0.300 mg cm^{-2} (b, c, d), 0.057 mg cm^{-2} (e), 0.168 mg cm^{-2} (f) and 0.361 mg cm^{-2} (g), respectively.

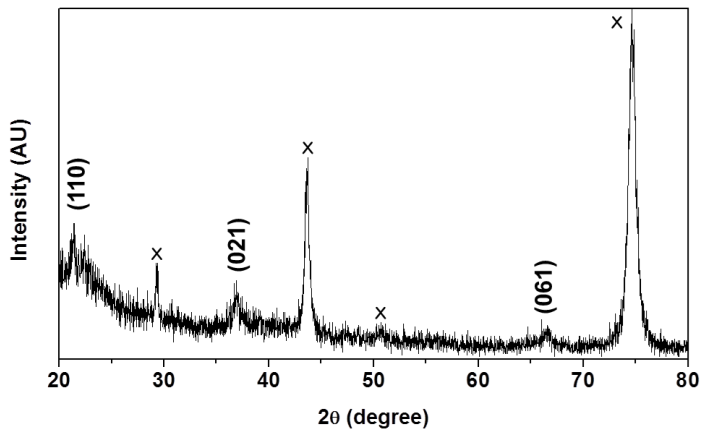

Figure 5-2. XRD pattern of the films containing electrodeposited MnO_2. The diffraction peaks except that for SS substrate and residues ($NaNO_3$) can be assigned to the crystal plane of (110), (021), and (061), which indicates that this film is composed of γ-MnO_2 phase [195].

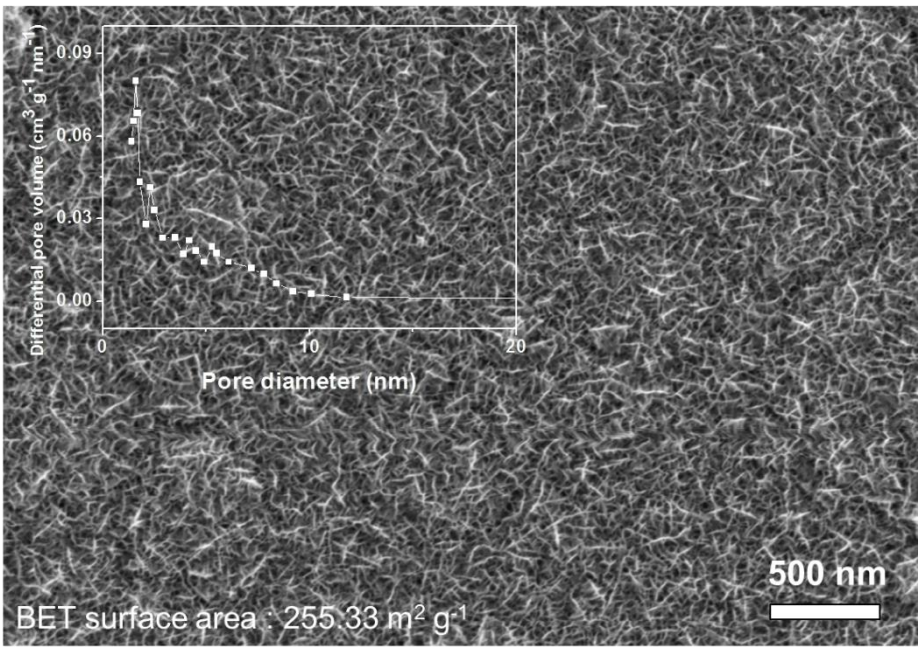

Figure 5-3. Magnified SEM image of MnO_2-deposited film. Inset graph represents Barrett-Joyner-Halenda (BJH) pore size distribution curves for the film. The anodically electrodeposited MnO_2 films show porous structure containing both macro-porosity and micro-porosity. Total surface area measured by BET method is 255.33 m^2 g^{-1}.

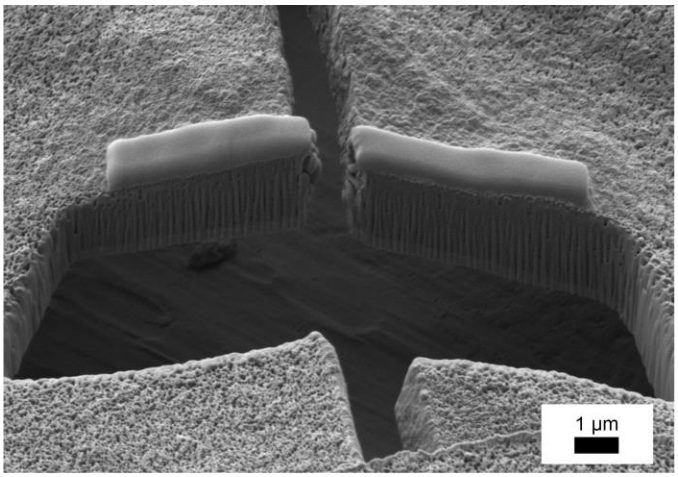

Figure 5-4. SEM image of the bare MnO_2 film after FIB milling. The weight of deposited MnO_2 is 0.299 mg cm^{-2}.

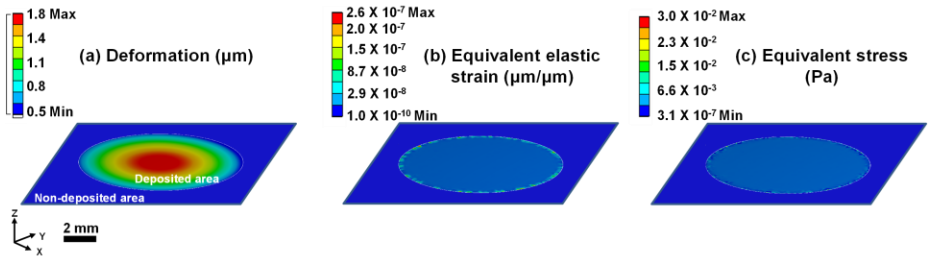

Figure 5-5. 3D FEM results. Deformation analyses (a) under high MnO_2 loading condition (maximum 1.8 μm depth), the calculated equivalent elastic strain (b) and stress (c).

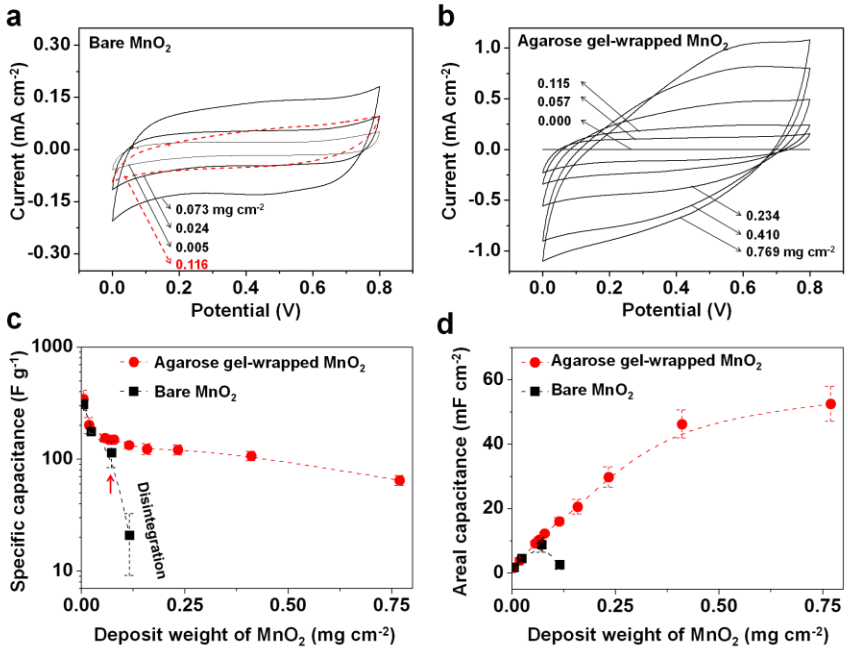

Figure 5-6. Cyclic voltammetry (CVs) results for bare MnO_2 electrodes (a) and an agarose gel-wrapped MnO_2 electrode (b) under different loading conditions. Specific capacitance (c) and areal capacitance (d) of electrode as a function of deposition weight of MnO_2.

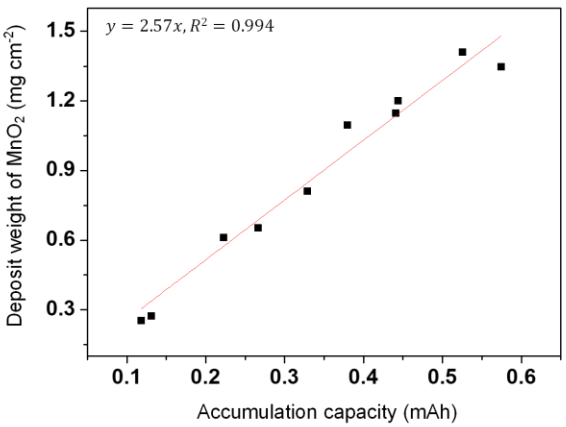

Figure 5-7. Deposit weight of MnO_2 as a function of accumulation capacity during electrodeposition.

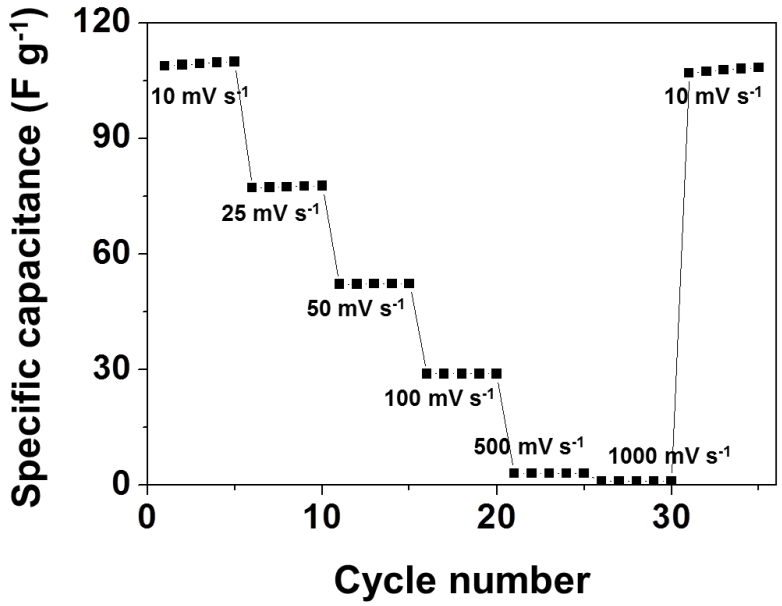

Figure 5-8. Rate capability of AGW MnO_2 (deposit weight of 0.41 mg cm^{-2}) at various scan rates between 10 mV s^{-1} and 1000 mV s^{-1}.

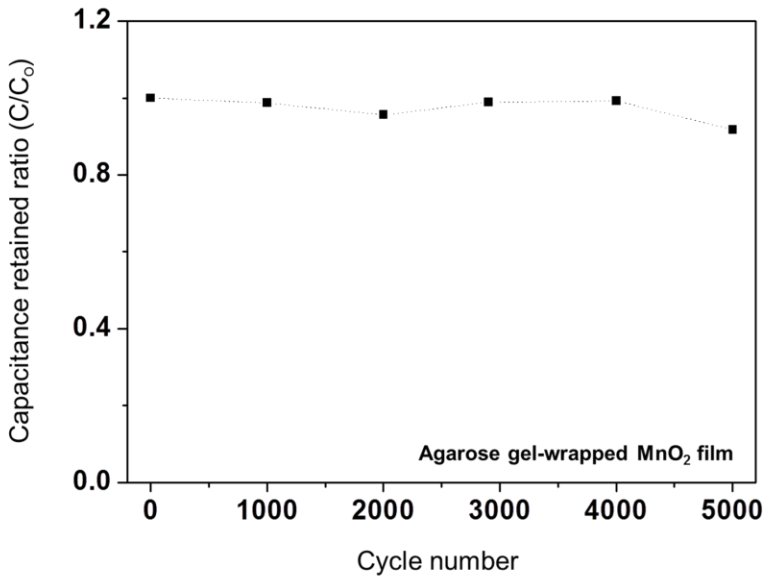

Figure 5-9. Relative capacitance of AGW MnO_2 as a function of charge-discharge cycles at a current density of 1 mA cm^{-2}.

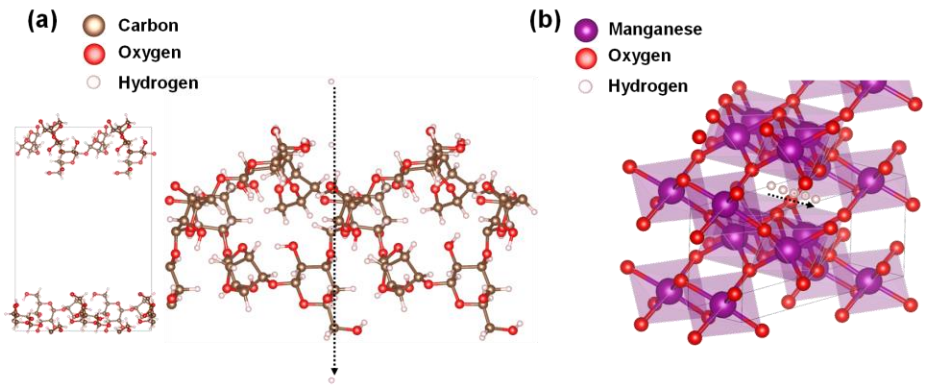

Figure 5-10. The agarose double helix structure (a), and ramsdellite MnO_2 (b). Arrow indicates each migration path of proton. Hexahedron represents boundary of each unit cell.

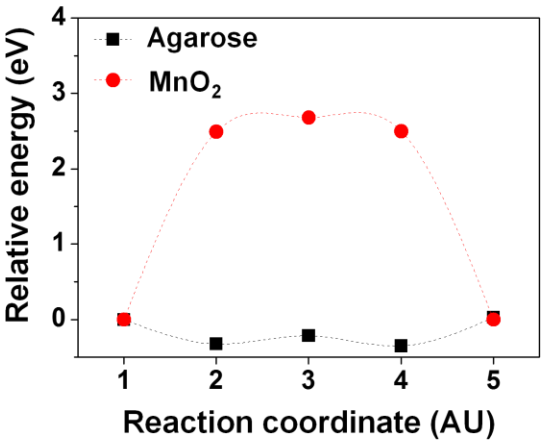

Figure 5-11. DFT calculated energy profile along the proton migration paths. The calculated total energies at each position of proton relative to the initial position are shown in y-axis.

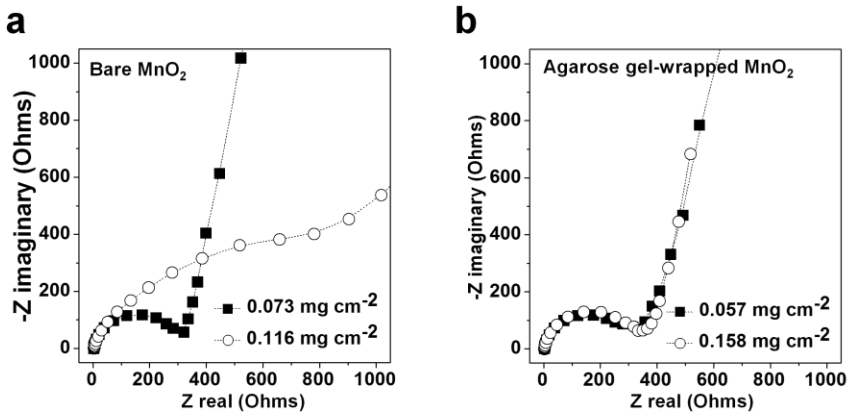

Figure 5-12. Nyquist impedance plots for a bare MnO_2 electrode (a) and an agarose gel-wrapped MnO_2 electrode (b).

Chapter 6. Robust Energy Storage Platform with Foldability and Washability

6.1 Experimental

6.1.1 Preparation of graphit felt-based conducting network (GFCN) electrode

Four types of tapes were used to the construct GFCNs: polypropylene tape (Tapex Corporation), cellophane tape (3M), duct tape (Kumsung K&T), and Post-it® (3M). Graphite felt, purchased from CeTech Corporation (GF065), was ripped off by repetitive attachment/detachment of each tape until the resistances of the film reached their minimum values. The minimum resistance values for polypropylene tape, cellophane tape, duct tape and Post-it® are 0.11, 0.85, 1.16, 2.50 kΩ cm. After the lint-off the GFCNs, all of electrodes were roll-pressed and cut into desired size.

6.1.2 Assembly of a full-cell system

The GFCN electrode for the assembled system is made with polypropylene tape. As a solid electrolyte, a PVA-H_3PO_4 gel electrolyte was prepared by mixing 5 g of polyvinyl alcohol (PVA) powder and 50 ml of deionized (DI) water, and 2.4 ml of phosphoric acid. The mixture was heated in 85 °C with vigorous stirring. After the complete dissolution of the PVA powder, the

solution was cast onto the 2 GFCN electrodes cooled down and dried for about 12 h under ambient conditions. After attaching the 2 gel electrolyte-coated GFCN electrodes, the completely constructed system was thoroughly sealed by using the sticky area of the polypropylene tape. The electrochemical folding-unfolding tests were conducted using a home-built linear stage instrument which was manually operated. To test the electrochemical stability after washing, I sewed the GFCN system on a lab coat. Then the GFCN system on lab coat was washed by washing machine (TROMM, Samsung) with the addition of detergent (Echoclean) and completely dried overnight at room temperature.

6.1.3 Oxidation of graphite felt

Oxidation of the graphite felt was performed by modifying the improved Hummer's method, as reported in the literature [199]. A sheet of graphite felt (15 cm × 15 cm × 0.65 cm, 9.79 g) and $KMnO_4$ (9 g, Sigma Aldrich) were mixed together and then immersed in a 9:1 mixture of concentrated H_2SO_4/H_3PO_4 (180 ml, Sigma Aldrich, 95 %/20 ml, Sigma Aldrich, 85 %). The mixture was maintained at 50 ℃ for 12 h, and then cooled to room temperature and poured onto ice (200 ml) with H_2O_2 (1.5 ml, Sigma Aldrich, 37 %). The oxidized sheet of graphite felt was repeatedly washed with excess amounts of DI water, HCl (Sigma Aldrich, 35 %), and ethanol under orbital shaking conditions. The sheet was completely dried overnight at 60 ℃.

6.1.4 Characterizations

The morphology of the graphite felt-tape complexes were characterized by scanning electron microscopy (SEM, Carl Zeiss, SUPRA 55VP). The X-ray diffraction (XRD) patterns were obtained in 20 ~ 80° using X-ray diffractometer (Rigaku, D-MAX2500-PC). For the electrochemical measurements, cyclic voltammetry (CV) and galvanostatic charge-discharge (CD) was performed by using electrochemical analyzing instrument (ZIVE SP2, Wonatech). For the half-cell test in a standard three-electrode configuration, I used a saturated Ag/AgCl as the reference electrode and a platinum counter electrode with an aqueous 1.0 M Na_2SO_4 as electrolyte. Conductivity test for GFCN electrodes with different types of tapes were performed potentiostatically (0.1 V), the resulting current is measured to calculate resistance of GFCN sheets.

6.1.5 Calculations

For the three-electrode cell test, the specific capacitance (F cm^{-2}) was calculated from cyclic voltammograms using the following equation [90, 178, 107]:

$$C = \frac{In_{CV}}{v \times \Delta V \times A}$$

where, In_{cv} is the area of integral for the discharged CV curve (AV), v is the sweep rate (V s^{-1}), ΔV is the potential window (V) and A is the area of electrode film (cm^{-2}).

For the two-electrode system, the specific capacitance (F cm^{-2}) was calculated from the cyclic voltammograms according to the following equation [200, 201]:

$$C = \frac{4 \times In_{CV}}{v \times \Delta V \times A}$$

where, A is the total area of the two electrodes (cm^2).

The energy density W, (Wh cm^{-2}) at certain scan rate v (V s^{-1}) was calculated based on following equation [202]:

$$E = \frac{1}{2} \times C \times \Delta V^2$$

where the C is the value of specific capacitance (F cm^{-2}).

And the power density P (W cm^{-2}) was obtained using the following equation [202]:

$$P = \frac{E}{t}$$

where the E is the value of energy density (Wh cm^{-2}).

6.2 Results and discussion

6.2.1 Selection of optimal adhesive substrate

A variety of commercially available adhesive tapes were exploited to fabricate GFCN with the objective of finding an ideal material for use in the 'lint taping' method. Polypropylene (PP) tape, cellophane tape, duct tape, and 3M Post it® were selected as candidates for fabricating the GFCNs. A sheet of graphite felt was torn off by the repetitive attachment/detachment of each tape until the conductance of the GFCN on each tape reached its upper limits. As illustrated in Figure 6-1(a), graphite felt is composed of a network of carbon fibers and magnified scanning electron microscopy (SEM) images (Figure 6-1(a) inset) indicate that a single fiber has a radius of ~8.75 μm and very high aspect ratio. The X-ray diffraction (XRD) pattern (Figure 6-1(b)) for the GFCN film displays sharp diffraction peak corresponding to the (002) plane of graphitic carbon (JCPDS card no. 25-0284).

The electrochemical property and performance of each GFCN were evaluated by means of cyclic voltammetry (CV) measurement in a potential window from 0 to 0.8 V. CVs were performed using a three-electrode system in 1 M Na_2SO_4 aqueous electrolyte and all GFCNs used in the test were identical in size and shape (rectangular 5 cm long by 1 cm wide). Figure 6-2 shows a series of photographs of the GFCN electrode based on each tape and the corresponding CV results at scan rates of 10, 100, 1000 mV s^{-1}. In case of PP and cellophane

tape, CV curves of GFCN showed a symmetrical and rectangular shape, indicative of excellent and ideal capacitance properties, even at a high scan rate of 1000 mV s^{-1} (Figure 6-2(a) and (b)). These results suggest that the formation of an electrical double layer is unimpeded due to the excellent conductivity of the GFCN formed on two tapes. On the other hand, CV curves of the GFCN on the duct tape and 3M Post it® show a relatively high resistive behavior (Figure 6-2(c) and (d)).

The reasons for the discrepancy in electrochemical properties can be explained by the different states of the GFCNs on the adhesive tapes. The repetitive applications of adhesive tape gradually peel off the graphite felt, resulting in an increase in the amount of stripped fiber that accumulates. In this situation, the adhesive strength and uniformity of the adhesive layer determine the packing state of the GFCNs on the tapes. The weight, thickness, packing density and sheet conductance of prepared GFCN layers on 4 types of adhesive tape are summarized in Table 6-1.

According to standard percolation theory, the density dependence of the conductivity is given by [203]

$$G \propto (N - N_C)^{\alpha}$$

Here, G indicates the sheet conductance in two dimensions, N is the number of conducting fibers per unit area, and N_c is the critical number corresponding to the percolation threshold. In equation (1), the number of conducting fibers, N, can be substituted for the density (ρ) of it. If I assume that the density of a

graphite fiber is much higher than the critical density of the percolation threshold, above equation can be reduced to:

$$G = k(\rho)^{\alpha}$$

where ρ is the density of graphite fiber on tape (g cm^{-3}), and k is a correction factor for fitting the experimental data. The critical exponent α depends only on the dimensionality of the space; for a film in two dimensions, the theoretical value of α is 1.33 [204].

Figure 6-3(a) shows the sheet conductance of GFCNs on 4 tapes as a function of the fiber density of the GFCN films. A fit of equation (2) to our data is shown as a red dashed line. Precise correlation between experimentally measured value and fitting based on theoretical calculations verifies that the packing density of the graphite fiber is a critical factor in determining both long-range electrical connectivity and the capacitive behavior of the GFCN on tape. In this regard, the PP tape was expected to show the most outstanding performance in the construction of a GFCN film. Figure 6-3(b) provides information on the specific capacitance (μF cm^{-2}) of GFCNs at various scan rates ranging from 10 mV s^{-1} to 2500 mV s^{-1}. The specific capacitance was quantified by integrating the CV curves in Figure 6-2 and details of the calculation method are presented in the supporting information. The GFCN electrode on PP tape showed a much higher specific capacitance (24.69 μF cm^{-2} at a scan rate of 10 mV s^{-1}) than the other electrodes (8.39 μF cm^{-2} for cellophane tape, 5.68 μF cm^{-2} for duct tape, 5.35 μF cm^{-2} for 3M Post-it® at identical scan rate condition). For the

quantitative comparison of rate capabilities, I derived the capacitance retention which is a ratio of two capacitance values obtained at a scan rate of 10 mV s^{-1} and 2500 mV s^{-1}. The calculated capacitance retention values of GFCN on PP, cellophane, duct, and Post-it® tapes were 0.43, 0.26, 0.08 and 0.02, respectively, which indicates the superior rate capability of the GFCN on the PP tape. In a Ragone plot, the GFCN on the PP tape also exhibited the most decent performance from the standpoint of both energy and power densities (Figure 6-4).

6.2.2 Assembly of full-cell

In order to realize a wearable supercapacitor system, the GFCN electrode based on the PP tape was introduced as a positive/negative electrode. For the fabrication of the full-cell with GFCN on PP tape, a graphite fiber was attached to the desired area of the PP tape. Attachment of the fiber to the selected area is simply achieved by applying a removable mask to the PP tape before peeling off the graphite felt (Figure 6-5). In the present research, I fabricated a GFCN film on PP tape with a 4 cm×4 cm rectangular shape with a protruding area (1 cm×2 cm) for connection to an external circuit. The uniform distribution and long-range electrical connectivity of GFCN on the PP tape was confirmed by resistance mapping (Figure 6-6). The final system was symmetrically organized in the GFCN-polymer electrolyte-GFCN configuration as illustrated in Figure 6-7(a). Polyvinyl alcohol (PVA)-based proton conducting polymer electrolytes were prepared by the solution cast technique. Added phosphoric acid has dual

roles as a proton supplier and as a plasticizer. The prepared PVA-H_3PO_4 electrolyte system exhibits good film-forming abilities and high mechanical strengths as previously reported [205]. The cross-sectional SEM image and energy dispersive spectroscopy (EDS) result (Figure 6-7(b)) confirm that three-layered film (polymer electrolyte-GFCN-tape) clearly secures its structural integrity.

6.2.3 Electrochemical measurements

The electrochemical test of the all-solid-state GFCN system was performed in two electrode set-up under both potentiostatic and galvanostatic conditions. All measurements were conducted in the potential window of 0 to 0.8 V at room temperature.

The CV curves for the GFCN system at various scan rates (1, 5, 10 mV s^{-1}) are summarized in Figure 6-7(c). Together with the proper incorporation of electrolyte into the porous GFCN, the system showed good capacitance properties. The symmetrical charge and discharge in CV curves were continuously maintained in the fast charge-discharge rate condition until the scan rate reached 1 V s^{-1} (Figure 6-8). These results are in good agreement with galvanostatic charge-discharge measurements (Figure 6-7(d)). Therefore, it can be concluded that the GFCN system retains its capacitive behavior even under conditions of fast operation, which can be attributed to both the high electrical and ionic conductivity of the GFCN/PVA-H_3PO_4 system.

The GFCN system showed a capacitance value of 25.24 μF cm^{-2}, 20.54 μF cm^{-2}, 17.80 μF cm^{-2} at a scan rate of 1 mV s^{-1}, 5 mV s^{-1}, 10 mV s^{-1}, respectively. Understandably, the specific capacitance value decreased with increasing charge-discharge speed (Figure 6-7(e)). Nevertheless, the all-solid-state GFCN system exhibited a decent rate performance without a noticeable drop of discharge/charge energy ratio (Figure 6-7(c)). In addition, no evidence of capacitance fading was found for the system after 5000 charge/discharge cycles, because the level of internal resistance of the overall system is kept low (Figure 6-9). Indeed, the low internal resistance of system is an important requirement under mechanically stressed conditions such as folding and washing.

6.2.4 Folding tests

In order to verify that the electrochemical performance of the GFCN system is maintained under severe mechanical deformations, a home-built folding instrument was used for making in-situ measurements during a test that involved repeated folding-unfolding. For the purpose of simulating the severe folding situation, the GFCN system with size of 4 cm×4 cm was gradually folded, and completely folded at the end (Pictures #1~#5 in Figure 6-10(a)). The bending radius (r_o) of each folding unit decreases to 0.29 mm at which point, the wearable system is completely folded (Figure 6-11).

The CV curves of the GFCN system measured in various folded states are displayed in Figure 6-10(b). The curves (potential versus current) in the folded states follow almost the same track as that under no mechanical deformation.

These data confirm that the morphological/electrical connectivity of GFCN is maintained and the electrochemical reactions that occurred in the system remain preserved under conditions of severe mechanical deformations (Figure 6-12).

Although some studies have reported on the development of flexible supercapacitor systems in a full-cell configuration, most of the resulting products were tested under moderate bending/folding conditions [109-111, 90, 127, 206]. On the other hand, our system can sustain its electrochemical and mechanical properties without the need for a binder or flexible current collector. Moreover, reverse-switching in the folding direction and the generation of a folding plane by additional folding had negligible effects on the performance of system (Pictures #6 and #7 in Figure 6-10(a) and corresponding CV curves in Figure 6-10(b)). This versatility on the foldable motif and unshrinking electrochemical performance are unique qualifications of the GFCN system as a wearable ESS, which has rarely been reported in previous research.

6.2.5 Washing tests

In the light of the current state of the art, I expect that the practically available, wearable ESS will arrive on market shelves in near future [207]. Integrated-cloth based system is the highly feasible form of a wearable ESS. In this expected situation, the washable characteristics of the system will become accepted as an important requirement of a wearable ESS. The concept of a washable system implies that the system does not permit one of two points to

occur, mainly water-degradable components and water leakage of the overall cell. Another requirement is superior tolerance to an imposed mechanical stress during washing such as crumpled states of clothing in a washing machine. Considering these essential prerequisites, the assembled GFCN system is capable of satisfying the above conditions. First of all, the PP tape not only plays a role as a water-proof support for GFCN but provides adhesive layer to seal overall system as well. Even if the water penetrates inside the system, there is no component which can be severely damaged by water. Secondly, the GFCN system exhibited a constant performance, even when in the completely folded state as mentioned above. Therefore, it can be concluded that the GFCN system is able to successfully operate after repeated washing cycles

To verify the washable nature of the GFCN system, a typical washing process was applied using a commercial washing machine with the addition of detergent. (See the Experimental Section for details of the process). Prior to the washing process, the GFCN system was integrated with a lab coat by sewing (Figure 6-13(a)). The CV curves in Figure 6-13(b) represent the electrochemical performance of the GFCN system before and after washing process. After the 1st washing cycle, the GFCN system retained 83 % of the original capacitance. The moderate decrease of capacitance that occurred during washing was attributed to the slight shape distortion of the box-like CV curve, indicating an increase in overall resistance. As mentioned, the GFCN system was designed so as to have a protruding area on both sides for the ease of connection to an external circuit. During the washing process, this area was directly exposed to water and detergent, and some slightly bound graphite felt

was removed and the network on the PP tape was rearranged. Thus, the decrease in capacitance after washing can be mainly attributed to resistive behavior occurring at the connecting part between the cell and the current collecting circuit. Consequently, the phenomenon would not be expected to occur repeatedly, since further capacitance fading was not observed after additional washing cycles (the GFCN system after the 2nd washing also showed a capacitance retention of 83 %).

6.2.6 Improvement of capacitance *via* surface treatments

The high electrical characteristic of graphitic fiber in organizing the GFCN provides important advantages for high power (~1.97 μW cm^{-2}), but there is a drawback related to the relatively low specific energy (~2.2 nW cm^{-2}) as shown in Figure 6-12(c). Apparently, a very important but also very challenging issue to address is how to greatly increase the energy density in the supercapacitor field. Double layer capacitance C can be expressed by following equation [56]:

$$C = \frac{(\varepsilon_r \varepsilon_0 A)}{d}$$

where ε_r is the electrolyte dielectric constant, ε_o is the dielectric constant of the vacuum, A is the electrode surface area and d is the effective thickness of the double layer. In this equation, d and A are changeable characteristics which are determined by the interfacial affinity between the electrolyte and electrode

[208]. The GFCN electrodes in the system have hydrophobic characteristics due to the surface of graphitic carbon, which makes it difficult to create a high electrolyte-electrode affinity. To obtain intimate contact between the graphitic electrode and the PVA-H_3PO_4 electrolyte, I imposed hydrophilic characteristics on the electrode by acid oxidation of the graphite felt. The abundance of oxygen containing groups on surface of graphitic fiber facilitated the wetting of the electrode with the PVA-H_3PO_4 electrolyte, which then increased the active surface area (A) accessible by electrolyte ions and reduced the charge separation distance (d) at the interface.

To demonstrate the enhanced capacitance of the GFCN system made of oxidized graphite felt (ox-GFCN), I compared the CV curves of both the GFCN and ox-GFCN systems at a scan rate of 1 mV s^{-1} (Figure 6-14(a)). As in the case of the GFCN, the CV curves of the ox-GFCN system showed good capacitance properties. The quantified specific capacitance at 1 mV s^{-1} is 313 μF cm^{-2}, the value of which is an order of magnitude greater than that of the GFCN system measured at same conditions. This increase in capacitance was also verified by galvanostatic charge-discharge measurements (Figure 6-15). In addition, this value is comparable to that for various carbon based supercapacitors [83, 209-212]. The values for specific capacitance obtained at various scan rates are show in Figure 6-14(b). The ox-GFCN system showed a superior capacitance at the scan rate of ~50 mV s^{-1}. However, 95 % capacitance fading was observed for ox-GFCN, while the scan rate increased from 1 mV s^{-1} to 50 mV s^{-1}. Apparently, the oxidation of GFCN for increasing the capacitance is closely related to the rate capability of the GFCN system, indicating a trade-off relation

between surface wettability and conductivity of fibrous graphite (Figure 6-14(c)). Although a significant improvement in energy density was realized by oxidizing the GFCN electrode, this value for specific capacitance can be increased by further upgrades. For instance, the simple electrodeposition of pseudocapacitive manganese oxide on the prepared GFCN electrode can be a powerful strategy for a high performance of the overall system (Figure 6-16) [213]. In addition, assigning pseudocapacitance by heteroatom (e.g. nitrogen) doping [214] or the electrical/chemical deposition of a faradaic material (e.g. cobalt oxide [215], polyaniline [216]) on the prepared GFCN platform represent potential routes for achieving a higher performance.

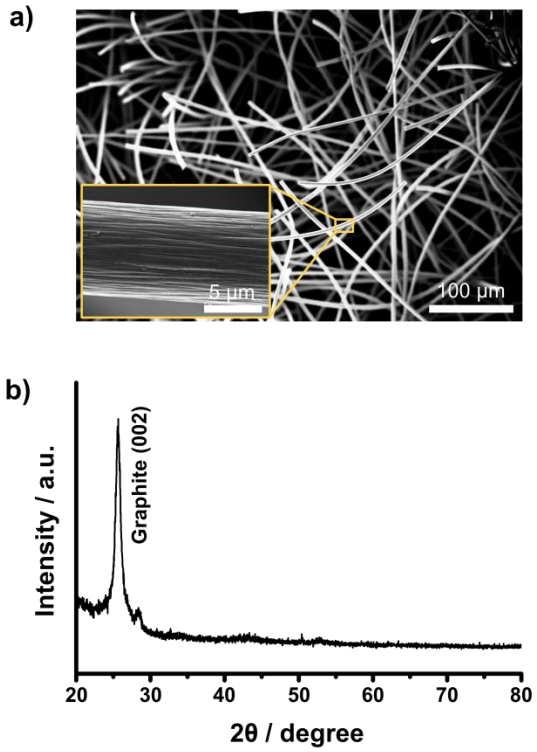

Figure 6-1. (a) SEM images of graphite felt and (b) XRD patterns of the film containing graphite felt.

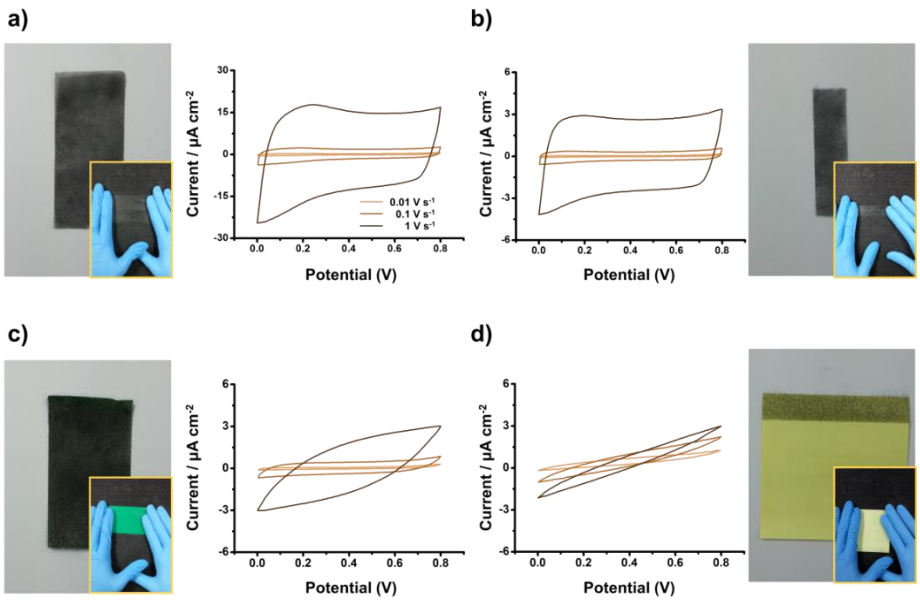

Figure 6-2. Fabrication process of graphite felt electrode by utilizing 4 types of adhesive substrate and corresponding CV curves at various scan rates. (a) Polypropylene tape, (b) Cellophane tape, (c) Duct tape, and (d) 3M Post it® .

Table 6-1. Weight, thickness, packing density and sheet conductance of prepared GFCN layers on 4 types of adhesive tapes.

Adhesive tape	Deposite weight	Thickness	Packing density	Sheet conductance
	mg cm^{-2}	μm	g cm^{-3}	$m\Omega^{-1}$ □
Polypropylene tape	1.98	20	0.99	5.3
Cellophane tape	1.47	50	0.29	1.5
Duct tape	2.65	100	0.27	1.1
3M Post-it®	1.25	130	0.097	0.75

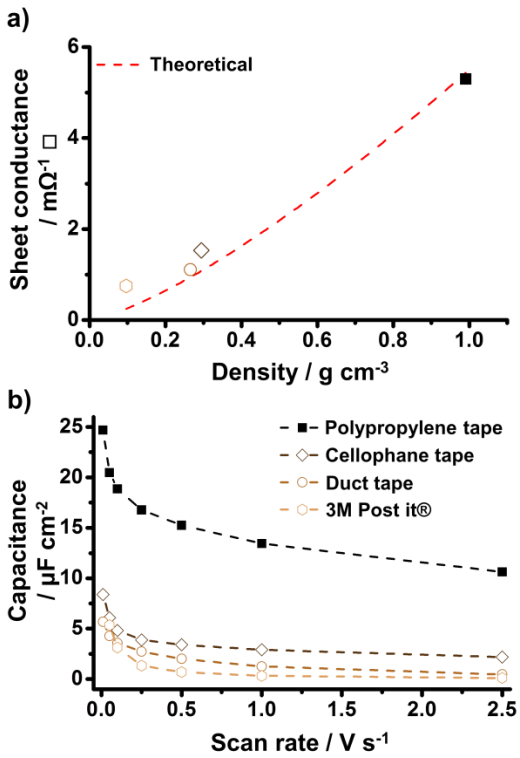

Figure 6-3. (a) Sheet conductance of graphite felt films as a function of GFCN film density. (b) Quantified specific capacitance at various scan rates from 10 mV s^{-1} to 2.5 V s^{-1}.

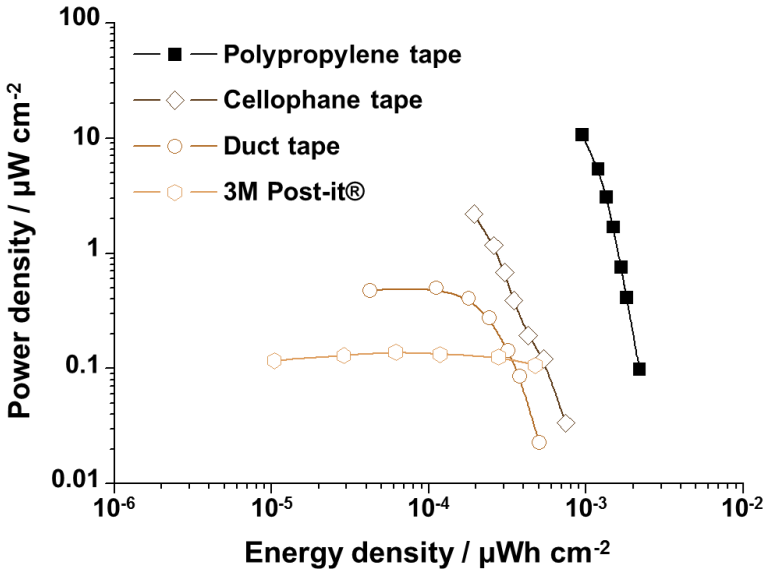

Figure 6-4. Ragone plot (power density against energy density) for the GFCN electrode constructed on various types of adhesive tape.

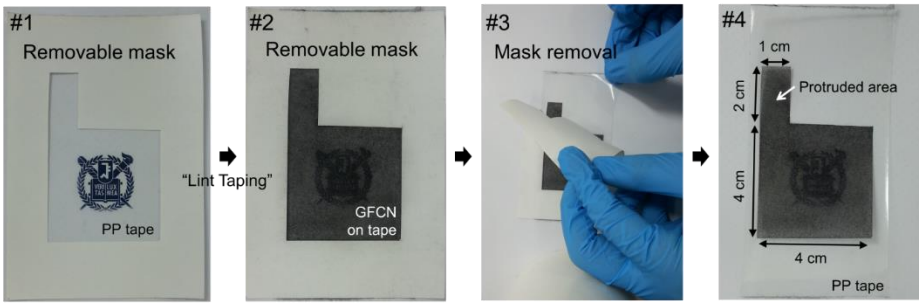

Figure 6-5. Fabrication procedure of a GFCN electrode for fully assembled supercapacitor system.

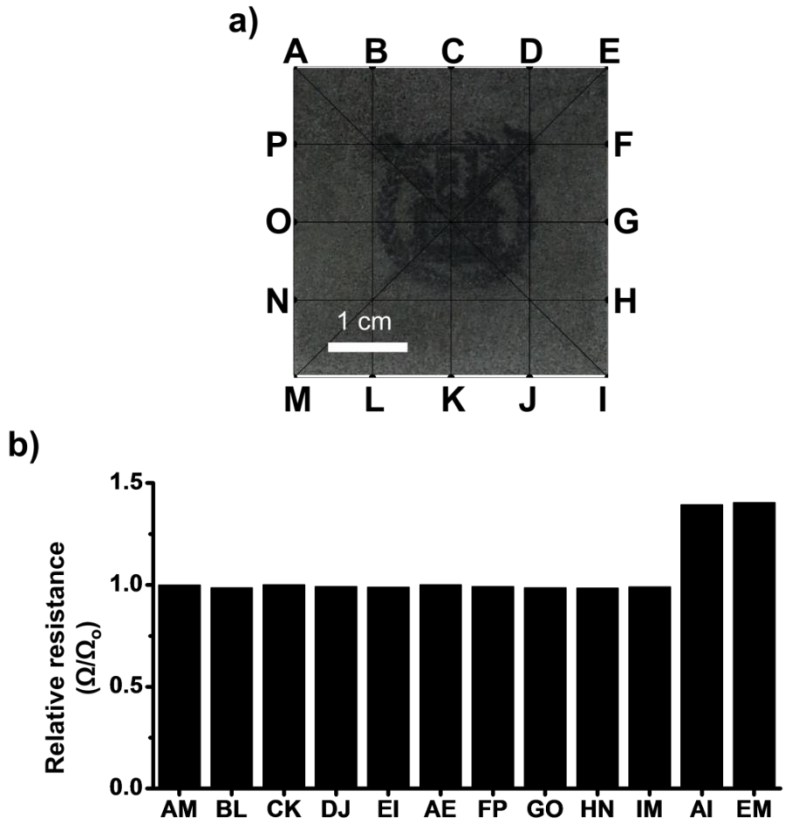

Figure 6-6. (a) Electrode placement configuration on the GFCN electrode for a two-probe resistance measurement. A~P indicates probe positioning. (b) Relative resistance at various probe positions. Ω_o is the resistance between A and M positions.

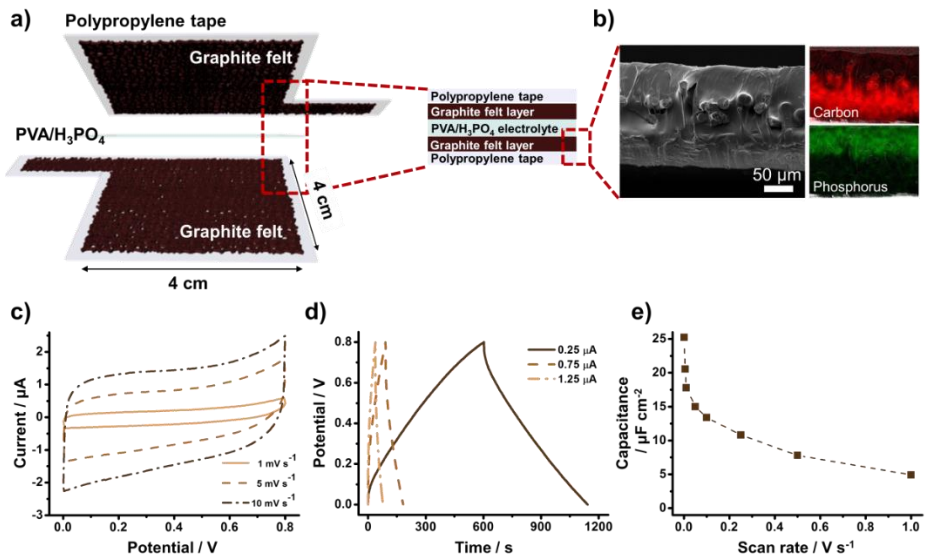

Figure 6-7. (a) Schematic illustration of wearable supercapacitor system. (b) SEM image of cross section for the electrode and EDS element mapping results. (c) CV curves of the system at three different scan rates (1 mV s^{-1}, 5 mV s^{-1}, 10 mV s^{-1}). (d) Galvanostatic charge/discharge curve at three different currents (0.25 µA, 0.75 µA, 1.25 µA) and (e) calculated specific capacitance as a function of scan rate.

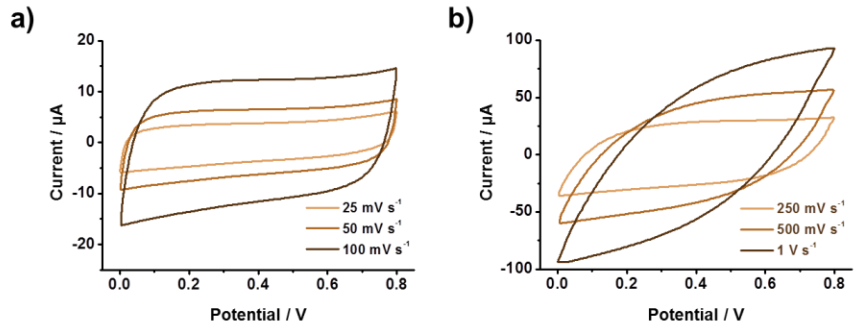

Figure 6-8. Cyclic voltammograms (CVs, current *versus* potential) for the GFCN full-cell at various scan rates up to 1 V s^{-1}. The symmetrical charge and discharge in CV curves were continuously maintained.

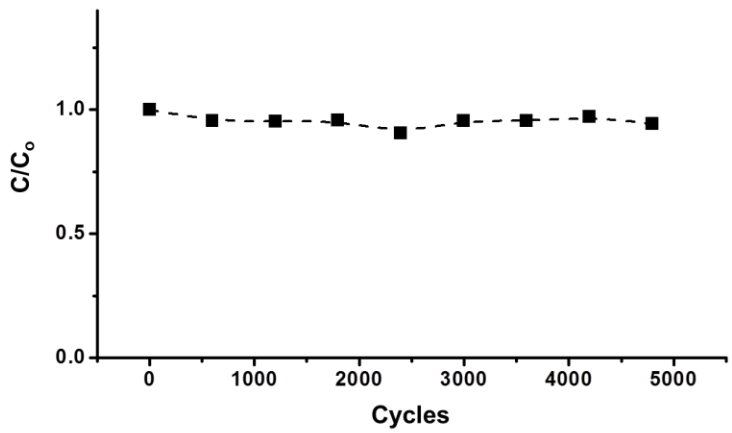

Figure 6-9. Relative capacitance as a function of charge-discharge cycles at a scan rate of 100 mV s^{-1}. C_o is the capacitance from the first cycle.

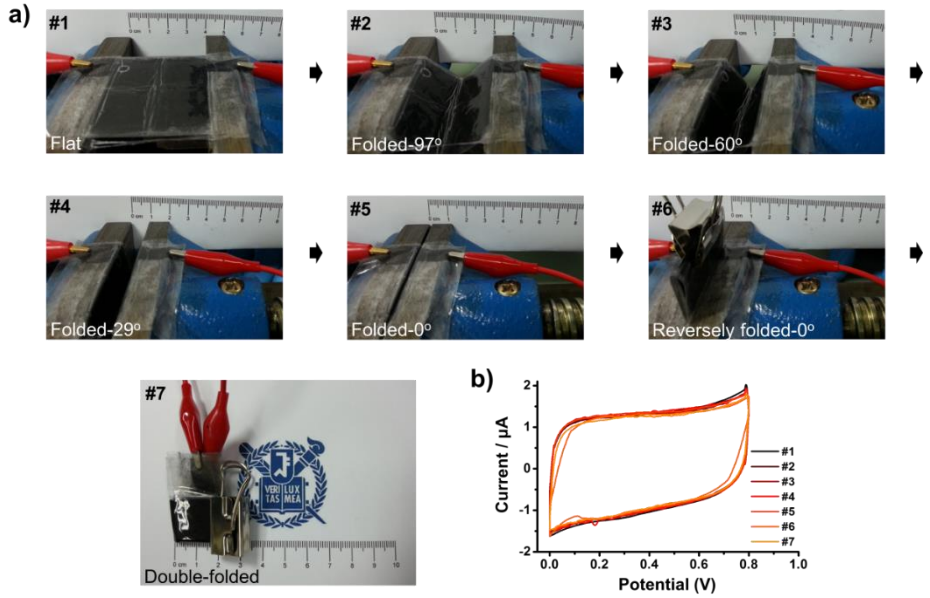

Figure 6-10. (a) Pictures of the system in various folding states. (b) Typical shapes of the CV curve were observed at scan rate of 10 mV s^{-1} for the different folding states of system.

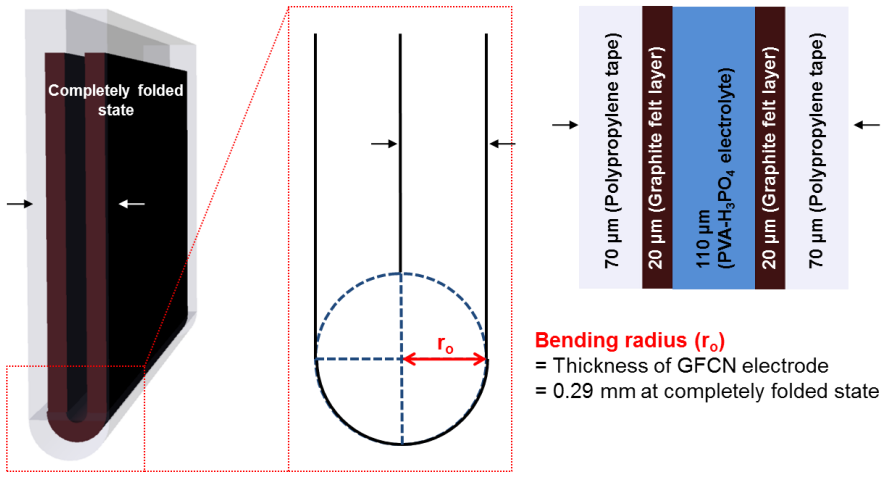

Figure 6-11. Determination of the minimum bending radius at completely folded state of GFCN full-cell.

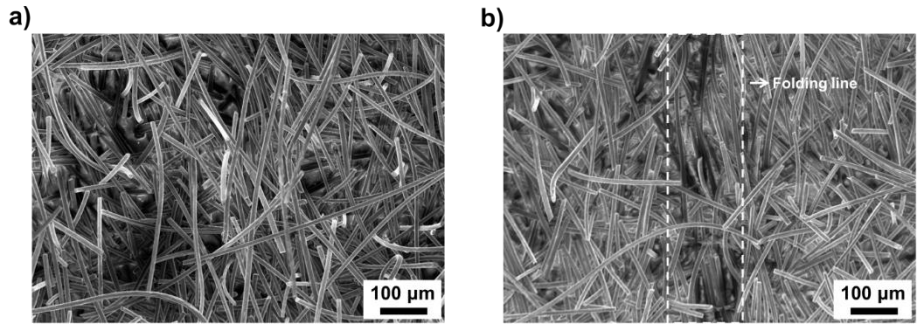

Figure 6-12. SEM images of a) pristine GFCN electrode and b) mechanically folded and unfolded GFCN electrode. No evidence of severe morphological disconnection was found for GFCN electrode after folding test.

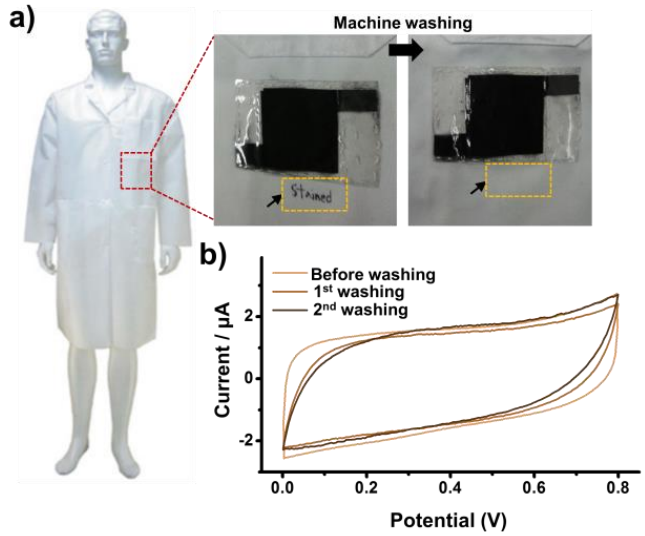

Figure 6-13. (a) Pictures of cloth integrated based device. (b) CV curves of device at scan rate of 10 mV s^{-1} after machine washing.

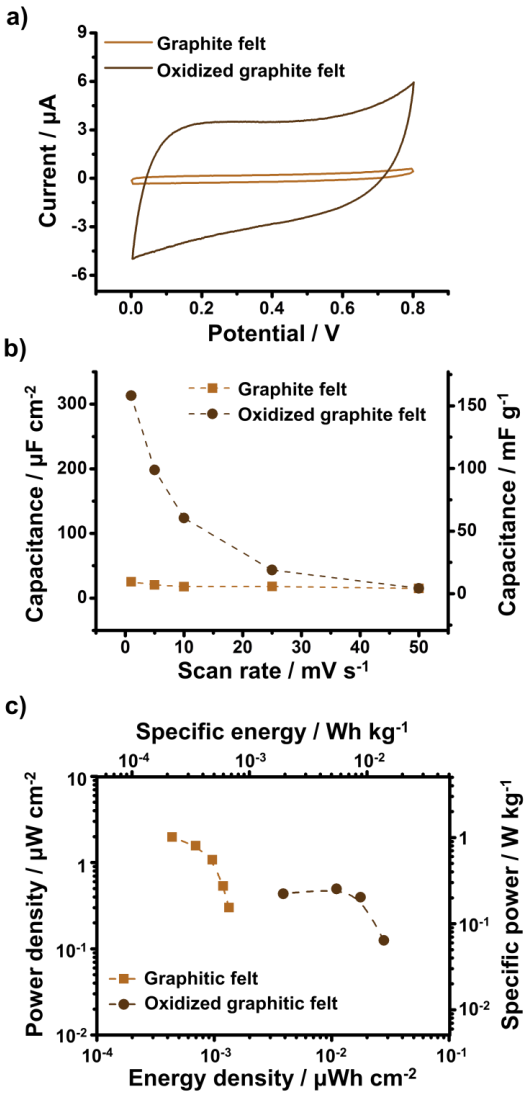

Figure 6-14. (a) CV curves at scan rate of 1 mV s^{-1} for assembled systems composed of graphitic felt and oxidized graphitic felt. (b) Specific capacitance (µF cm^{-2}, mF g^{-1}) as a function of scan rates (1 mV s^{-1} - 50 mV s^{-1}). (c) Ragone plot (power against energy) for assembled full-cell composed of graphitic felt (GFCN) and oxidized graphitic felt (ox-GFCN).

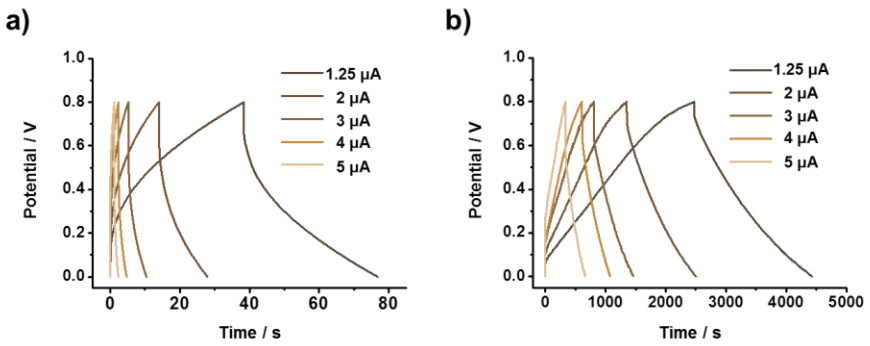

Figure 6-15. Charge-discharge curves (voltage *vs.* time) for assembled full-cell composed of (a) graphitic felt (GFCN) and (b) oxidized graphitic felt (ox-GFCN). The specific currents are 0.078, 0.125, 0.188, 0.25, 0.313 µA cm^{-2}. Each values of current applied to an assembled full-cell with size of 4 cm×4 cm.

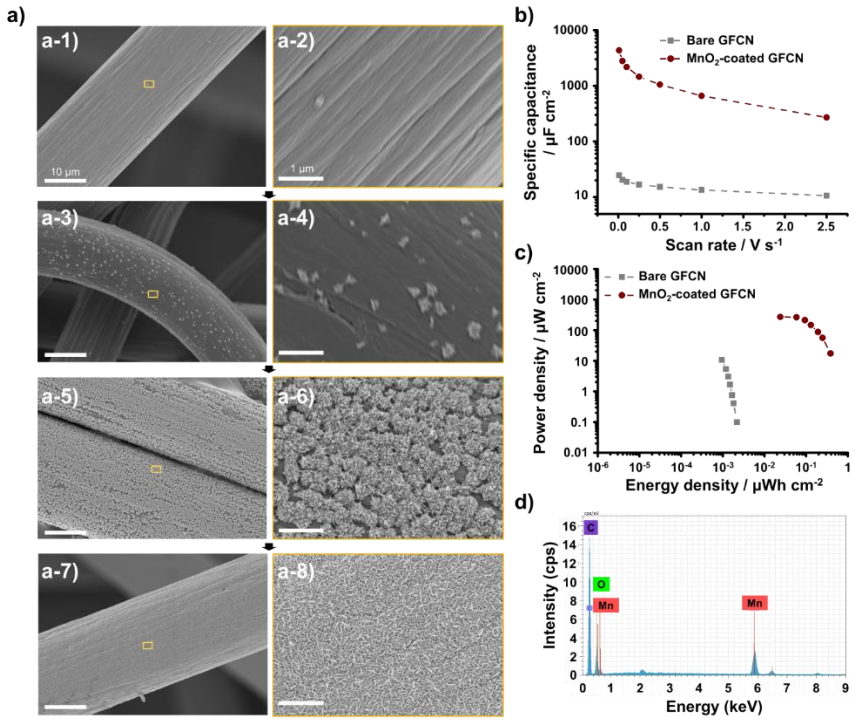

Figure 6-16. (a) SEM images of electro-deposited MnO_2. The MnO_2 was anodically (1.2 V) electro-deposited based on previous research [213]. As presented in images (a-1, 3, 5, 7) and the corresponding magnified images (a-2, 4, 6, 8), the hierarchical MnO_2 structure is gradually grown on the fibrous graphite. After the amount of MnO_2 deposited reached 0.096 mg cm^{-2} (a-7, 8 images), the MnO_2 film fully covered the surface of the fibrous graphite (MnO_2-coated GFCN). (b) Quantified specific capacitance of MnO_2-coated GFCN as a function of scan rate. Cyclic voltammetry was performed under the half-cell condition. (c) Ragone plot for the MnO_2-coated GFCN electrode constructed on polypropylene tape. (d) SEM-EDS data for the surface of MnO_2-coated GFCN.

Chapter 7. Summary and Conclusions

As one of the strategies for eliciting Li storage performance, the radial alignment of facile Li pathways inside three-dimensional TiO_2 was proposed in Chapter 2. Based on DFT calculations, it is concluded that [001] directionally over-grown TiO_2 rods provide a parallelepiped and prolonged *c*-channels which would be efficient pathways for Li^+ insertion and extraction. The desired TiO_2 rods were experimentally synthesized by the phase-selective growth of primary nanoparticles. The oil/water interfaces in a bicontinuous emulsion phase provided places for such TiO_2 growth and a tendency to reduce surface energy drove the assembly of TiO_2 rods with a spherical morphology. The use of radially organized TiO_2 rods (or c-channels) results in a greatly enhanced Li mobility inside the crystal, and consequently a reversible phase transformation was induced and maintained during repetitive charge-discharge cycles. Also, the spherical-shaped rods that were used in constituting the 3D-TS have advantages over the typical nano-sized TiO_2 with respect to both the close-packing of active materials and the decrease in intercrystalline resistance. The strategy used to prepare the 3D-TS reported herein has the important potential for use as a tailored approach to upgrading the related materials for Li storage.

As advanced high voltage anode materials, the nanostructured HTO particles and their fundamental Li diffusion dynamics were investigated in Chapter 3. The Li diffusion pathways and kinetics were investigated, which account for a significant portion in the electrochemical energy storage performance of HTO.

The close dependence of Li storage performance on Li diffusion within HTO crystals was elucidated by monitoring the charge/discharge profiles at various temperatures. Coupled with DFT calculations, two paths were proposed as feasible Li diffusion routes, which play major roles in the anisotropic (de)lithiation process of HTO. In addition, to shorten the distance of Li migration, a mc-HTO with the shape of a nano-bundle was synthesized utilizing a kinetic gap during the structural transformation of different phases of TiO_2. The mc-HTO exhibited a superior power performance compared to bulky HTO and commercial LTO. Thus, the HTO developed in this study represents the most competitive material currently available for the construction of safe LIB because its Li storage performance surpasses any other conventional high voltage anode material.

The development of an active carbon material and a 3D structured metallic current collector hybrid was described in Chapter 4, which highlights an ultrafast charge/dischargeable supercapacitor electrode. Clearly, the concept of realizing brain coral-like electrode has the following advantages. First, the large contact area and strong interfacial bond facilitate charge transfer between the active material and the current collector. Second, the ionic resistance of electrode materials without a complex pore structure is reduced. Furthermore, NH_3 activation is proven to be an excellent strategy for increasing the energy density of electrode materials without the loss of superior rate capability. It can be concluded that this concept is highly practical for use in applications in the field of power-demanding devices and ac line filtering.

A facile synthesis of a robust metal oxide thin film involving agarose gel-

mediated electrodeposition is presented in Chanpter 5. To prove the concept, an organic layer was introduced on the MnO_2 film by taking advantage of the inherent characteristics of agarose gels, including film-forming, ion-penetrable and elastic properties to achieve a high-performance pseudocapacitive electrode. The resulting electrode exhibited, not only an enhanced areal loading capacity, but a high utilization rate of MnO_2 as well. These improvements can be explained by a robust film structure and excellent contact with the metallic current collector. This study provides an effective route for organic-metal oxide hybridization by simply adding an agarose gel dip-coating procedure prior to the electrodeposition process.

The fabrication of an all-solid-state, foldable and washable supercapacitor system using simple 'lint taping' method were proposed in Chapter 6. Clearly, our concept has the following advantages. First, the superior electrical conductivity and connectivity of GFCN facilitates the long-range electron transfer between the electrode surface and the external circuit. Second, the self-adhering architecture provided by the tape not only forms a free-standing GFCN film but electrochemical activity is retained under harsh mechanical and washing conditions. Furthermore, surface oxidation was shown to be an excellent strategy for increasing the energy density of GFCN electrodes and the overall system. I expect that GFCN-based supercapacitor system developed in this study represent a promising ESS candidate for the future wearable electronics.

Chapter 8. Recommendations for Further Research

The recommendations for further research are summarized as follows;

1) The Li diffusion dynamics and electrochemical properties of $H_2Ti_{12}O_{25}$ are intensively studied in this dissertation. Although its improved potential flatness and capacity, the possibility of hydrogen gas evolution should be considered seriously before the practical application of $H_2Ti_{12}O_{25}$. As discussed in Chapter 3, the Li^+ ions substitute pre-existing H^+ ions of $H_2Ti_{12}O_{25}$ during the first lithiation (charging) process, results in hydrogen evolution reactions. Therfore, it is necessary to evaluate the fate of H^+ ions released from $H_2Ti_{12}O_{25}$. If the evolution of H_2 gas is to occur, the kinetics of hydrogen evolution and the strategy for managing the generated gas should be investigated.
2) The high electrical and mechanical characteristics of the GFCN electrode provide important advantages for achieving flexibility, foldability, and stretchability of supercapacitor system. However, the relatively low specific energy is critical drawback for the application of such system. Although, a significant improvement in energy density was realized in this dissertation, I believe that the value for energy density can be increased by further upgrades. Furthermore, some electrode materials and solid-type electrolytes with Li electroactivities are provided, the realization of wearable LIB system based on GFCN electrode would be possible [217, 218].

Bibliography

[1] J. –M. Tarascon, M. Armand, *Nature* **2001**, 414, 359.

[2] R. Bhattacharyya, B. Key, H. Chen, A. S. Best, A. F. Hollenkamp, C. P. Grey, *Nature Mater.* **2010**, 9, 504.

[3] F. Orsini, A. du Pasquier, B. Beaudouin, J. –M. Tarascon, M. Trentin, N. Langenhuizen, E. de Beer, P. Notten, *J. Power Sources* **1999**, 81-82, 918.

[4] D. W. Murphy, F. J. Disalvo, J. N. Carides, J. V. Waszczak, *Mat. Res. Bull.* **1978**, 13, 1395.

[5] M. Lazzari, B. Scrosati, *J. Electrochem. Soc.* **1980**, 127, 773.

[6] K. Mizushima, P. C. Jones, P. J. Wiseman, J. B. Goodenough, *Mat. Res. Bull.* **1980**, 15, 783.

[7] B. Scrosati, J. Hassoun, Y. –K. Sun, *Energy Environ. Sci.* **2011**, 4, 3287.

[8] P. G. Bruce, B. Scrosati, J. –M. Tarascon, *Angew. Chem. Int. Ed.* **2008**, 47, 2930.

[9] U. Kasavajjula, C. Wang, A. J. Appleby, *J. Power Sources* **2007**, 163, 1003.

[10] Y. Wang, G. Cao, *Adv. Mater.* **2008**, 20, 2251.

[11] L. Ji, Z. Lin, M. Alcoutlabi, X. Zhang, *Energy Environ. Sci.* **2011**, 4, 2682.

[12] R. Koksband, J. Barker, H. Shi. M. Y. Saidi, *Solid State Ionics* **1996**, 84, 1.

[13] A. Manthiram, *J. Phys. Chem. Lett.* **2011**, 2(3), 176.

[14] H. B. Wu, J. S. Chen, H. H. hng, X. W. Lou, *Nanoscale* **2012**, 4, 2526.

[15] D. S. Su, R. Schogl, *ChemSusChem* **2010**, 3,136.

[16] M. M. Thackeray, C. Wolverton, E. D. Isaacs, *Energy Environ. Sci.* **2012**, 5, 7854.

[17] G. L. Soloveichik, *Annu. Rev. Chem. Biomol. Eng.* **2011**, 2, 503.

[18] B. Dunn, H. Kamath, J. –M. Tarascon, *Science*, **2011**, 334, 928.

[19] Z. Zeng, W. –I. Liang, H. –G. Liao, H. L. Xin, Y. –H. Chu, H. Zheng, *Nano Lett.* **2014**, 14, 1745.

[20] R. L. Sacci, N. J. Dudney, K. L. More, L. R. Parent, I. Arslan, N. D. Browning, R. R. Unocic, *Chem. Commun.* **2014**, 50, 2104.

[21] Z. Chen, Y. Qin, Y. Ren, W. Lu, C. Orendorff, E. P. Roth, K. Amine, *Energy Environ. Sci.* **2011**, 4, 4023.

[22] G. Gachot, S. Grugeon, M. Armand, S. Pilard, P. Guenot, J. –M. Tarascon, S. Laruelle, *J. Power Sources* **2008**, 178, 409.

[23] P. G. Balakrishnan, R. Ramesh, T. P. Kumar, *J. Power Sources* **2006**, 155, 401.

[24] Q. Wang, P. Ping, X. Zhao, G. Chu, J. Sun, C. Chen, *J. Power Sources* **2012**, 208, 210.

[25] T. Fröschl, U. Hörmann, P. Kubiak, G. Kučerová, M. Pfanzelt, C. K. Weiss, R. J. Behm, N. Hüsing, U. Kaiser, K. Landfester, M. Wohlfahrt-Mehrens, *Chem. Soc. Rev.* **2012**, 41, 5313.

[26] X. Sun, P. V. Radovanovic, B. Cui, *New J. Chem.* **2015**, 39, 38.

[27] Y. Ren, Z. Liu, F. Pourpoint, A. R. Armstrong, C. P. Grey, P. G. Bruce, *Angew. Chem.* **2012**, 124, 2206.

[28] S. Liu, H. Jia, L. Han, J. Wang, P. Gao, D. Xu, J. Yang, S. Che, *Adv. Mater.* **2012**, 24, 3201.

[29] A. G. Dylla, G. Henkelman, K. J. Stevenson, *Acc. Chem. Res.* **2013**, 46, 1104.

[30] S. M. Lukic, J. Cao, R. C. Bansal, F. Rodriguez, A. Emadi, *IEEE Trans. Ind. Electron.* **2008**, 55, 2258.

[31] T. Matsuo, Y. Gambe, Y. Sun, I. Honma, *Sci. Rep.* **2014**, 4, 6084.

[32] K. Somasundaram, E. Birgersson, A. S. Mujumdar, *Appl. Math. Comput.* **2012**, 219, 2231.

[33] N. Ogihara, T. Yasuda, Y. Kishida, T. Ohsuna, K. Miyamoto, N. Ohba, *Angew. Chem. Int. Ed.* **2014**, 53, 11467.

[34] N. S. Hudak, D. L. Huber, *ECS Trans.* **2011**, 33, 1.

[35] K. Kang, Y. S. Meng, J. Bréger, C. P. Grey, G. Ceder, *Science* **2006**, 311, 977.

[36] D. C. Sayle, J. A. Doig, S. C. Parker, G. W. Watson, T. X. T. Sayle, *Phys. Chem. Chem. Phys.* **2005**, 7, 16.

[37] B. J. Morgan, G. W. Watson, *Phys. Rev. B* **2010**, 82, 144119.

[38] C. L. Olson, J. Nelson, *J. Phys. Chem. B* **2006**, 110, 9995.

[39] S. Kerisit, K. M. Rosso, Z. Yang, J. Liu, *J. Phys. Chem. C* **2009**, 113, 20996.

[40] M. Wagemaker, D. Lützenkirchen-Hecht, P. Keil, A. A. van Well, R. Frahm, *Phys. B* **2003**, 336, 118.

[41] H. Yildirim, J. P. Greeley, S. K. R. S. Sankaranarayanan, *Phys. Chem. Chem. Phys.* **2012**, 14, 4565.

[42] H. Yildirim, J. P. Greeley, S. K. R. S. Sankaranarayanan, *J. Phys. Chem. C* **2011**, 115, 15661.

[43] M. L. Sushko, K. M. Rosso, J. Liu, *J. Phys. Chem. C* **2010**, 114, 20277.

[44] Y. –S. Hu, L. Kienle, Y. –G. Guo, J. Maier, *Adv. Mater.* **2006**, 18, 1421.

[45] Z. Sun, J. H. Kim, Y. Zhao, F. Bijarbooneh, V. Malgras, Y. Lee, Y. –M. Kang, S. X. Dou, *J. Am. Chem. Soc.* **2011**, 133, 19314.

[46] H. Qiao, Y. Wang, L. Xiao, L. Zhang, *Electrochem. Commun*. **2008**, 10, 1280.

[47] R. B. Khomane, *J. Colloid Interface Sci*. **2011**, 356, 369.

[48] H. Fei, M. Wei, *Electrochim. Acta* **2011**, 56, 6997.

[49] J. Akimoto, K. Chiba, N. Kijima, H. Hayakawa, S. Hayashi, Y. Gotoh, Y. Idemoto, *J. Electrochem. Soc*. **2011**, 158, A546.

[50] J. Akimoto, K. Kataoka, N. Kojima, S. Hayashi, Y. Gotoh, T. Sotokawa, Y. Kumashiro, *J. Power Sources* **2013**, 244, 679.

[51] M. V. Koudriachova, N. M. Harrison, S. W. de Leeuw, *Phys. Rev. Lett*. **2001**, 86, 1275.

[52] S. P. Ong, V. L. Chevrier, G. Hautier, A. Jain, C. Moore, S. Kim, X. Ma, G. Ceder, *Energy Environ. Sci*. **2011**, 4, 3680.

[53] M. S. Islam, C. A. J. Fisher, *Chem. Soc. Rev*. **2014**, 43, 185.

[54] B. Ziebarth, M. Klinsmann, T. Eckl, C. Elsässer, *Phys. Rev. B* **2014**, 89, 174301.

[55] K. Kang, D. Morgan, G. Ceder, *Phys. Rev. B* **2009**, 79, 014305.

[56] P. Simon, Y. Gogotsi, *Nature Mater*. **2008**, 7, 845.

[57] J. R. Miller, A. F. Burke, *Electrochem. Soc. Interface Spring* **2008**, 17, 53.

[58] J. P. Zheng, T. R. Jow, *J. Electrochem. Soc*. **1995**, 142, L6.

[59] P. Soudan, J. Gaudet, D. Guay, D. Belanger, P. Schulz, *Chem. Mater*. **2002**, 14, 1210.

[60] B. E. Conway, V. Birss, J. Wojotowicz, *J. Power, Sources* **1994**, 66, 1.

[61] P. A. Nelson, J. R. Owen, *J. Electrochem. Soc*. **2003**, 150, A1313.

[62] C. Lin, J. A. Ritter, B. N. Popov, *J. Electrochem. Soc*. **1998**, 145, 4097.

[63] N. L. Wu, S. Y. Wang, C. Y. Han, D. S. Wu, L. R. Shiue, *J. Power Sources* **2003**, 113, 173.

[64] N. L. Wu, *Mater. Chem. Phys.* **2002**, 75, 6.

[65] T. Brousse, D. Belanger, *Electrochem. Solid-State Lett.* **2003**, 6, A244.

[66] T. Brousse, M. Toupin, D. Belanger, *J. Electrochem. Soc.* **2004**, 151, A614.

[67] H. Y. Lee, J. B. Goodenough, *J. Solid State Chem.* **1999**, 144, 220.

[68] H. Y. Lee, V. Manivannan, J. B. Goodenough, *C. R. Acad. Sci., Ser. IIc: Chim.* **1999**, 2, 565.

[69] L. L. Zhang, X. S. Zhao, *Chem. Soc. Rev.* **2009**, 38, 2520.

[70] Y. Lv, F. Zhang, Y. Dou, Y. Zhai, J. Wang, H. Liu, Y. Xia, B. Tu, D. Zhao, *J. Mater. Chem.* **2012**, 22, 93.

[71] N. D. Kim, S. J. Kim, G. –P. Kim, I. Nam, H. J. Yun, P. Kim, J. Yi, *Electrochim. Acta* **2012**, 78, 340.

[72] N. D. Kim, W. Kim, J. B. Joo, S. Oh, P. Kim, Y. Kim, J. Yi, *J. Power Sources* **2008**, 180(1), 671.

[73] E. J. Lee, Y. J. Lee, J. K. Kim, M. Lee, J. Yi, J. R. Yoon, J. C. Song, I. K. Song, *Mater. Res. Bull.* **2015**, 70, 209.

[74] J. R. Miller, P. Simon, *Science* **2008**, 321, 651.

[75] Z. Yang, J. Zhang, M. C. W. Kintner-Meyer, X. Lu, D. Choi, J. P. Lemmon and J. Liu, *Chem. Rev.* **2011**, 111, 3577.

[76] P. L. Taberna, C. Portet and P. Simon, *Appl. Phys. A* **2006**, 82, 639.

[77] Q. Cheng, J. Tang, J. Ma, H. Zhang, N. Shinya and L.-C. Qin, *Carbon* **2011**, 49, 2917.

[78] C.-W. Huang, C.-H. Hsu, P.-L. Kuo, C.-T. Hsieh and H. Teng, *Carbon* **2011**, 49, 895.

[79] G. Zhao, J. Li, L. Jiang, H. Dong, X. Wang and W. Hu, *Chem. Sci*. **2012**, 3, 433.

[80] M. M. Shaijumon, F. S. Ou, L. Ci and P. M. Ajayan, *Chem. Commun*. **2008**, 20, 2373.

[81] Q. Cheng, J. Tang, J. Ma, H. Zhang, N. Shinya, L.-C. Qin, *Phys. Chem. Chem. Phys*. **2011**, 13, 17615.

[82] S. Boukhalfa, K. Evanoff, G. Yushin, *Energy Environ. Sci*. **2012**, 5, 6872.

[83] D. Pech, M. Brunet, H. Durou, P. Huang, V. Mochalin, Y. Gogotsi, P.-L. Taberna and P. Simon, *Nature Nanotechnol*. **2010**, 5, 651.

[84] J. R. Miller, R. A. Outlaw and B. C. Holloway, *Science* **2010**, 329, 1637.

[85] X. Lang, A. Hirata, T. Fujita and M. Chen, *Nature Nanotechnol*. **2011**, 6, 232.

[86] H. Zhang, X. Yu and P. V. Braun, *Nature Nanotechnol*. **2011**, 6, 277.

[87] A. L. Cohen, S. R. Smith, M. S. McCartney and J. Van Etten, *Mar. Ecol. Prog. Ser*. **2004**, 271, 147.

[88] W. Chaikittisilp, M. Hu, H. Wang, H.-S. Huang, T. Fujita, K. C.-W. Wu, L.-C. Chen, Y. Yamauchi and K. Ariga, *Chem. Commun*. **2012**, 48, 7259.

[89] C.-M. Chen, Q. Zhang, C.-H. Huang, X.-C. Zhao, B.-S. Zhang, Q.-Q. Kong, M.-Z. Wang, Y.-G. Yang, R. Cai and D. S. Su, *Chem. Commun*. **2012**, 48, 7149.

[90] I. Nam, S. Park, G. –P. Kim, J. Park, J. Yi, *Chem. Sci*. **2013**, 4, 1663.

[91] P. –C. Chen, G. Shen, S. Sukcharoenchoke, C. Zhou, *Appl. Phys. Lett*. **2009**, 94, 043113.

[92] Y. Yang, S. Jeong, L. Hu, H. Wu, S. W. Lee, Y. Cui, *Proc. Natl. Acad. Sci. U. S. A.* **2011**, 108, 13013.

[93] P. J. King, T. M. Higgins, S. De, N. Nicoloso, J. N. Coleman, *ACS Nano* **2012**, 6, 1732.

[94] S. W. Lee, B. M. Gallant, H. R. Byon, P. T. Hammond, Y. Shao-Horn, *Energy Environ. Sci.* **2011**, 4, 1972.

[95] H. Xia, M. O. Lai, L. Lu, *JOM* **2011**, 63, 54.

[96] W. Wei, X. Cui, W. Chen, D. G. Ivey, *Chem. Soc. Rev.* **2011**, 50, 1697.

[97] W. Wei, X. Cui, W. Chen, D. G. Ivey, *J. Phys. Chem. C* **2008**, 112, 15075.

[98] C. –C. Hu, T. –W. Tsou, *J. Power Sources* **2003**, 115, 179.

[99] M. Nakayama, T. Kanaya, R. Inoue, *Electrochem. Commun.* **2007**, 9, 1154.

[100] G. –P. Kim, I. Nam, N. D. Kim, J. Park, S. Park, J. Yi, *Electrochem. Commun.* **2012**, 22, 93.

[101] J. N. Broughton, M. J. Brett, *Electrochim. Acta* **2005**, 50, 4814.

[102] N. Nagarajan, H. Humadi, I. Zhitomirsky, *Electrochim. Acta* **2006**, 51, 3039.

[103] N. Pernodet, M. Maaloum, B. Tinland, *Electrophoresis* **1997**, 18, 55.

[104] V. Normand, D. L. Lootens, E. Amici, K. P. Plucknett, P. Aymard, *Biomacromolecules* **2000**, 1, 730.

[105] X. Shen, X. Chen, J. –H. Liu, X. –J. Huang, *J. Mater. Chem.* **2009**, 19, 7687.

[106] A. Pluen, P. A. Netti, R. K. Jain, D. A. Berk, *Biophys J.* **1999**, 77, 542.

[107] S. Park, I. Nam, G. –P. Kim, J. Park, N. D. Kim, Y. Kim, J. Yi, *Chem. Commun.* **2013**, 49, 1554.

[108] N. D. Kim, H. J. Yun, I. Nam, J. Yi, *J. Mater. Chem.* **2011**, 21, 15885

[109] C. Meng, C. Liu, L. Chen, C. Hu, S. Fan, *Nano Lett.* **2010**, 10, 4025.

[110] P. Chen, H. Chen, J. Qiu, C. Zhou, *Nano Res.* **2010**, 3, 594.

[111] I. Nam, G.-P. Kim, S. Park, J. W. Han, J. Yi, *Energy Environ. Sci.* **2014**, 7, 1095.

[112] J. Xue, Y. Zhao, H. Cheng, C. Hu, Y. Hu, Y. Meng, H. Shao, Z. Zhang, L. Qu, *Phys. Chem. Chem. Phys.* **2013**, 15, 8042.

[113] L. Hu, M. Pasta, F. L. Mantia, L. Cui, S. Jeong, H. D. Deshazer, J. W. Choi, S. M. Han, Y. Cui, *Nano Lett.* **2010**, 10, 708.

[114] T. Chen, H. Peng, M. Durstock, L. Dai, *Sci. Rep.* **2014**, 4, 3612.

[115] Y.–H. Lee, J.–S. Kim, J. Noh, I. Lee, H. J. Kim, S. Choi, J. Seo, S. Jeon, T.–S. Kim, J.–Y. Lee, J. W. Choi, *Nano Lett.* **2013**, 13, 5753.

[116] P. J. King, T. M. Higgins, S. De, N. Nicoloso, J. N. Coleman, *ACS Nano* **2012**, 6, 1732.

[117] I. Balberg, C. H. Anderson, S. Alexander, N. Wagner, *Phys. Rev. B* **1984**, *30*, 3933.

[118] M. F. Yu, O. Lourie, M. J. Dyer, K. Moloni, T. F. Kelly, R. S. Ruoff, *Science* **2000**, 287, 637.

[119] V. Krstic, G. S. Duesberg, J. Muster, M. Burghard, S. Roth, *Chem. Mater.* **1998**, 10, 2338.

[120] D. Zhang, K. Ryu, X. Liu, E. Polikarpov, J. Ly, M. E. Tompson, C. Zhou, *Nano Lett.* **2006**, 6, 1880.

[121] R. Duggal, F. Hussain, M. Pasquali, *Adv. Mater.* **2006**, 18, 29.

[122] S. Maruyama, E. Einarsson, Y. Murakami, T. Edamura, *Chem. Phys. Lett.* **2005**, 403, 320.

[123] Z. Cao, B. Q. Wei, *Energy Environ. Sci.* **2013**, 6, 3183.

[124] H. Pan, J. Li, Y. P. Feng, *Nanoscale Res. Lett.* **2010**, 5, 654.

[125] B. You, N. Li, H. Zhu, X. Zhu, J. Yang, *ChemSusChem* **2013**, 6, 474.

[126] J. K. Sprafke, S. D. Stranks, J. H. Warner, R. J. Nicholas, H. L. Anderson, *Angew. Chem. Int. Ed.* **2011**, 50, 2313.

[127] F. Liu, S. Song, D. Xue, H. Zhang, *Adv. Mater.* **2012**, 24, 1089.

[128] Y. He, W. Chen, X. Li, Z. Zhang, J. Fu, C. Zhao, E. Xie, *ACS Nano* **2013**, 7, 174.

[129] J. Du, L. Zhao, Y. Zeng, L. Zhang, F. Li, P. Liu, C. Liu, *Carbon* **2011**, 49, 1094.

[130] K. S. Novoselov, A. K. Geim, S. V. Morozov, D. Jiang, Y. Zhang, S. V. Dubonos, I. V. Grigorieva, A. A. Firsov, *Science* **2004**, 306, 666.

[131] S. Zhong, C. Padeste, M. Kazacos, M. Skyllas-Kazacos, *J. Power Sources* **1993**, 45, 29.

[132] S. Tanaka, D. Nogami, N. Tsuda, Y. Miyake, *J. Colloid Interface Sci.* **2009**, 334, 188.

[133] G. Kresse, J. Furthmüller, *Phys. Rev. B* **1996**, 54, 11169.

[134] J. P. Perdew, K. Burke, M. Ernzerhof, *Phys. Rev. Lett.* **1996**, 77, 3865.

[135] P. E. Blöchl, *Phys. Rev. B* **1994**, 50, 17953.

[136] S. L. Dudarev, G. A. Botton, S. Y. Savrasov, C. J. Humphreys, A. P. Sutton, *Phys. Rev. B* **1998**, 57, 1505.

[137] B. J. Morgan, G. W. Watson, *Surf. Sci.* **2007**, 601, 5034.

[138] B. J. Morgan, G. W. Watson, *J. Phys. Chem. C* **2009**, 113, 7322.

[139] B. J. Morgan, D. O. Scanlon, G. W. Watson, *J. Mater. Chem.* **2009**, 19, 5175.

[140] B. J. Morgan, G. W. Watson, *J. Phys. Chem. C* **2010**, 114, 2321.

[141] G. Henkelman, B. P. Uberuaga, H. A. Jónsson, *J. Chem. Phys.* **2000**, 113, 9901.

[142] G. Henkelman, H. Jónsson, *J. Chem. Phys.* **2000**, 113, 9978.

[143] Y. S. Yun, K. R. Lee, H. Park, T. Y. Kim, D. Yun, J. Han, J. Yi, *ACS Catal.* **2015**, 5, 82.

[144] J. Kang, A. Hirata, L. Kang, X. Zhang, Y. Hou, L. Chen, C. Li, T. Fujita, K. Akagi, M. Chen, *Angew. Chem., Int. Ed.* **2013**, 52, 1664.

[145] J. Jung, M. Cho, M. Zhou, *AIP Adv.* **2014**, 4, 017104.

[146] F. Gligor, S. W. de Leeuw, *Solid State Ionics* **2006**, 177, 2741.

[147] Z. Shan, E. Gianotti, J. C. Jansen, J. A. Peters, L. Marchese, T. Maschmeyer, *Chem. - Eur. J.* **2001**, 7, 1437.

[148] T. –D. N. Phan, H. –D. Pham, T. V. Cuong, E. J. Kim, S. Kim, E. W. Shin, *J. Cryst. Growth* **2009**, 312, 79.

[149] A. Monnier, F. Schüth, Q. Huo, D. Kumar, D. Margolese, R. S. Maxwell, G. D. Stucky, M. Krishnamurty, P. Petroff, A. Firouzi, M. Janicke, B. F. Chmelka, *Science* **1993**, 261, 1299.

[150] K. S. W. Sing, D. H. Everett, R. A. W. Haul, L. Moscou, R. A. Pierotti, J. Rouquérol, T. Siemieniewska, *Pure Appl. Chem.* **1985**, 57, 603.

[151] H. Qiao, D. Tao, Y. Wang, Y. Cai, F. Huang, X. Yang, J. Wei, Q. Wei, *Chem. Phys. Lett.* **2010**, 490, 180.

[152] B. Liu, E. S. Aydil, *J. Am. Chem. Soc.* **2009**, 131, 3985.

[153] J. Lin, Y. –U. Heo, A. Nattestad, Z. Sun, L. Wang, J. H. Kim, S. X. Dou, *Sci. Rep.* **2014**, 4, 5769.

[154] Q. Huang, L. Gao, *Chem. Lett.* **2003**, 32, 638.

[155] D. Wang, D. Choi, J. Li, Z. Yang, Z. Nie, R. Kou, D. Hu, C. Wang, L. V. Saraf, J. Zhang, I. A. Aksay, J. Liu, *ACS Nano* **2009**, 3, 907.

[156] Z. Hong, M. Wei, T. Lan, G. Cao, *Nano Energy* **2012**, 1, 466.

[157] D. Dambournet, I. Belharouak, K. Amine, *Chem. Mater.* **2010**, 22, 1173.

[158] T. Ohzuku, Z. Takehara, S. Yoshizawa, *Electrochim. Acta*, 1979, 24, 219.

[159] W. J. Macklin, R. J. Neat, *Solid State Ionics* **1992**, 53-56, 694.

[160] Y. F. Zhukovskii, P. Balaya, E. A. Kotomin, J. Maier, *Phys. Rev. Lett.* **2006**, 96, 058302.

[161] C. Kim, R. Buonsanti, R. Yaylian, D. J. Milliron, J. Cabana, *Adv. Energy Mater.* **2013**, 3, 1286.

[162] W. J. H. Borghols, M. Wagemaker, U. Lafont, E. M. Kelder, F. M. Mulder, *Chem. Mater.* **2008**, 20, 2949.

[163] D. Wang, D. Choi, Z. Yang, V. V. Viswanathan, Z. Nie, C. Wang, Y. Song, J. –G. Zhang, J. Liu, *Chem. Mater.* **2008**, 20, 3435.

[164] E. Baudrin, S. Cassaignon, M. Koelsch, J. –P. Jolivet, L. Dupont, J. –M. Tarascon, *Electrochem. Commun.* **2007**, 9, 337.

[165] H. Qiao, Y. Wang, L. Xiao, L. Zhang, *Electrochem. Commun.* **2008**, 10, 1280.

[166] L. Xin, Y. Liu, B. Li, X. Zhou, H. Shen, W. Zhao, C. Liang, *Sci. Rep.* **2014**, 4, 4479.

[167] S. Kikkawa, F. Yasuda, M. Koizumi, *Mater. Res. Bull.* **1985**, 20, 1221.

[168] H. Izawa, S. Kikkawa, M. Koizumi, *J. Phys. Chem.* **1982**, 86, 5023.

[169] E. Morgado Jr, P. M. Jardim, B. A. Marinkovic, F. C. Rizzo, M. A. S. de Abreu, J. L. Zotin, A. S. Araújo, *Nanotechnology* **2007**, 18, 495710.

[170] A. Paolella, G. Bertoni, E. Dilena, S. Marras, A. Ansaldo, L. Manna, C. George, *Nano Lett.* **2014**, 14, 1477.

[171] F. Ning, S. Li, B. Xu, C. Ouyang, *Solid State Ionics* **2014**, 263, 46.

[172] K. Persson, V. A. Sethuraman, L. J. Hardwick, Y. Hinuma, Y. S. Meng, A. van der Ven, V. Srinivasan, R. Kostecki, G. Ceder, *J. Phys. Chem. Lett.* **2010**, 1, 1176.

[173] Q. Zhang, X. Li, *Int. J. Electrochem. Sci.* **2013**, 8, 6449.

[174] D. A. H. Hanaor, C. C. Sorrell, *J. Mater. Sci.* **2011**, 46, 855.

[175] J. Muscat, V. Swamy, N. M. Harrison, *Phys. Rev. B* **2002**, 65, 224112.

[176] D. C. Hurum, A. G. Agrios, K. A. Gray, *J. Phys. Chem. B* **2003**, 107, 4545.

[177] J. Baek, S. Park, C. K. Song, T. Y. Kim, I. Nam, J. M. Lee, J. W. Han, J. Yi, *Chem. Commun.* **2015**, 51, 15019.

[178] I. Nam, G. –P. Kim, S. Park, J. Park. N. D. Kim, J. Yi, *Nanoscale* **2012**, 4, 7350.

[179] R. Kötz, M. Carlen, *Electrochim. Acta* **2000**, 45, 2483.

[180] G. L. Drisko, X. Wang, R. A. Caruso, *Langmuir* **2011**, 27, 2124.

[181] D. Walsh, L. Arcelli, T. Ikoma, J. Tanaka, S. Mann, *Nature Mater.* **2003**, 2, 386.

[182] Y. Xue, S. Datta, *Phys. Rev. Lett.* **1999**, 83, 4844.

[183] J. Tersoff, *Appl. Phys. Lett.* **1999**, 74, 2122.

[184] G. Wang, L. Zhang, J. Zhang, *Chem. Soc. Rev.* **2012**, 41, 797.

[185] S. Bose, T. Kuila, A. K. Mishra, R. Rajasekar, N. H. Kim, J. H. Lee, *J. Mater. Chem.* **2012**, 22, 767.

[186] Y.-R. Nian, H. J. Teng, *Electroanal. Chem.* **2003**, 540, 119.

[187] Y. Honda, T. Haramoto, M. Takeshige, H. Shiozaki, T. Kitamura, M. Ishikawa, *Electrochem. Solid-State Lett.* **2007**, 10, A106.

[188] M. Yao, K. Okuno, T. Iwaki, M. Kato, S. Tanase, K. Emura, T. Sakai, *Electrochem. Solid-State Lett.* **2007**, 10, A245.

[189] C. Portet, P. L. Taberna, P. Simon, C. Laberty-Robert, *Electrochim. Acta* **2004**, 49, 905.

[190] D. W. Wang, F. Li, L.-C. Yin, X. Lu, Z.-G. Chen, I. R. Gentle, G. Q. Lu, H.-M. Cheng, *Chem. Eur. J.* **2012**, 18, 5345.

[191] D. Wei, Y. Liu, Y. Wang, H. Zhang, L. Huang, G. Yu, *Nano Lett.*, **2009**, 9, 1752.

[192] T. Fujii, T. Yano, H. Kumagai, O. Miyawaki, *Biosci. Biotechnol. Biochem.* **2000**, 64(8), 1618.

[193] S. Arnott, A. Fulmer, W. E. Scott, *J. Mol. Biol.*, **1974**, 90, 269.

[194] V. Normand, D. L. Lootens, E. Amici, K. P. Plucknett, P. Aymard, *Biomacromolecules* **2000**, 1, 730.

[195] S. Chou, F. Cheng, J. Chen, *J. Power Sources* **2006**, 162, 727.

[196] I. Nam, G. –P. Kim, S. Park, J. Park, N. D. Kim, J. Yi, *Nanoscale* **2012**, 4, 7350.

[197] C. –C. Hu, T. –W. Tsou, *Electrochem. Commun.* **2002**, 4, 105.

[198] S. –C. Pang, M. A. Anderson, T. W. Chapman, *J. Electrochem. Soc.* **2000**, 147, 444.

[199] D. C. Marcano, D. V. Kosynkin, J. M. Berlin, A. Sinitskii, Z. Sun, A. Slesarev, L. B. Alemany, W. Lu, J. M. Tour, *ACS Nano* **2010**, 4, 4806.

[200] J. Ji, L. L. Zhang, H. Ji, Y. Li, X. Zhao, X. Bai, X. Fan, F. Zhang, R. S. Ruoff, *ACS Nano* **2013**, 7, 6237.

[201] T. Kim, G. Jung, S. Yoo, K. S. Suh, R. S. Ruoff, *ACS Nano* **2013**, 7, 6899.

[202] C. Zhang, Z. Peng, J. Lin, Y. Zhu, G. Ruan, C. –C. Hwang, W. Lu, R. H. Hauge, J. M. Tour, *ACS Nano* **2013**, 7, 5151.

[203] L. Hu, D. S. Hecht, G. Grüner, *Nano Lett*. **2004**, 4, 2513.

[204] R. L. Blumberg, G. Shlifer, H. E. Stanley, *J. Phys. A: Math. Gen*. **1980**, 13, L147.

[205] M. Z. Kufian, S. R. Majid, A. K. Arof, *Ionics* **2007**, 13, 231.

[206] Y. Fu, X. Cai, H. Wu, Z. Lv, S. Hou, M. Peng, X. Yu, D. Zou, *Adv. Mater*. **2012**, 24, 5713.

[207] S. Y. Lee, K.–H. Choi, W.–S. Choi, Y. H. Kwon, H.–R. Jung, H.–C. Shin, J. Y. Kim, *Energy Environ. Sci*. **2013**, 6, 2414.

[208] T. Y. Kim, H. W. Lee, M. Stoller, D. R. Dreyer, C. W. Bielawski, R. S. Ruoff, K. S. Suh, *ACS Nano* **2011**, 5, 436.

[209] W. Chen, R. B. Rakhi, L. Hu, X. Xie, Y. Cui, H. N. Alshareef, *Nano Lett*. **2011**, *11*, 5165.

[210] D. Pech, M. Brunet, P.–L. Taberna, P. Simon, N. Fabre, F. Mesnilgrente, V. Conédéra, H. Durou, *J. Power Sources* **2010**, *195*, 1266.

[211] H. J. In, S. Kumar, Y. Shao-Horn, G. Barbastathis, *Appl. Phys. Lett*. **2006**, *88*, 083104.

[212] C.–H. Huang, Q. Zhang, T.–C. Chou, C.–M. Chen, D. S. Su, R.–A. Doong, *ChemSusChem*, **2012**, 5, 563.

[213] S. Park, I. Nam, G.–P. Kim, J. W. Han, J. Yi, *ACS Appl. Mater. Interfaces* **2013**, 5, 9908.

[214] G. Xu, B. Ding, P. Nie, L. Shen, J. Wang, X. Zhang, *Chem. Eur. J.* **2013**, 19, 12306.

[215] Y. J. Lee, J. C. Jung, S. Park, J. G. Seo, S.–H. Baeck, J. R. Yoon, J. Yi, I. K. Song, *Korean J. Chem. Eng.* **2011**, 28, 492.

[216] G. Xiong, C. Meng, R. G. Reifenberger, P. P. Irazoqui, T. S. Fisher, *Adv. Energy Mat.* **2014**, 4, 1300515.

[217] C. Wang, W. Wan, Y. Huang, J. Chen, H. H. Zhou, X. X. Zhang, *Nanoscale* **2014**, 6, 5351.

[218] G. K. Simon, B. Maruyama, M. F. Durstock, D. J. Burton, T. Goswami, *J. Power Sources* **2011**, 196, 10254.

국 문 초 록

최근 휴대용 전자기기와 리튬이온전지(lithium ion battery)의 사용이 증가하면서 안전성에 대한 우려가 증가하고 있다. 실제로 다양한 전자기기에서 사용되는 리튬이온전지의 폭발사고에 대한 소식을 자주 접할 수 있다. 리튬이온전지의 용도가 휴대폰, 노트북과 같은 소형 전자기기에서 전기자동차, 스마트그리드(smart grid) 등의 대형 에너지 저장 장치로 확대되면서 리튬이온전지의 불안정성이 초래할 수 있는 인적, 물적 자원의 손실에 대한 우려가 커지고 있는 상황이다. 이러한 상황에서 고안전성 리튬이온전지의 핵심 부품인 고전압 음극물질에 대한 관심이 증가하고 있다. 고전압 음극물질은 높은 작동전압 덕분에 리튬의 불균일한 도금(plating)을 방지할 수 있고 전해액 산화에 의한 부반응을 억제하는 원리로 리튬이온전지의 안전성/안정성을 크게 개선하는 것으로 알려져 있다. 대표적인 고전압 음극물질군으로서 다양한 산화 티타늄 기반의 무기결정체들(리튬티타늄화합물 ($Li_4Ti_5O_{12}$), 이산화티타늄(TiO_2)) 이 개발되어 왔지만 낮은 용량(capacity) 또는 약화된 전위평탄면(voltage plateau)으로 인해 산업적 응용에 어려움이 있다. 이 학위논문의 첫 부분에서는 이러한 단점을 극복하는 전기화학적 특성을 지닌 고전압 음극물질의 개발에 대하여 다루고 있다. 자세한 내용은 다음과 같다.

- 무기결정체 내에서 원활한 리튬의 삽입과 탈리는 고전압 음극물질의 리튬저장능력에 있어 매우 중요하다. 다양한 결정구조를 갖는 이산화티타늄 (TiO_2) 물질 중 루타일(rutile) 결정체 내의 c-채널이 리튬의 원활한 삽입과 탈리에 중요한 경로를 제공하는데 c-채널은 적층된 (001) 결정면에 수직으로 발달해 있다. 그러므로 (001) 결정면의 적층구조가 잘 발달된 루타일 이산화티타늄을 개발함으로써 리튬의 저장능력을 최대화할 수 있다. 이에 최적화된 형태로서 돌기형 c-채널 나노막대가 원형으로 배열된 이산화티타늄 나노구체를 제시하였다. 나노막대의 (001) 결정면이 과성장하는 이유는 합성과정에서의 염소이온(Cl^-)이 (110) 결정면에 선택적으로 흡착됨으로써 성장을 방해하기 때문으로 예상된다. 향상된 결정내부의 리튬 확산도 뿐만 아니라 나노막대가 구형의 형태로 조밀구조를 이루고 있기 때문에 낮은 전자전달 저항을 유도할 수 있었다. 이렇게 합성된 이산화티타늄 나노구체는 고전압 음극물질로서 100%의 쿨롱효율(Coulombic efficiency)을 나타내었고 300회 이상의 충방전 싸이클에서도 성능저하가 발견되지 않을 정도로 높은 안정성을 나타내었다.
- 또 다른 고전압 음극물질로서 수소화산화티타늄(hydrogenated titanium oxide, HTO)은 리튬티타늄화합물을 능가하는 높은 실용량 덕분에 최근 개발 된 이후로 주목을 받고 있다. 하지만 리튬의 거동

측면에서 수소화산화티타늄의 열역학적, 동역학적 특성은 밝혀져 있지 않은 상황이다. 따라서 이 논문에서는 이론적, 실험적 분석을 통해 수소화산화티타늄의 리튬의 저장능력을 평가하였다. 그 결과 리튬의 확산 속도가 특성이 수소화산화티타늄의 리튬의 저장능력에 중대한 영향을 미치는 것을 알아내었고, 수소화산화티타늄을 나노구조화 하여 리튬의 확산거리를 감소시킬 수 있다면 그 전기화학적 성능을 향상시킬 수 있다는 결론에 도달하게 되었다. 합성과정에서 이산화티타늄 전구체의 상변화 속도차이를 이용해 제조된 나노구조의 수소화산화티타늄은 벌크 수소화산화티타늄에 비해 크게 향상된 율속특성과 안정성을 보였다. 이렇게 제조된 나노구조의 수소화산화티타늄은 현재까지 개발된 고전압 음극소재 중에 가장 높은 용량을 나타내었다.

슈퍼커패시터라고도 불리는 전기화학 커패시터는 배터리와 커패시터의 중간 성능을 갖으며 높은 출력, 장수명 특성 덕분에 안전하고 안정적인 미래의 에너지 저장 시스템으로서 주목 받고 있다. 향후 높은 출력 특성과 더불어 에너지 밀도가 향상된다면 배터리와 함께 대표적인 에너지 저장시스템으로 활용될 수 있을 것으로 예상된다. 현재 슈퍼커패시터 기술의 한계점은 낮은 이온/전자 전도성과 전하 전달 저항에 의한 등가직렬저항(equivalent series resistance)의 증가에 있다. 또한

정전용량(capacitance)를 결정하는 표면적을 증가하기 위해 시행되고 있는 활성화 공법(activation process)이 유독한 화학물질, 금속물 처리를 통해 이루어 지기 때문에 가격경쟁력과 환경오염 측면에서 경쟁력 약화가 우려된다. 이 학위논문의 중간 부분에서는 이러한 기술적 한계점을 극복하는 슈퍼커패시터 전극제조에 대하여 다루고 있다. 자세한 내용은 다음과 같다.

- 슈퍼커패시터 전극 내 이온전도 및 집전체/활물질 사이에서 발생하는 전하전달 저항을 감소시키 위하여 뇌산호(brain coral) 모양과 유사한 금속-탄소 하이브리드 물질을 개발하였다. 제조된 물질은 1,000 V s^{-1} 의 빠른 충반전 조건에서도 잘 작동하였다. 합성을 위해서 아가로스 겔(agarose gel)을 활용하였고 겔 내에 위치한 기공 내에 금속선을 채워 탄화(carbonization) 시켰다. 내부의 기공을 금속선이 채우고 있기 때문에 이온 및 전자의 전달이 크게 향상되었다. 빠른 출력 특성 덕분에 에너지 저장 뿐만 아니라 교류전원의 필터링에도 사용 될 수 있다.
- 단위면적당 높은 정전용량 확보하기 위해서는 활물질을 제한된 면적 내에 집적화 시키는 것이 필요하다. 하지만 박막전극의 경우 지나치게 많은 활물질이 도포될 경우 구조적 붕괴 및 전기적 고립(electrical isolation)이 일어나 집적화에 한계가 있다. 이를 해결하기 위해 아가로스 겔이라는 고분자 탄성체를 필름 형태로 집전체 위에

코팅하고 전기증착법을 통해 활물질을 증착시켜 제한된 전극 면적 내에서 높은 정전용량(52.55 mF cm^{-2})을 확보할 수 있었다.

최근 스마트폰과 같은 휴대용 전자기기에 있어서 “웨어러블(wearable)” 특성을 부여하는 것은 장착될 에너지 저장 시스템의 개발에 달려있다고 해도 과언이 아니다. 그러므로 구부릴 수 있고(flexible), 접을 수 있고(foldable), 늘릴 수 있는(stretchable) 에너지 저장 시스템의 개발이 매우 중요해지고 있다. 이를 위해서는 물리적 변형에 견딜 수 있고 그 변형에도 전도성을 잃지 않을 수 있는 에너지 저장 플래폼이 필요한데 이 학위논문에서는 ‘lint taping’ 기법을 개발하여 흑연계 탄소 섬유를 필름형태로 제조하는데 성공하였다. 자세한 내용은 다음과 같다.

- 옷에서 보푸라기를 제거하기 위해 접착성 테이프를 활용하는 것에 영감을 얻어 흑연계 탄소 섬유 네트워크를 접착성 기판 위에 필름형태로 구성하였다. 제조된 탄소 필름은 고체 전해질과 함께 결합되어 슈퍼커패시터로서 전기화학적 특성을 분석하였다. 그 결과 접거나 세탁하는 등의 심각한 물리적 변형에도 그 전기화학적 특성을 유지하여 향후 웨어러블 전자기기에의 적용 가능성을 증명하였다.

주요어: 에너지 저장 시스템, 안전성, 안정성, 리튬이온전지, 슈퍼커패시터, 고전압 음극물질, 이산화티타늄, 수소화산화티타늄, 하이브리드 전극, 금속−탄소 이중연결구조, 이산화망간, 전고상, 웨어러블, 세탁가능
학 번: 2010-22811

List of publications

International Publications

International Peer-Reviewed Journals (First Author)

1. J. Baek*, **S. Park***, C. K. Song, T. Y. Kim, I. Nam, J. M. Lee, J. W. Han, and J. Yi, "Radial alignment of c-channel nanorods in 3D porous TiO_2 for eliciting enhanced Li storage performance", Chemical Communications, 51, 15019-15022 (2015)
   (* Soomin Park and Jayeon Baek contributed equally to this work.)
2. **S. Park**, Y. G. Yoo, I. Nam, S. Bae, and J. Yi, "All-Solid-State, Washable, Wearable Supercapacitors Fabricated by using a Fibrous Graphite Network and Self-Adhering Architecture", Energy Technology, 2(8), 677-684 (2014)
3. **S. Park**, I. Nam, G. –P. Kim, J. W. Han, and J. Yi, "Hybrid MnO_2 Film with Agarose Gel for Enhancing the Structural Integrity of Thin Film Supercapacitor Electrodes", ACS Applied Materials & Interfaces, 5(20), 9908-9912 (2013)
4. G. –P. Kim*, **S. Park***, I. Nam, J. Park, and J. Yi, "Preferential growth of Co_3O_4 anode material with improved cyclic stability for lithium-ion batteries", Journal of Materials Chemistry A, 1(12), 3872-3876 (2013).
   (* Soomin Park and Gil-Pyo Kim contributed equally to this work.)
5. **S. Park**, E. H. Kim, M. Eo, H. D. Song, S. Lee, J. –K. Roh, B. –C. Lee, Y. Kim, and J. Yi, "Effect of Dispersion Stability on the Deposition of Citrate-Capped Silver Nanoparticles in Natural Soils", Journal of Nanoscience and Nanotechnology, 13(3), 2224-2229 (2013).
6. **S. Park**, I. Nam, G. –P. Kim, J. Park, N. D. Kim, Y. Kim, and J. Yi, "A brain-coral-inspired metal-carbon hybrid synthesized using agarose gel for ultra-fast charge and discharge supercapacitor electrodes", Chemical Communications, 49(15), 1554-1556 (2013)

International Peer-Reviewed Journals (Co-author)

1. S. Bae, Y. G. Yoo, I. Nam, **S. Park**, J. Park, J. M. Lee, J. W. Han, and J. Yi, "Tunable Lithium Storage Properties of Metal Lithium Titanates by Stoichiometric Modulation", Electrochemistry Communications, *accepted*
2. S. Bae, I. Nam, **S. Park**, Y. G. Yoo, J. Park, J. M. Lee, J. W. Han, and J. Yi, "Sponge-like $Li_4Ti_5O_{12}$ constructed on graphene for high Li electroactivities", Journal of Nanoscience and Nanotechnology, *in press*
3. I. Nam,, J. Park, **S. Park**, S. Bae, Y. G. Yoo, and J. Yi, "Dual Planar Helix Type Energy Storage Wires to Circumvent Universal Energy Lag Effect", Advanced Energy Materials, 1501812 (2015)
4. S. Bae, I. Nam, **S. Park**, Y. G. Yoo, S. Yu, J. M. Lee, J. W. Han, and J. Yi, "Interfacial Adsorption and Redox Coupling of $Li_4Ti_5O_{12}$ with Nano-graphene for High-Rate Lithium Storage", ACS Applied Materials & Interfaces, 7(30), 16565-16572 (2015)
5. I. Nam, S. Bae, **S. Park**, Y. G. Yoo, J. M. Lee, J. W. Han, and J. Yi, "Omnidirectionally stretchable, high performance supercapacitors based on a graphene-carbon-nanotube layered structure", Nano Energy, 15, 33-42 (2015)
6. M. Lee, G. –P. Kim, H. D. Song, **S. Park**, and J. Yi, "Preparation of energy storage material derived from used cigarette filter for supercapacitor electrode", Nanotechnology, 25, 345601 (2014)
7. I. Nam, G. –P. Kim, **S. Park**, J. W. Han, and J. Yi, "All-solid-state, origami-type foldable supercapacitor chips with integrated series circuit analogues", Energy & Environmental Science, 7, 1095-1102 (2014)
8. S. Hong, **S. Park**, J. Park, and J. Yi, "Effect of end group modification of DNA-functionalized gold nanoparticles on cellular uptake in HepG2 cells", Colloids and Surfaces B: Biointerfaces, 112, 415-420 (2013)
9. G. –P. Kim, I. Nam, **S. Park**, J. Park, and J. Yi, "Preparation *via* an electrochemical method of graphene films coated on both sides with NiO nanoparticles for use as high-performance lithium ion anodes", Nanotechnology, 24(47), 475402 (2013)
10. G. –P. Kim, **S. Park**, I. Nam, J. Park, and J. Yi, "Synthesis of porous NiO materials

with preferentially oriented crystalline structures with enhanced stability as lithium ion battery anodes", Journal of Power Sources, 237(1), 172-177 (2013)

11. J. Park, W. G. Moon, G. –P. Kim, I. Nam, **S. Park**, Y. Kim, and J. Yi, "Three-Dimensional aligned mesoporous carbon nanotubes filled with Co_3O_4 nanoparticles for Li-ion battery anode applications", Electrochimica Acta, 105, 110-114 (2013)
12. J. Park, G. –P. Kim, H. N. Umh, I. Nam, **S. Park**, Y. Kim, and J. Yi, "Co_3O_4 nanoparticles embedded in ordered mesoporous carbon with enhanced performance as an anode material for Li-ion batteries", Journal of Nanoparticle Research, 15(9), 1943 (2013)
13. H. –J. Park, H. Y. Kim, S. Cha, C. H. Ahn, J. Roh, **S. Park**, S. Kim, K. Choi, J. Yi, Y. Kim, and J. Yoon, "Removal characteristics of engineered nanoparticles by activated sludge", Chemosphere, 92(5), 524-528 (2013)
14. I. Nam, **S. Park**, G. –P. Kim, J. Park, and J. Yi, "Transparent and ultra-bendable all-solid-state supercapacitors without percolation problems", Chemical Science, 4(4), 1663-1667 (2013)
15. H. –J. Park, **S. Park**, J. Roh, S. Kim, K. Choi, J. Yi, Y. Kim, and J. Yoon, "Biofilm-inactivating activity of silver nanoparticles: A comparison with silver ions", Journal of Industrial and Engineering Chemistry, 19(2), 614-619 (2013)
16. J. Roh, H. N. Umh, J. Sim, **S. Park**, J. Yi, and Y. Kim, "Dispersion stablity of citrate- and PVP-AgNPs in biological media for cytotoxicity test", Korean Journal of Chemical Engineering, 30(3), 671-674 (2013)
17. J. Park, G. –P. Kim, I. Nam, **S. Park**, and J. Yi, "One-pot synthesis of silicon nanoparticles trapped in ordered mesoporous carbon for use as an anode material in lithium-ion batteries", Nanotechnology, 24(2), 025602 (2013)
18. I. Nam, G. –P. Kim, **S. Park**, J. Park, N. D. Kim, and J. Yi, "Fabrication and design equation of film-type large-scale interdigitated supercapcitor chips", Nanoscale, 4(23), 7350-7353 (2012)
19. G. –P. Kim, I. Nam, N. D. Kim, J. Park, **S. Park**, and J. Yi, "A synthesis of graphene/Co_3O_4 thin films for lithium ion battery anodes by coelectrodeposition", Electrochemistry Communications, 22, 93-96 (2012)

20. S. Hong, **S. Park**, S. Lee, Y. I. Yang, H. D. Song, and J. Yi, "The Sensitive, Anion-Selective Detection of Arsenate with Poly(allylamine hydrochloride) By Single Particle Plasmon-Based Spectroscopy", Analytica Chimica Acta, 694(1), 136-141 (2011)

Domestic Publications (Korean journal)

1. 엄하늬, 노진규, 이병천, **박수민**, 이종협, 김영훈, "나노물질의 환경 매질별 노출 사례 조사", Korean Chemical Engineering Research, 50(6), 1056-1063 (2012)

Patents Application on File

1. 이종협, 백자연, **박수민**, 송찬경, 김태용, 남인호, "삼차원 구조의 구형 타이타니아 제조방법", 특허 출원 10-2015-0133388 (2015.09.21)
2. 이종협, 김길표, 이민재, 송현돈, **박수민**, "비금속이 도핑된 수퍼 커패시터 전극용 다공성 탄소물질", 특허 출원 10-2015-0002563 (2015.01.08)
3. 이종협, 남인호, 배성준, **박수민**, 유영근, "신축성 전자소자 및 에너지 저장을 위한 무기 액틴-미오신 결합", 특허 출원 10-2014-0175194 (2014.12.08)

International Conferences (First author)

1. **S. Park**, J. Baek, C. K. Song, T. Y. Kim, I. Nam, J. W. Han, and J. Yi, "Rational design of 3D TiO_2 for use in Li-ion battery", 227th ECS Meeting, Hilton Chicago, Chicago, Illinois, USA, May 24-28 (2015)
2. **S. Park**, I. Nam, G. –P. Kim, M. Lee, W. G. Moon, S. Bae, and J. Yi, "Robust hybrid film containing pseudocapacitive MnO_2 for large areal capacitance", 247th American Chemical Society National Meeting & Exposition, Dallas, Texas, USA, March 16-20 (2014)
3. **S. Park**, E. H. Kim, M. Eo, H. D. Song, H. Park, J. Roh, J. Yoon, Y. Kim, and J. Yi, "Transport behavior of silver nanoparticles in soil", 243rd ACS National Meeting &

Exposition, San Diego, California, USA, March 25-29 (2012)

4. **S. Park**, H. –J. Park, J. Roh, J. Yoon, and J. Yi, "Environmental Fate Evaluation of Silver Nanoparticles Released to the Soil", 6th International Conference on Materials for Advanced Technologies, Singapore, June 26-July 1 (2011)

International Conferences (Co-author)

1. I. Nam, G.-P. Kim, **S. Park**, S. Bae, Y. G. Yoo, J. W. Han, and J. Yi, "Origami-type supercapacitor chips with high voltage performance", 227th ECS Meeting, Hilton Chicago, Chicago, Illinois, USA, May 24-28 (2015)
2. S. Bae, H. D. Song, I. Nam, G.-P. Kim, **S. Park**, Y. G. Yoo, and J. Yi, "Computational analysis of battery performance working at low temperature", 227th ECS Meeting, Hilton Chicago, Chicago, Illinois, USA, May 24-28 (2015)
3. Y. G. Yoo, **S. Park**, I. Nam, S. Bae, and J. Yi, "Wearable and washable supercapacitor based on adhering architecture", 227th ECS Meeting, Hilton Chicago, Chicago, Illinois, USA, May 24-28, (2015)
4. S. Bae, I. Nam, **S. Park**, Y. G. Yoo, and J. Yi, "Graphene wrapped $Li_4Ti_5O_{12}$ derived by the hydrophilic-hydrophobic interaction", The Korean Society of Clean Techonology 2014 Fall Meeting, K hotel, Gyeongju, Korea, September 24-26 (2015)
5. I. Nam, **S. Park**, G.-P. Kim, S. Bae, Y. G. Yoo, and J. Yi, "Transparent supercapacitor solving performance reduction without percolation effect", The Korean Society of Clean Techonology 2014 Fall Meeting, K hotel, Gyeongju, Korea, September 24-26 (2014)
6. I. Nam, G.-P. Kim, **S. Park**, J. W. Han, S. Bae, S. Yu, H. N. Umh, S. Y. Lee, Y. H. Kim, and J. Yi, "High voltage energy storage systems using facile patterning approach", 248th American Chemical Society National Meeting & Exposition, San Francisco, CA, USA, August 10-14 (2014)
7. J. Baek, T. Y. Kim, I. Nam, **S. Park**, S. Yu, S. Bae, S. Y. Lee, H. N. Umh, Y. H. Kim, and J. Yi, "Production of valuable chemicals (1,3-butadiene) from biomass-based resources alternative to the petroleum", 248th American Chemical Society National

Meeting & Exposition, San Francisco, CA, USA, August 10-14 (2014)

8. I. Nam, **S. Park**, G.-P. Kim, H. D. Song, W. G. Moon, S. Bae, and J. Yi, "Fabrication of Transparent and Flexible Supercapacitor", 2013 MRS Fall Meeting Program & Exhibit, Boston, Massachusetts, USA, December 1-6 (2013)
9. S. Hong, **S. Park**, J. Park, H. D. Song, and J. Yi, "Real-time, Optical Monitoring of Cellular Internalization of Functional Gold Nanoparticles", The Korean Society for Environmental Analysis 2013 Fall Meeting, Lotte Hotel, Jeju, Korea, November 3-6 (2013)
10. G.-P. Kim, S. Bae, W. G. Moon, J. Park, I. Nam, **S. Park**, and J. Yi, "Synthesis of chemically modified carbon support for platinum electrocatalysts", The 14th Japan-Korea Symposium on Catalysis, WINC Aichi, Nagoya, Japan, July 1-3 (2013)
11. I. Nam, **S. Park**, G.-P. Kim, J. Park, N. D. Kim, I. K. Song, and J. Yi, "Design and preparation of innovative supercapacitors for energy storage systems", 245th ACS National Meeting & Exposition, New Orleans, Louisiana, USA, April 7-11 (2013)
12. G.-P. Kim, **S. Park**, I. Nam, J. Park, N. Kim, H. Song, and J. Yi, "Facile synthesis of Co_3O_4 nanoflakes embedded in 3D porous carbon matrix for lithium ion battery anodes by electrodeposition", 244th American Chemical Society National Meeting & Exposition, Philadelphia, Pennsylvania, USA, August 19-23 (2012)
13. I. Nam, N. D. Kim, J. Park, G.-P. Kim, **S. Park**, and J. Yi, "Environmentally Benign Synthesis of a Mn_3O_4/Graphene Hybrid Material for Use as an Anode in Li Ion Batteries", 16th International Meeting on Lithium Batteries, ICC Jeju, Korea, June 17-22 (2012)
14. Y. I. Yang, M. Eo, I. Choi, S. Lee, H. D. Song, **S. Park**, E. H. Kim, and J. Yi, "Preparation and characterization of Raman scattering-active hyperbranched plasmonic nanoparticles", 243rd ACS National Meeting & Exposition, San Diego, California, USA, March 25-29 (2012)
15. H. D. Song, I. Choi, S. Lee, Y. I. Yang, **S. Park**, E. H. Kim, M. Eo, T. Kang, and J. Yi, "Core-satellites assembly of plasmonic nanoparticles for the on-chip colorimetric sensors", 243rd ACS National Meeting & Exposition, San Diego, California, USA, March 25-29 (2012)

16. H. D. Song, I. Choi, S. Lee, Y. I. Yang, **S. Park**, T. Kang, and J. Yi, "Application of Plasmonic Coupling using Single Particle Core-satellites (COSA) Assembly", 6th International Conference on Materials for Advanced Technologies, Singapore, June 26-July 1 (2011)
17. Y. I. Yang, E. Jeong, I. Choi, S. Lee, H. D. Song, K. Kim, **S. Park**, Y. Choi, T Kang, and J. Yi, "In Situ Growth Monitoring of Heterogeneous Nanoparticles", 6th International Conference on Materials for Advanced Technologies, Singapore, June 26-July 1 (2011)
18. S. Hong, **S. Park**, J. Park, and J. Yi, "Quantifying and characterization of cellular internalization and localization of functionalized gold nanoparticles by oligomers", 240th ACS National Meeting and Exposition, Boston, MA, USA, August 22-26 (2010)

Domestic Conferences

1. 유성주, 김용화, 이수영, **박수민**, 유영근, 박종석, 이종협, "플라즈몬 유도 열전자를 이용한 효율적 태양광 에너지 전환", 한국화학공학회 2014년도 가을 총회 및 학술대회, 대전컨벤션센터, 10. 23-24 (2014)
2. 남인호, 김길표, **박수민**, 배성준, 유영근, 최경희, 이종협, "환경 분석용 휴대전자기기를 위한 투명한 에너지 저장 시스템 개발", 2014년 춘계 환경분석학회 학술대회, 전남 여수시 디오션호텔, 5. 22-23 (2014)
3. **박수민**, 유영근, 남인호, 배성준, 이종협, "수계 환경 분석용 전자기기를 위한 방수성 에너지 저장 시스템 개발", 2014년 춘계 환경분석학회 학술대회, 전남 여수시 디오션호텔, 5. 22-23 (2014)
4. 남인호, 김길표, **박수민**, 한정우, 이종협, "유사 직렬 구조를 기반으로 한 고전압 슈퍼커패시터 칩 개발", 한국전기화학회 2014년 춘계 총회 및 학술발표회, 창원컨벤션센터, 4. 10-12 (2014)
5. **박수민**, 유영근, 남인호, 배성준, 이종협, "접착성 기판을 이용한 전도성 탄소 네트워크의 제조 및 이를 이용한 접을 수 있는 슈퍼커패시터 개발", 한국전기화학회 2014년 춘계 총회 및 학술발표회, 창원컨벤션센터, 4. 10-12 (2014)

6. 이민재, 김길표, 송현돈, **박수민**, 문원균, 이종협, “사용된 담배필터를 재활용한 기공성 탄소제조 및 수퍼커패시터 성능평가”, 2014년 한국청정기술학회 춘계 학술발표회, 여수경도리조트, 3. 27-28 (2014)
7. **박수민**, 유영근, 남인호, 배성준, 이종협, “전도성 탄소 네트워크 제조 및 수퍼커패시터 전극으로서 응용”, 2014년 한국청정기술학회 춘계 학술발표회, 여수경도리조트, 3. 27-28 (2014)
8. 남인호, 김길표, **박수민**, 한정우, 이종협, “패턴화를 통한 고전압 수퍼커패시터 시스템”, 2014년 한국청정기술학회 춘계 학술발표회, 여수경도리조트, 3. 27-28 (2014)
9. 남인호, 김길표, **박수민**, 송현돈, 이민재, 문원균, 배성준, 이종협, “대면적의 패턴화된 망간 산화물 수퍼커패시터 개발 및 성능 평가”, 한국전기화학회 2013년 추계 총회 및 학술발표회, 대전컨벤션센터, 11. 7-9 (2013)
10. **박수민**, 남인호, 김길표, 문원균, 배성준, 이민재, 송현돈, 이종협, “박막전지의 구조적 안정성을 높이기 위한 유기겔-금속산화물 복합체 합성”, 한국전기화학회 2013년 추계 총회 및 학술발표회, 대전컨벤션센터, 11. 7-9 (2013)
11. 김길표, **박수민**, 남인호, 송현돈, 이민재, 배성준, 문원균, 이종협, “전기화학 증착법을 이용한 이방성 결정구조를 지닌 연결된 기공구조의 NiO 합성 및 리튬이온 배터리 음극 활용”, 한국전기화학회 2013년 추계 총회 및 학술발표회, 대전컨벤션센터, 11. 7-9 (2013)
12. 문원균, 박준수, 김길표, 남인호, **박수민**, 이종협, “삼차원으로 정렬된 탄소나노튜브/산화코발트 합성 및 리튬이온전지 음극물질로의 응용”, 한국화학공학회 2013년도 가을 총회 및 학술대회, 대구 EXCO, 10. 23-25 (2013)
13. 남인호, **박수민**, 김길표, 문원균, 배성준, 송현돈, 이종협, “아가로스 겔을 이용한 삼차원 금속/탄소 복합체 제조 및 고출력 슈퍼커패시터로의 응용”, 2013년 한국청정기술학회 추계 학술발표회, 제주 한화리조트, 9. 25-27 (2013)
14. **박수민**, 남인호, 김길표, 박준수, 배성준, 이종협, “고출력 슈퍼커패시터 전극을 위한 삼차원 구조의 금속/탄소 복합체 제조”, 한국전기화학회 2013년도 춘계총회 및 학술발표회, 창원컨벤션센터, 4. 11-13 (2013)
15. 남인호, 김길표, **박수민**, 박준수, 문원균, 이종협, “망간 산화물과 그래핀 복합체를 이용한 리튬 이온 전지의 음극 재료 개발”, 한국전기화학회 2013년

도 춘계총회 및 학술발표회, 창원컨벤션센터, 4. 11-13 (2013)

16. 김길표, **박수민**, 남인호, 박준수, 송현돈, 이종협, “Agarose Gel-Mediated Electrodeposition: Preferential Growth of Co_3O_4 anode material for Lithium-Ion Batteries”, 한국전기화학회 2013년도 춘계총회 및 학술발표회, 창원컨벤션센터, 4. 11-13 (2013)
17. 김길표, **박수민**, 남인호, 박준수, 이종협, “아가로스 겔 주형을 이용한 연결된 기공구조를 갖는 니켈옥사이드 합성 및 리튬 이차전지 음극 활물질 응용”, 2013년 한국청정기술학회 춘계 학술발표회, 여수 경도리조트, 3. 28-29 (2013)
18. **박수민**, 김길표, 남인호, 박준수, 배성준, 문원균, 이종협, “금속 산화물/유기겔 하이브리드 전극 제조와 박막형 슈퍼커패시터에의 응용”, 2013년 한국청정기술학회 춘계 학술발표회, 여수 경도리조트, 3. 28-29 (2013)
19. **박수민**, 김혜선, 어문정, 송현돈, 이수승, 노진규, 이병천, 김영훈, 이종협, “환경 거동 평가를 위한 은 나노입자의 토양 수착 분석”, 한국환경분석학회 2012 추계학술대회 및 심포지움, 제주도 라마다호텔, 11. 23 (2012)
20. 남인호, 김남동, 김길표, 박준수, **박수민**, 이종협, “고효율 커패시터를 위한 비정질 산화망간과 중형기공성탄소 복합체 제조”, 춘계 한국청정기술학회, 연세대학교, 5.25 (2012)
21. 김남동, 김소정, 박준수, 김길표, 남인호, **박수민**, 김필, 이종협, “슈퍼캐패시터의 전기화학적 성능 증가를 위한 질소도핑방법의 개발”, 한국화학공학회 봄 총회 및 학술대회, 제주국제컨벤션센터, 4.25-27 (2012)
22. 박준수, 김길표, 김남동, 남인호, **박수민**, 이종협, “실리콘 나노입자가 담지된 중형기공성 탄소체의 합성: 리튬 이차전지 음극 활물질 응용”, 한국화학공학회 봄 총회 및 학술대회, 제주국제컨벤션센터, 4.25-27 (2012)
23. 남인호, 김남동, 박준수, 김길표, **박수민**, 이종협, “비결정성 망간 산화물과 중형 기공성 탄소의 복합체 제조 및 수퍼커패시터 전극 활용”, 한국전기화학회 춘계총회 및 학술발표회, 광주광역시 김대중컨벤션센터, 4.12-14 (2012)
24. 김길표, 김남동, 박준수, 남인호, **박수민**, 이종협, “리튬 이차전지 음극 활물질 응용을 위한 그래핀/코발트 옥사이드 물질의 제조와 분석”, 한국전기화학회 춘계총회 및 학술발표회, 광주광역시 김대중컨벤션센터, 4.12-14 (2012)

25. 박준수, 엄하늬, 김길표, 김남동, 남인호, **박수민**, 김영훈, 이종협, “리튬 이차전지용 Co304/중형기공성 탄소 복합체의 전기화학적 특성”, 한국전기화학회 춘계총회 및 학술발표회, 광주광역시 김대중컨벤션센터, 4.12-14 (2012)
26. 양영인, 정은혜, 송현돈, 최인희, 이수승, **박수민**, 강태욱, 이종협, “나노플라즈모닉스를 이용한 고감도 환경 모니터링 방법”, 추계 환경분석학회, 제주KAL호텔, 11. 24-25 (2011)
27. 이수승, 김기훈, 양영인, 어문정, 송현돈, **박수민**, 강태욱, 이종협, “금속성 나노입자 기반의 분광 센서 탐침자 개발”, 추계 환경분석학회, 제주KAL호텔, 11. 24-25 (2011)
28. **박수민**, 홍수린, 이수승, 양영인, 송현돈, 이종협, “수용액 중 저농도 비소이온의 검출방법 - 양이온성 전해질 고분자로 개질된 단일 금 나노입자의 응용”, 춘계 환경분석학회, K water 연구원 상하수도 교육센터, 5. 26-27 (2011)
29. 박희진, 김희연, **박수민**, 노진규, 김영훈, 이종협, 윤제용, “Evaluation of bioaccumulation of silver nanoparticles”, 춘계공업화학회, 제주국제컨벤션센터, 5. 11-13 (2011)
30. 노진규, **박수민**, 박희진, 윤제용, 이종협, 김영훈, “나노물질의 PChem과 Nanotoxicity의 상관성에 관한 문헌연구”, 춘계화학공학회, 창원컨벤션센터, 4. 27-29 (2011)
31. 노진규, **박수민**, 박희진, 윤제용, 이종협, 김영훈, “Abiotic Degradability of Silver Nanoparticles under Light, Salt and Natural Organic Matters”, 춘계화학공학회, 창원컨벤션센터, 4. 27-29 (2011)
32. 김희연, 박희진, 노진규, **박수민**, 김영훈, 이종협, 윤제용, “활성오니를 이용한 은나노의 생분해성 평가”, 춘계 한국물환경학회, 국립환경인력개발원, 4. 22-23 (2011)
33. **박수민**, 박희진, 노진규, 이상희, 윤제용, 김영훈, 최경희, 이종협, “환경독성 연구를 위한 제조 은 나노입자의 응집과 침전에 관한 연구”, 추계화학공학회, 대전 컨벤션센터, 10. 20-22 (2010)